RASHBA SPIN-ORBIT INTERACTION IN MESOSCOPIC SYSTEMS

Frank Erik Meijer

Rashba spin-orbit interaction in mesoscopic systems

Proefschrift

ter verkrijging van de graad van doctor
aan de Technische Universiteit Delft,
op gezag van de Rector Magnificus prof. dr. ir. J.T. Fokkema,
voorzitter van het College voor Promoties,
in het openbaar te verdedigen op maandag 20 juni 2005 om 15.30 uur

door

Frank Erik MEIJER

natuurkundig ingenieur
geboren te Groningen.

Dit proefschrift is goedgekeurd door de promotor:

Prof. dr. ir. T. M. Klapwijk

Samenstelling van de promotiecommissie:

Rector Magnificus,	voorzitter
Prof. dr. ir. T.M. Klapwijk	Technische Universiteit Delft, promotor
Dr. A.F. Morpurgo	Technische Universiteit Delft, toegevoegd promotor
Prof. dr. G.E.W. Bauer	Technische Universiteit Delft
Prof. dr. P.W. Brouwer	Cornell University, Verenigde Staten
Prof. dr. L.W. Molenkamp	Universität Würzburg, Duitsland
Prof. dr. J. Nitta	Tohoku University, Japan
Prof. dr. ir. B.J. van Wees	Rijksuniversiteit Groningen

TUDelft   **NTT** ☺

"Je gaat het pas zien als je het door hebt"

Johan Cruijff

Preface

After having been a banker for some time, I realized that the time was not yet ripe for me to become rich; I first had to continue increasing my knowledge and understanding of the physical world around me in the form of a PhD. The present thesis describes the electron transport and spin dynamics in solid-state systems, and is the result of four years of research in Delft and in Japan. Although I am the alone author of this thesis, my research would never have been so successful without the help of other people.

First of all I would like to thank my advisor Prof. Teun Klapwijk for supporting and stimulating me during the past four years. You gave me the freedom to choose my own research projects, and allowed me to continue my research in Japan, even though Rashba spin-orbit interaction is certainly not the core business of your group. Your advice on many topics has been very helpful to me. Also, you have given me many opportunities to present my work at conferences around the world. I have appreciated this freedom and trust very much.

I am also very much indebted to my co-supervisor Dr. Alberto Morpurgo. You have not only contributed a great deal to my understanding of physics, but you have also taught me the importance of being critical in what I do (and yes, I know by now that I cannot fabricate a ballistic single-mode ring). Also, your input in writing high-quality scientific articles was indispensable, especially at the beginning. Thanks to the few occasions where your Italian temperament showed up, you have also enhanced my knowledge of Italian curses substantially.

The year that I have spent in the NTT Basic Research Laboratories in Japan in the group of Prof. J. Nitta has been the best period of my PhD. Nitta-san, I thank you very much for skillfully teaching me the basics of Rashba spin-orbit interaction, sample fabrication, and low-temperature measurements. You have contributed greatly to my joy in physics during all the years that we know each other. I also think back with great pleasure to all our dinner parties you organized, and the mountain trips we made together. I am sure that you will also be a great teacher and inspirer of your new students at Tohoku University.

My gratitude also goes to many other people from NTT; in the first place to

Dr. H. Takayanagi for making my stay at NTT possible. I would also like to thank Dr. Takaaki Koga for making his samples available to me, and organizing our holidays into the Japanese Alps. Moreover, my stay at NTT would never have been so pleasant (and hence productive) without Hashi and the secretaries; you have organized thousands of memorable dinner- and hanami parties, karaoke events and movie nights. Also other people have made my Japanese (nightlife) experience very enjoyable, in particular Robert Nijssen, Wilfred van Rooijen, Andreas Richter, Frank Deppe, Mike Stopa, Wilfred van der Wiel, Isao Tomita, Hiroyuki Tamura, Robert Anderson, and Marleen Vermeulen. Thank you all!

Although I was the only person working on Rashba spin-orbit interaction or anything alike in Delft, I have nevertheless always felt a strong emotional bond with my fellow PhD students Ruth, Hon Tin, Diederik, Paul, Ruurd, Saverio, Gert-Jan, Rogier, Chris, Merlijn, Monica, David, and Rami, as well as the post-docs and students. We could always share our feelings in good and bad times, and talk about important things in life. I especially thank Ruth for convincing me that plastic is indeed fantastic, and for providing me with excellent ideas for holidays, and Tino for sharing his Starbucks passion with me. You all created a very pleasant and productive working environment, seven days a week! Also people from QT have kept my C_2H_5OH-level high, especially Ronald (the next Tiësto), Laurens (Okonomiyaki master), and Alexander (next prime minister).

I also gratefully acknowledge Jan, Ben, and Jordi for their technical assistance, Jaap, Sven, Gao and Ad for their scientific assistance, and Monique and Maria for their general assistance. Moreover, I have benefitted greatly from discussions with Y. Nazarov, Y. Blanter, M. Baauboer from the theory section, and C-.M. Hu, T. Schäpers, J. Schliemann, M. Governale, U. Zülicke, from elsewhere.

Also people outside physics have contributed to the success of this thesis, by entertaining and supporting me, and boozing me up. In particular I would like to thank my Vindicat club; Reinout, Sjoerd, PJ, Rienk, Maarten, Geurt, Geert, Joost, and Floris. But equally important is the enduring friendship with my Groningen-connection; Mark, Sake, Diane, SJ, Frodo, Rutger, Victor, Hans, Corien, Sicco, Stephanie, Paulien, and more recently Arjen. I would also like to thank my friends from the monday-evening "Politiek Cafe" and the Masterclass for all our interesting discussions. Let's make the Netherlands a better place!

Finally, I am extremely grateful to my parents and my brother for their continuing and unconditional support during the past four years. Without this warmth at the home front it would have been impossible to successfully finish my PhD.

Frank Meijer, April 2005

Contents

Chapter 1

Introduction

1.1 Introduction

Semiconductors form the foundation of today's information age. They enable and underlie virtually every system that is involved in the manipulation and transport of information, from laptop computers to cellular phones and satellite-based global communication networks. Semiconductor materials are nowadays as vital to the worlds economic growth, or maybe even more vital, as were once other materials such as stone, wood, coal and metals.

Ironically, semiconductors - which are neither highly conducting nor highly insulating - were initially not believed to be particularly useful. The true potential of semiconductors was recognized after the discovery that their conductivity is extremely sensitive to the addition of dopant atoms and the application of electric fields. This characteristic resulted in the fabrication of the first gate voltage controlled switches and amplifiers: it was the birth of the transistor age [1]. The development of sophisticated growth techniques to manufacture high-quality structures (higher electron mobility) and micro-patterning techniques (ongoing miniaturization of transistors) over the last decades, allowed to achieve tremendous improvements in the processing and calculation speed of transistors. These developments extended their commercial applicability substantially.

1.1.1 III-V semiconductors

Silicon (Si) plays currently a dominant role in the world of microelectronics. This is mainly due to the natural abundance of Si (beaches), and the fact that Si forms a high-quality natural oxide, which is being used as a gate oxide in the transistor technology. In the last decades, however, the large potential of another class of semiconductors is being recognized. These are the so-called III-V compound semiconductors, which consist of a mixture of elements of group III (e.g., Al, Ga, In) and group V (e.g., As, P, Sb) of the periodic table, such as GaAs and InGaAs. The applicability of this class of semiconductors is fuelled again by the impressive improvements in epitaxial growth techniques, such as MBE and MOCVD, resulting in an electron mobility that surpasses that of Si by far. This has made III-V semiconductors ideal candidates for ultra-fast electronics. To date there exist, for example, already InGaAs-based transistors operating at 560 GHz, although they are (still) more expensive than their Si-based counterpart.

In addition to their superior performance in high-speed, low-power electronic applications, III-V semiconductors were also found to have excellent optoelectronic properties. III-V semiconductors are in many cases direct bandgap materials, and are therefore particularly important for electroluminescense devices,

such as light emitting diodes and lasers (high quantum efficiency). Moreover, the bandgap of III-V quantum wells - and therefore the wavelength at which they emit or detect radiation - can be engineered/tuned by the appropriate mix of III-V compounds. This possibility has been exploited, e.g., to fabricate eye-safe infrared-lasers for cash registers, has generated new methods for astrophysical remote sensing, and is also being utilized in optical telecommunication applications: tailor-made (InGaAs-based) lasers have been designed that emit at a wavelength at which the losses in optical fibers is minimal, enabling/improving high-speed broadband communication systems. Finally, epitaxial III-V semiconductors have even demonstrated the highest efficiency of any type of solar cells ($> 35\%$) [2].

Therefore, it is correct to state that the improved control over III-V semiconductor crystal growth has powered a revolution in photonics and opto-electronics, just as Si has done in microelectronics a decade earlier. Moreover, when III-V compounds can be grown on cheap substrates in future [3], it might even become commercial to let them replace Si in every-day microelectronics.

1.1.2 Fundamental research

The commercially driven activities described above have also had an offspring to research in fundamental physics. The epitaxial growth of III-V semiconductor layers and quantum wells, together with the improvements in microfabrication techniques, have facilitated unprecedented possibilities for fundamental research. In high-purity semiconductors and quantum wells electrons move ballistically, and are phase-coherent over large distances at low enough temperatures (typically $> 1\,\mu\text{m}$ at $\text{T} \sim 1\,\text{K}$). In this regime, the classical Boltzmann description of electron transport does no longer hold, and new theories were developed that take the phase-coherent, i.e., the quantum mechanical (or wavelike) nature of electrons into account. Experimentally, new interesting phenomena in high-quality structures were observed, which are generally not observable in metal systems, such as Shubnikov-de Haas oscillations, the integer and fractional quantum Hall effect [4], as well as quantized conduction [5]. It became also possible to fabricate and study (phase-coherent) transport through fascinating structures, such as quantum dots (artificial atoms) [6]. In fact, due to the tailor-made wafer design and microfabrication it became possible to fabricate almost any desired 2D, 1D or 0D model system, which allowed to test the new theories and to obtain new knowledge ("do it yourself quantum mechanics").

Note that the obtained fundamental knowledge about quantum mechanics and electron transport might, in return, also be beneficial for the applied community. For example, due to the miniaturization of transistors, the physics in these devices

will in the end also be determined by the quantum mechanical nature of electrons, causing unpredictable fluctuations in essential design parameters. Hence, a thorough understanding of the world of mesoscopic (phase-coherent) physics will be necessary for the future transistor technology.

1.2   Spintronics

The functionality of modern semiconductor-based commercial devices relies only on the control of the electronic charge: the spin degree of freedom of carriers does not play a role, and is not being utilized in any way. This heavily contrasts the situation in modern metal-based devices and applications, in which ferromagnetism - a macroscopic spin phenomenon - plays a central role.

The most important spin-dependent effect in metallic systems is the giant magneto-resistance (GMR) effect, discovered in 1988 [7]. The resistance of metallic multi-layer structures, consisting of alternating magnetic and non-magnetic layers, was found to depend on the relative orientation of the magnetization directions of the ferromagnetic layers. Specifically, the resistance is lowest (highest) when the magnetic moments are aligned (anti-aligned) [8]. This property makes that applying a small external magnetic field induces a significant change in resistance of the multilayer, up to 20% at room temperature. Soon after its discovery, the GMR effect found its application in information storage and reading, for example in read heads for hard disks and MRAM memory [9].

Nowadays, the research (and user's field) that aims at identifying, understanding, controlling, and finally utilizing spin-dependent phenomena, is known as "Spintronics".

1.2.1   Semiconductor spintronics

Motivated by the tremendous commercial success of spintronics in metallic systems, the electron spin degree of freedom has also become the center of interest in semiconductor physics, both experimentally and theoretically. In contrast to metals, however, in semiconductor spintronics essentially all device proposals and potential applications are motivated by (or based on) the binary nature of a *single* spin [10].

When the spin-direction of an electron is measured along an arbitrary axis it can only be "up" or "down", and could therefore represent "1" and "0", respectively. Hence, the electron spin could be utilized to transport digital information, since it is attached to mobile conduction electrons. Moreover, the spin state can

in principle be controlled by magnetic and electrostatic means, making it possible to perform elementary operations on the digital spin-bit. Hence, utilizing the spin degree of freedom could open new possibilities to future spin-based data processing and calculation schemes [10].

In this context we note that the phase-coherence time of electron spins is generally much longer than that of charge states. This might offer the opportunity to store and manipulate phase-coherence on relevant time scales, and to use the spin as an elementary quantum bit for quantum computation. Currently, experiments to entangle electron spins in coupled quantum dots and perform qubit rotations are being performed, which might lead - in the far future - to the realization of the revolutionary ideas in the field of quantum computation [11].

The application of the spin degree of freedom is not limited to quantum transport. The spin might also play a role in quantum optics. The possibility to engineer the coupling between spins and optical photons has already resulted in proposals for a spin-based light emitting diode (spin-LED [12]) and spin-based optical switches operating at terahertz frequency. More proposals and applications are likely to follow.

So far, however, the field of semiconductor spintronics is far from any commercial application. A lot of major fundamental issues and practical problems need to be resolved before any widespread semiconductor spintronic device will reach the market. In fact, at this emerging stage of semiconductor spintronics, fundamental- and application-minded research are still going hand in hand.

1.2.2 Material systems

III-V semiconductors are also very suitable materials for future semiconductor *spintronic* applications. This is because the control over the III-V semiconductor growth also offers the opportunity to engineer essentially all the relevant parameters that determine the spin dynamics in these structures, including the g-factor (Zeeman coupling) and the spin-orbit interaction strength [13]. This is of vital importance for most spintronic applications, and is generally not possible in metallic systems. In addition, the control over parameters also offers, as previously in the case of electronics, great opportunities to study fundamental spin-dependent phenomena. Hence, spintronics can be seen as the extension of traditional mesoscopic physics: the interest has shifted from the electron charge and its coherence, to effects that are related to the spin and its coherence.

Narrow-gap III-V semiconductor quantum wells - based on InAs, InGaAs, or InSb, for example - are particularly important for spintronics. The main reason is that in these (appropriately designed) quantum wells the dominant type of spin-

orbit interaction is tunable by electrostatic means, allowing to affect/control the spin-dynamics in these quantum wells by applying gate voltages. This type of spin-orbit interaction is known as Rashba spin-orbit interaction [14], and is the central theme of this Thesis.

1.3   Spin-orbit interaction

As its name already implies, spin-orbit interaction (SOI) gives rise to a coupling between the spin dynamics of an electron and its (orbital) motion in space. Below we will give an intuitively picture of spin-orbit interaction. In Chapter 2 we will present a more formal description of SOI, in particular of Rashba SOI.

If an electron is travelling through an electric field, it "sees" in its restframe a moving electric field, i.e., moving charges. These moving charges - or electrical current - give rise to an "internal magnetic field" in the restframe of the electron. This "internal magnetic field" couples, in return, to the spin of the electron. The magnitude and the direction of this internal magnetic field depend on the velocity and travel direction of the electron in a material, i.e., SOI gives rise to a $\mathbf{k}$-dependent internal magnetic field, where $\mathbf{k}$ is the wavevector of the electron. SOI is in many respects similar to the more familiar Zeeman coupling. SOI lifts for example the spin degeneracy, and results in a ($\mathbf{k}$-dependent) spin-splitting of the conduction band [13]. Some of the important differences between SOI and Zeeman coupling will be discussed in Chapter 2.

In solid state systems, SOI is generally caused by three different "sources" of electric field: (1) impurities in the conduction layer, (2) lack of crystal inversion symmetry, and (3) lack of structural inversion symmetry of the confinement potential of electrons in a quantum well or heterostructure.

(1) The SOI due to the impurities is usually very weak in epitaxially grown III-V quantum wells, and can be neglected in practice. It is, however, the main source of SOI in metallic systems, since the other two mechanisms are absent.

(2) Most III-V semiconductors crystallize in the zinc-blende structure. In contrast to silicon (diamond structure), the lattice of the zinc-blende structure does not have inversion symmetry. Hence, electrons moving through this lattice "feel" an asymmetric crystal potential. This effectively results in SOI, and the corresponding spin-splitting of the conduction band, as was demonstrated theoretically by Dresselhaus. Hence, this type of SOI is known as Dresselhaus SOI [15]. The strength of Dresselhaus SOI depends only on the atomic elements in the crystal lattice. The Dresselhaus spin-split energy does, however, depend on the Fermi wavevector.

(3) When the motion of electrons is confined to two dimension, for example in quantum wells, an asymmetric confinement potential forms another source for SOI. The importance of this mechanism lies in the fact that the asymmetry in the confinement potential can be varied by electrostatic means, allowing to tune the SOI strength by an external gate voltage [16]. This type of SOI is known as Rashba SOI [14]. For reasons that will be explained in Chapter 2, the strength of Rashba SOI depends also on the crystal composition in the quantum well, and is largest for narrow gap III-V semiconductors, such as InAs and InGaAs.

The total SOI in a sample, and hence the total internal magnetic field that couples to the spin, is the sum of the above three contributions. The competition between these SOI mechanisms leads in general to complex behavior of the spin dynamics. In narrow-gap III-V quantum wells, however, the Rashba SOI is generally much larger than the other two mechanisms, which makes it often an excellent approximation to neglect the contribution due to impurities and the Dresselhaus mechanism [16]. In the rest of the Introduction and this Thesis we will therefore mainly focus on the effects related to Rashba SOI.

1.3.1   Spin dynamics in the presence of Rashba SOI

As mentioned above, Rashba SOI gives rise to an internal magnetic field $\mathbf{B}_{SOI}$, which has the form $\mathbf{B}_{SOI} = \alpha(Vg)|\boldsymbol{k}| \ (\hat{\boldsymbol{k}} \times \hat{z})$, i.e., the magnitude of $\mathbf{B}_{SOI}$ is proportional to the product of $|\mathbf{k}|$ and a voltage-dependent parameter, and it is pointing in the direction perpendicular to both $\mathbf{k}$ and $\hat{z}$ (with $\hat{z}$ the growth direction of the quantum well). In the absence of an externally applied magnetic field, the spin will precess around this internal magnetic field $\mathbf{B}_{SOI}$, analogous to Larmor-precession around an external magnetic field. The precession frequency depends on the magnitude of the internal magnetic field $|\mathbf{B}_{SOI}|$, and hence can be modified by applying a gate voltage [16]. This property has led to the proposal of a Datta-Das "toy-model" [17], also known as the Datta-Das spin-transistor (although its practical usefulness is far from obvious).

Datta and Das consider a ballistic transport channel with Rashba SOI, with at either side of the channel a ferromagnetic lead (see Fig. 1.1). When a spin is injected from one of the leads, it precesses around the internal Rashba field $\mathbf{B}_{SOI}$ until it arrives at the other ferromagnetic lead (the drain). The electron's transmission probability into the drain depends on the relative alignment of its spin with the drain's (fixed) magnetization. Since the total precession angle of the spin during the travel to the drain can be controlled by a gate voltage, so can the source-to-drain current (or conductance). Hence, this device is called a "spin-FET", since its operation relies on the field-effect.
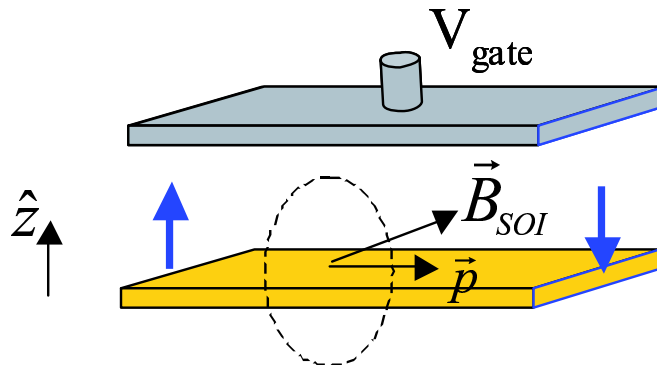
Figure 1.1: A schematic overview of the Datta-Das spin-FET. An injected spin on
the left is precessing around the Rashba field $\mathbf{B}_{SOI}$ when it is moving to the right with
momentum $\mathbf{p}$. The magnitude of $\mathbf{B}_{SOI}$ can be tuned by the gate voltage, and hence
so can the total spin precession angle.

The importance of this Datta-Das "spin-transistor" is probably not its appli-
cability, but the intense scientific discussion it stimulated about the spin dynamics
in 2D electron gases with Rashba SOI. It has motivated the experimental and
theoretical investigation of the role of elastic scattering and dimensionality, for
example [18]. Moreover, it has also resulted in studies of the combined effect
of Rashba SOI and Dresselhaus SOI on the spin dynamics [19], as well as the
combined effect of Rashba SOI and Zeeman coupling [20, 21]. All these investi-
gations, in return, have led to the discovery of new spin-related effects and new
applications and devices. The paradigm of the Datta-Das device has therefore
had quite a broad impact on the field of spintronics.

From the example of the Datta-Das device it is clear that the spin dynamics
in a ballistic channel is rather simple: the spin is just precessing around the
internal Rashba field. The situation becomes more complicated in the presence
of elastic scattering (which is present in essentially all real systems). As outlined
above, the internal Rashba field $\mathbf{B}_{SOI}$ is always pointing perpendicular to the
travel direction of the electron, i.e., perpendicular to $\mathbf{k}$. Since elastic scattering
randomizes the travel direction, also the Rashba field - around which the spin is
precessing - changes direction after each scattering. This randomization of the
spin precession axis results in the loss of memory of the initial spin direction; i.e.,
elastic scattering leads to spin relaxation. This is the so-called Dyakonov-Perel
spin-relaxation mechanism [22] (for further details see Ch. 2).

Currently, there is an intense discussion whether the "inverse" effect is pos-
sible: if the spin-dynamics of an electron is determined by the orbital motion

of the electron, could the orbital motion of the electron also depend on its (initial) spin-direction? Although the debate continues, experimental observations of this so-called spin-Hall effect in solid state systems have already been reported recently [23].

From an application point of view, the spin relaxation time and spin relaxation length are very important, since they determine the upper time- and length scales on which proposed spintronic devices can operate. Increasing the spin relaxation time in experimental systems is of central importance, and several ways to suppress the Dyakonov-Perel spin relaxation mechanism have been proposed. Examples include the confinement of the electron motion to narrow quantum wires [18], and applying additional Zeeman coupling [20, 21]. Below, these two spin-lifetime enhancing mechanisms are explained in some more detail.

A characteristic of the Dyakonov-Perel spin relaxation mechanism is that the spin relaxation time is inversely proportional to the elastic scattering time, i.e., heavy scattering slows down the spin relaxation process [22]. This is due to the inability of the electron spin to follow the internal Rashba field $\mathbf{B}_{SOI}$ when it is varying its direction too rapidly. This characteristic implies that introducing additional scattering, for example from the walls of the quantum wire, will enhance the spin relaxation time. Indeed, it has been demonstrated theoretically that decreasing the width of the quantum wire below the spin precession length, results in a large increase of the spin relaxation time [18].

The spin relaxation time can also be enhanced by adding Zeeman coupling (see Ch. 7). In the presence of both Rashba SOI and Zeeman coupling the spin will precess around the (vectorial) sum of the internal Rashba field and the external Zeeman field. Since the direction of the external magnetic field does not depend on the travel direction of the electron, its effect on the spin dynamics is to "stabilize" the spin precession axis. If the external magnetic field (Zeeman coupling) is large enough, the spins will stay aligned parallel or anti-parallel with the external magnetic field, despite of the elastic scattering. Hence, Zeeman coupling results in a (large) increase of the spin relaxation time [20, 21].

The spin dynamics in diffusive 2D electron gases with Rashba SOI and Zeeman coupling seems to be quite complex in general. Parameters like the electron density, elastic scattering time, Rashba spin-split energy, etc., could all play a role. In Chapters 7 and 8 of this Thesis we will demonstrate, however, that the spin dynamics - in particular the spin relaxation time - depends only on the ratio of two energy scales; the Zeeman energy and a Rashba SOI related energy scale (which is inversely proportional to the Dyakonov-Perel spin relaxation time) [20, 21]. In this sense the spin-dynamics in 2D electron gases with Rashba SOI is expected to be well-defined and "universal".

1.3.2   Effect of Rashba SOI on phase-coherent transport

In the previous section we discussed the spin-dynamics in 2DEGs with Rashba
SOI, when scattering and Zeeman coupling are present. The modification of the
spin-dynamics has also interesting consequences for phase-coherent phenomena,
and can lead to new spin-dependent, phase-coherent effects. Before discussing
those spin-effects, we first give a brief overview of some important concepts in
phase-coherent transport.

If the temperature is low enough ($\sim$ 1K), inelastic scattering processes, such
as electron-electron interaction and electron-phonon scattering, weaken. What
remains is elastic scattering on impurities and defects, which do not change the
energy of the electron, and do therefore not randomize its phase (i.e the elec-
tron wavefunction stays phase-coherent). In this regime, the classical Boltzmann
transport theory does no longer hold, and new *phase-coherent* effects can be ob-
served. All these phase-coherent effects are essentially based on the quantum
mechanical law that the total probability of a certain process is given by the
absolute square of the sum over all possible (complex) amplitudes (see Ch. 2).
In general, this leads to interference effects between the complex partial proba-
bilities, and therefore often to non-classical behavior. A beautiful and appealing
example of this quantum mechanical principle is the Aharonov-Bohm effect [24],
which leads to magnetoconductance oscillations in a ring geometry.

Aharonov-Bohm (AB) oscillations belong to the class of so-called sample-
specific effects, since they depend on the details of the system, such as the radius
of the ring and the precise scattering configuration. Another example belonging
to this class are universal conductance fluctuations (UCF), which are caused by
the random interference of electronic waves (rather than the well-defined inter-
ference in a 1D ring structure). UCF is observable in systems with dimensions
smaller than the phase-coherence length, for example quantum dots [28]. The
typical characteristic of sample-specific effects is that they disappear upon en-
semble averaging: If one would measure, for example, the magnetoconductance
of many rings in series, the Aharonov-Bohm ("h/e") oscillations would vanish.
The same holds true for UCF.

The other class of phase-coherent effects consist of phenomena that survive
ensemble averaging, and do not depend on the details of the system, such as
the scattering configuration. This class of effects is caused by the interference
of electronic waves travelling along *time-revered* paths. The phase-difference be-
tween these time-reversed partial waves is zero (assuming spinless particles, and
no magnetic field), since they "see" exactly the same electrostatic environment.
This results in positive interference, or coherent-backscattering, independent of

the details of the followed scattering path. A small magnetic field modifies the phase-difference between the time-reversed waves, however, and leads to $h/2e$ oscillations in ring structures, and to the well-known logarithmic weak-localization (WL) correction to the Drude conductivity in 2D systems, for example.

Rashba SOI has a significant effect on all the above mentioned sample-specific and ensemble-averaged phase-coherent phenomena. Below we briefly discuss some of the most important consequences; a more elaborate discussion of the effect of Rashba SOI on phase-coherent transport will be given in Chapter 2.

The influence of Rashba SOI on the localization correction to the Drude conductivity is known best, and has been studied extensively. It has been shown that strong Rashba SOI - which affects the spin dynamics severely - results in a sign change of the conductance correction, i.e., coherent back-scattering in the absence of Rashba becomes coherent forward-scattering [25]. This positive correction to the Drude conductivity is known as weak anti-localization (WAL). The tunability of the Rashba SOI in quantum wells has made it possibile to show beautifully the crossover between WL (no Rashba) and WAL (strong Rashba) by applying a gate voltage [26], as well as by changing the quantum well design [27]. In Chapters 7 and 8 we will show that "stabilizing" the spin-dynamics (fixing the spin-precession axis by additional Zeeman coupling), also results in a crossover from WAL to WL [21]. These experiments beautifully illustrate the role of the spin-dynamics on coherent backscattering.

Spin-orbit interaction also affects the sample-to-sample conductance fluctuations, referred to as universal conductance fluctuations (UCF) [28, 29]. The average amplitude of the UCF does not depend on sample size or degree of disorder, but the mean amplitude *does* depend on the presence of a magnetic field and/or SOI. Specifically, in the absence of magnetic fields and SOI their amplitude is of the order of e^2/h. If time-reversal symmetry is broken by a magnetic field, their amplitude is reduced by a factor 2. In case the spin-rotational symmetry is broken, e.g., by strong Rashba SOI, the amplitude of the UCF is reduced by a factor 4. Moreover, in the presence of both a magnetic field and SOI, the reduction is even a factor 8, as has been demonstrated within a random-matrix description of quantum transport [29].

Finally, Rashba SOI is predicted to affect the (h/e and $h/2e$) Aharonov-Bohm oscillations. In the presence of Rashba SOI and a magnetic field perpendicular to the ring, the spin makes a solid angle as the electron is travelling around the ring, which results in a spin-dependent phase-shift of the wavefunction (see Ch. 5). This Rashba-induced phase shift will have an observable effect in the Fourier spectrum of the AB oscillations. Specifically, it predicted to lead to a splitting of the characteristic h/e peak [30]. Moreover, the Rashba-induced phase shift is also

predicted to give rise to fluctuations in the amplitude of the (ensemble-averaged) $h/2e$ peak in the Fourier spectrum [31]. The experimental observation of these subtle effects is not trivial, however, as we will show in Chapter 6.

As the above examples illustrate, studying the effect of Rashba SOI on phase-coherent phenomena is an interesting topic in itself, and allows to obtain a deeper fundamental understanding of the role of the spin degree of freedom in mesoscopic physics. For this purpose, the tunability of the Rashba strength and the flexibility to affect/control the spin dynamics by the interplay with Zeeman coupling is especially interesting, since it offers the possibility to study all kinds of crossovers and to test newly developed theories.

In return, nowadays well-understood phase-coherent phenomena, such as WAL, can also be utilized for the investigation of certain aspects of the spin dynamics that are not yet fully understood, such as the effect of the competition between Rashba SOI and Zeeman coupling (see Ch. 7 and 8 [21]). Note that this "analyzing technique" of the spin dynamics is very practical, because it involves only simple transport measurement, in contrast to more elaborate optical techniques [32]. Moreover, WAL measurements are also routinely used to extract the Rashba SOI strength [16] and the electron g-factor (see Ch. 7 and [33]); it has become a standard characterization tool for quantum wells and heterostructures.

On the applied side it is interesting to note that there exist proposals to utilize phase-coherent, spin-dependent, phenomena for spintronic devices (see Ch. 5). For example, the possibility to control the phase shifts in a ring structure by electrostatic means, has led to the proposal for a (spin-based) conductance modulator, or spin interference device [34]. Moreover, it was demonstrated that quantum interference in the presence of Rashba SOI can be utilized to produce a spin filter [27], i.e. to create spin-polarized currents, which might be of paramount importance for many potential future applications.

1.4   This Thesis

As outlined in the previous sections, Rashba SOI might play a crucial role in spintronics, as far as controlling the spin dynamics is concerned. Especially the tunability of the Rashba spin-orbit strength by electrostatic means, and by quantum well design, offer new possibilities that did not exist in the old metal-based counterpart. In addition, on a more fundamental level Rashba SOI is predicted to give rise to interesting new phenomena, which cannot be (clearly) observed in metallic systems investigated in the past. Studying systems with Rashba SOI, and understanding the physics that those experiments reveal, is therefore

of importance for the applied spintronic community, as well as for fundamental reasons.

In this Thesis we address - partly theoretically and partly experimentally - the following central questions: (1) What is the effect of Rashba SOI on phase-coherent transport in mesoscopic systems, such as Hall bars and ring structures? (2) How does the competition between Rashba SOI and Zeeman coupling affect the spin dynamics in 2D electron gases? (3) What can be said about the breaking of time-reversal symmetry in the 2D electron gas, in the presence of Rashba SOI and Zeeman coupling?

In order to answer these questions we have developed and investigated quantum wells with different, and tuneable, Rashba SOI strength. Also, we have developed a quite unique experimental setup, where we can apply a magnetic field perpendicular and parallel to the quantum well independently, in order to create Zeeman coupling and study quantum interference at the same time.

1.4.1 Outline of this Thesis

This Thesis is written in such a way that all the Chapters can be read and understood without having the knowledge of the foregoing Chapters. The amount of redundancy is kept, however, to a minimum for those reading this Thesis from the beginning to the end.

Chapter 2: In this Chapter we describe all the important theoretical concepts that are at the basis of this Thesis. The main focus in the Chapter is on quantum interference in the presence of Rashba SOI, and on the formal derivation of the Rashba SOI strength in arbitrary quantum wells.

Chapter 3: We have studied different kinds of samples, fabricated out of different kinds of heterostructures. In this Chapter the different heterostructures and samples are characterized. We also briefly address the sample fabrication procedure, as well as the our measurement system.

Chapter 4: In order to study theoretically the effect of Rashba SOI, model-Hamiltonians are being used. Finding the physically correct Hamiltonian seems trivial, but has resulted in ambiguities and errors in literature. For example, a non-hermitean Hamiltonian has been used in literature to model a 1D ring structure. In this Chapter we show in detail the procedure to derive the correct Hamiltonian for electrons moving on a 1D ring in the presence of Rashba SOI and a perpendicular magnetic field.

Chapter 5: In this Chapter we theoretically study a 1D ring in the presence of Rashba SOI and a perpendicular field. In particular, we calculate its eigenfunctions and eigenenergies, from which we find the (spin-dependent) phase-shifts in

the wavefunction, when the electron is travelling around the ring. The phase shift is found to depend on the Rashba SOI strength, which in return is tunable by a gate voltage. We propose to utilize a ring structure with Rashba SOI as a spin-based "conductance modulator", or spin-interference device.

Chapter 6: From the theoretical 1D model it follows the wavefunction picks up a spin-dependent geometrical phase - the Aharonov-Casher phase - when it is travelling around the ring. This is predicted to result in a splitting of the h/e peak in the Fourier transform of the magnetoconductance of the (1D) ring. In this Chapter we show experimentally that sample-specific effects dominate the Fourier spectrum in real (quasi-2D) ring structures, which impedes the possibility to observe the Aharonov-Casher phase directly. We demonstrate that the sample-specific features can be suppressed by ensemble averaging the Fourier spectra. This allows us to observe a statistical significant splitting in the h/e peak in the ensemble-averaged Fourier spectrum.

Chapter 7: In this Chapter we systematically investigate the how the competition between Rashba SOI and Zeeman coupling affects the spin-dynamics, in particular the spin-relaxation time. We demonstrate that this information can be extracted from the magnetoconductance of a Hall-bar, as a function of a perpendicular and parallel magnetic field. We find that the spin relaxation time depends about quadratically on the ratio Zeeman energy/Rashba energy, in agreement with recent theory. In this Chapter we also show that the competition between Rashba SOI and Zeeman coupling result in breaking of time reversal symmetry, and therefore introduces an upper cut-off time for the interference of time-reversed waves which is shorter than the usual inelastic scattering time. In addition, this analysis is shown to provide a new way to determine the g-factor of electrons in the Hall-bar.

Chapter 8: The results in Chapter 7 are obtained in the limit that the Zeeman energy is (much) smaller than the Rashba SOI energy, i.e. Zeeman coupling can be considered as a small perturbation. In this Chapter we study the time-reversal symmetry (TRS) breaking due to the competition between Rashba SOI and Zeeman coupling for arbitrary values of their ratio. We find that the TRS breaking saturates when the Zeeman energy (E_Z) becomes comparable to the Rashba energy (E_{SOI}). Moreover, we find that this spin-induced TRS breaking mechanism is a universal function of the ratio E_Z/E_{SOI}, within the experimental accuracy.

References

[1] Transistor action was first discovered in Germanium at the Bell Labs in 1947.

[2] see, e.g., the homepages of Spectrolab (www.spectrolab.com) and the National Renewable Energy Laboratory (www.nrel.gov)

[3] E.P.A.M. Bakkers, J.A. van Dam, S. de Franceschi, L.P. Kouwenhoven, M. Kaiser, M. Verheijen, H. Wondergem, and P. van der Sluis, Nature Materials **3**, 769 (2004)

[4] The discovery of the integer and fractional Quantum Hall effect were both awarded the nobel price (in 1985 and 1998, respectively).

[5] These effects are described in almost any modern textbook, e.g., D.K. Ferry and S.M. Goodnick, *Transport in Nanostructures* (Cambridge University Press, UK, 1997)

[6] See, e.g., L. P. Kouwenhoven, T.H Oosterkamp, M.W.S. Danoesastro, M. Eto, D.G. Austing, T. Honda, and S. Tarucha, Science **278**, 1788 (1997).

[7] M.N. Baibich, J. M. Broto, A. Fert, F. Nguyen Van Dau, F. Petroff, P. Eitenne, G. Creuzet, A. Friederich, and J. Chazelas, Phys. Rev. Lett. **61**, 2472 (1988).

[8] Similar properties were found in so-called magnetic tunnel junctions, which consist of two ferromagnetic layer separated by a thin tunnel barrier.

[9] M. Dax, Semicond. Int. **20**, 84 (1997)

[10] S.A. Wolf, D.D. Awschalom, R.A. Buhrman, J.M. Daughton, S. von Molnar, M.L. Roukes, A.Y. Chtchelkanova, and D.M. Treger, Science **294**, 1488 (2001); D.D. Awschalom, D. Loss, and N. Samarth, *Semiconductor Spintronics and Quantum Computation* (Spinger-Verlag, Berlin, 2002); I. Zutic, J. Fabian, and S. Das Sarma, Rev. Mod. Phys. **76**, 323-410 (2004)

[11] W.G. van der Wiel, S. De Franceschi, J.M. Elzerman, T. Fujisawa, S. Tarucha, and L.P. Kouwenhoven, Rev. Mod. Phys. **75**, 1 (2003)

[12] Y. Ohno, D.K. Young, B. Beschoten, F. Matsukura, H. Ohno, and D.D. Awschalom, Nature **402**, 790 (1999)

[13] R. Winkler, *Spin-Orbit Coupling Effects in Two-Dimenional Electron and Hole Systems* (Springer-Verlag, Berlin, 2003)

[14] E.I. Rashba, Sov. Phys. Solid State **2**, 1109 (1960); Y.A. Bychkov and E.I. Rashba, J. Phys. C **17**, 6039 (1984)

[15] G. Dresselhaus, Phys. Rev. **100**, 580 (1955)

[16] J. Nitta, T. Akazaki, H. Takayanagi, and T. Enoki, Phys. Rev. Lett. **78**, 1335 (1997); T. Koga, J. Nitta, T. Akazaki, and H. Takayanagi, Phys. Rev. Lett. **89**, 46801 (2002)

[17] S. Datta and B. Das, Appl. Phys. Lett. **56**, 665 (1990)

[18] A.A. Kiselev and K.W. Kim, Phys. Rev. B **61**, 13115 (2000)

[19] J. Schliemann, J.C. Egues, and D. Loss, Phys. Rev. Lett. **90**, 146801 (2003)

[20] V.A. Froltsov, Phys. Rev. B **64**, 45311 (2001); A.A. Burkov and L. Balents, Phys. rev. B **69**, 245312 (2004)

[21] F.E. Meijer, A.F. Morpurgo, T.M. Klapwijk, T. Koga, and J. Nitta, Phys. Rev. B **70**, 201307(R) (2004); see Chapter 7 of this Thesis.

[22] M.I. Dyakonov and V.I. Perel, Sov. Phys. JETP **33**, 1053 (1971); Sov. Phys. Solid State **13**, 3023 (1972)

[23] Y.K. Kato, R.C. Myers, A.C. Gossard, and D.D. Awschalom, Science **306**, 1910 (2004); J. Wunderlich, B. Kaestner, J. Sinova, and T. Jungwirth, Phys. Rev. Lett. **94**, 47204 (2005)

[24] Y. Aharonov and D. Bohm, Phys. Rev. **115**, 485 (1959)

[25] S.V. Iordanskii, Y.B. Lyanda-Geller, and G.E. Pikus, JETP **60**, 206 (1994)

[26] J.B. Miller, D.M. Zumbuhl, C.M. Marcus, Y.B. Lyanda-Geller, D. Goldhaber-Gordon, K. Campman, and A.C. Gossard, Phys. Rev. Lett. **90**, 76807 (2003)

[27] T. Koga, J. Nitta, and H. Takayanagi, Phys. Rev. Lett. **88**, 126601 (2002); P. Streda and P. Seba, Phys. Rev. Lett. **90**, 256601 (2003)

[28] See, e.g., J.A. Folk, S.R. Patel, S.F. Godijn, A.G. Huibers, S.M. Cronenwett, C.M. Marcus, K. Campman, and A.C. Gossard, Phys. Rev. Lett. **76**, 1699 (1996)

[29] See, e.g., I. L. Aleiner and V. I. Falko, Phys. Rev. Lett. **87**, 256801 (2001)

[30] A.G. Aronov and Y.B. Lyanda-Geller, Phys. Rev. Lett. **70**, 343 (1993)

[31] H.A. Engel and D. Loss, Phys. Rev. B **62**, 10238 (2000)

[32] Y. Kato, R.C. Myers, A.C. Gossard, and D.D. Awschalom, Nature **427**, 50 (2004)

[33] G.M. Minkov, A.V. Germanenko, O.E. Rut, A.A. Sherstobitov, L.E. Golub, B.N. Zvonkov, and M. Willander, Phys. Rev. B **70**, 155323 (2004); see also Chapter 7 of this Thesis.

[34] J. Nitta, F.E. Meijer, and H. Takayanagi, Appl. Phys. Lett. **75**, 695 (1999)

Chapter 2

Theoretical concepts

2.1   Introduction

In this Thesis we have investigated the influence of the Rashba SOI and Zeeman coupling on phase-coherent electron transport, and on the spin dynamics in 2D electron gases (2DEG). As we will outline in this Chapter, the spin dynamics in diffusive 2DEGs depends critically on the interplay between Rashba SOI and Zeeman coupling. It is the spin dynamics in turn, that determines many of the phase-coherent transport properties of the electrons. This Chapter is therefore organized as follows: First, we will give a very brief overview of the characteristics of Rashba SOI, followed by a description of the spin dynamics in the presence of Rashba SOI and Zeeman coupling, with a focus on the spin-relaxation process. Then we will outline the concepts of quantum interference, and the role of the spin dynamics in the interference process. Here, we will also discuss the influence of the spin dynamics on (phase-coherent) Aharonov-Bohm oscillations in more detail. Finally, we will go deeper into the microscopic origin of Rashba SOI, by outlining the bandstructure calculations that allows to determine the Rashba SOI strength in arbitrary quantum wells.

2.2   Rashba spin-orbit interaction

When electrons are confined to a thin layer (2DEG) by an *asymmetric* confinement potential, their spin- and orbital degrees of freedom are coupled. This effect is known as Rashba SOI. Its precise origin, and the strength of the Rashba SOI, will be discussed in detail in Chapter 2.9. Here we just state that Rashba SOI is described by the following Hamiltonian [1]

$$\hat{H}_R \;=\; \alpha \left(\boldsymbol{p} \times \boldsymbol{\sigma} \right) \cdot \hat{z} \tag{2.1}$$

where $\boldsymbol{p} = -i\hbar \boldsymbol{\nabla}$ is the momentum operator, and $\boldsymbol{\sigma} = (\hat{\sigma}_x, \hat{\sigma}_y, \hat{\sigma}_z)$ is a vector of the Pauli spin matrices. The value of α depends on details of the quantum well (see Ch. 2.9). In the absence of Zeeman coupling and elastic scattering, the total Hamiltonian of electrons is given by $\hat{H} = \hat{H}_{kin} + \hat{H}_R$, or explicitly

$$\hat{H} \;=\; \frac{\boldsymbol{p}^2}{2\,m} \;+\; \alpha \left(\boldsymbol{p} \times \hat{\boldsymbol{\sigma}} \right) \cdot \hat{z} \;=\; \frac{p_x^2 \;+\; p_y^2}{2\,m} \;+\; \alpha \left(\hat{\sigma}_x\, p_y - \hat{\sigma}_y\, p_x \right) \tag{2.2}$$

Diagonalizing this Hamiltonian yields the following energy spectrum:

$$E(\boldsymbol{k}) \;=\; \frac{\hbar^2\, \boldsymbol{k}^2}{2\,m} \;\pm\; \alpha\, |\boldsymbol{k}| \tag{2.3}$$

where the plus and minus sign correspond to the two possible spin directions (the spin eigenstates are pointing perpendicular to **k** and in the plane of the
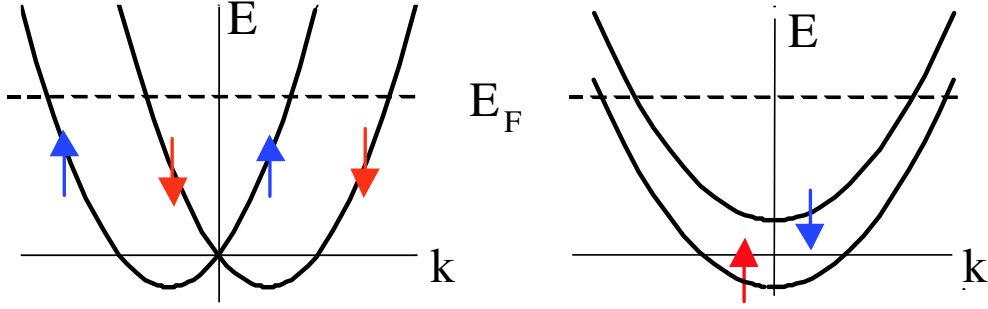
Figure 2.1: The 1D dispersion relations of a degenerate electron gas in the presence of Rashba SOI (left) or Zeeman coupling (right). The arrows indicate the spin-up and spin-down states (for Zeeman coupling the spin-up state is pointing parallel to **B**, for Rashba SOI it is pointing in the direction of $\mathbf{k} \times \hat{\mathbf{z}}$). For a finite Fermi energy E_F, Rashba SOI does not lead to spin-polarization, in contrast to Zeeman coupling.

2DEG). It follows that Rashba SOI leads to lifting of the spin-degeneracy in the conduction band, even in the absence of an external magnetic field. Specifically, Rashba SOI results in a spin-splitting $\Delta = 2\,\alpha\,|\mathbf{k}|$. The (1D) dispersion relation is shown on the left side of Fig. 2.1. It consist of two parabolas that are shifted horizontally with respect to each other. For comparison, the dispersion relation in the presence of (only) Zeeman coupling is shown on the right hand side of Fig. 2.1. In this case, the parabolas are shifted vertically with respect to each other. This difference in shift-direction has an important consequence; Zeeman coupling leads to spin-polarization of the electron gas (i.e., the number of spin-up and spin-down electrons is different), whereas the presence of Rashba SOI does *not* result in spin-polarization. The (mathematical) reason for this is that Rashba SOI does not break time-reversal symmetry, in contrast to Zeeman coupling [2].

2.3 Dyakonov-Perel spin relaxation mechanism

From the above it follows, that Rashba SOI can be viewed as an internal magnetic field $\boldsymbol{B}_R$ acting on the spin, with $\boldsymbol{B}_R = \frac{\alpha}{\mu}\,(\boldsymbol{p} \times \hat{z})$ (and μ is the magnetic moment). The Rashba field $\boldsymbol{B}_R$ is thus always pointing perpendicular to the momentum direction $\boldsymbol{p}$, and in the plane of the 2DEG. In a diffusive 2DEG the momentum direction $\boldsymbol{p}$ of the electron changes frequently, and hence so does the direction of $\boldsymbol{B}_R$ around which the spin is precessing. Due to these random fluctuations of $\boldsymbol{B}_R$ in time - and the resulting random spin rotations in time - the spin looses the memory of its initial spin direction, i.e., the fluctuations in $\boldsymbol{B}_R$ results in

spin relaxation. This mechanism is called the Dyakonov-Perel spin relaxation mechanism [3, 4], and is the main cause of spin relaxation in (slightly) disordered 2DEGs with Rashba SOI (for other mechanisms see Ch. 2.3.1).

From the above picture of the Dyakonov-Perel (DP) mechanism, we can make the following quantitative estimate of the resulting spin relaxation time. The spin is initially precessing around a certain direction of $\boldsymbol{B}_R$ with a typical frequency ω and during a typical time τ (Here, ω is of the order $\mu|\boldsymbol{B}_R|/\hbar = \Delta/\hbar$, and τ is the typical elastic scattering time). After a time τ, i.e., after a scattering event, the direction of $\boldsymbol{B}_R$ changes randomly, and the spin starts precessing around the new direction of $\boldsymbol{B}_R$. Hence, after a certain number of scattering events there is no correlation anymore between the initial and final spin states. The precise time-scale on which the spin looses its memory depends on the parameter $\omega\tau = \Delta\tau/\hbar$, which is the typical angle of spin precession between scattering events. For $\Delta\tau/\hbar \ll 1$, the precession angle between succeeding scattering events is small, so that the spin vector experiences a slow angular diffusion. During a time interval t, the number of random steps is t/τ. For uncorrelated steps in the precession angle we have to sum the (random) squared precession angles $(\Delta\tau/\hbar)^2$, and hence the total squared precession angle after time t is $(\Delta\tau/\hbar)^2 \, t/\tau$. The spin relaxation time τ_s can be defined as the time at which the total precession angle becomes of the order of unity, and hence is given by $1/\tau_s \cong \Delta^2\tau/\hbar$. A more accurate calculation (assuming point-like scatterers) shows that $1/\tau_{s,x} = 1/\tau_{s,y} = 1/2\tau_{s,z} = \Delta^2\tau/2\hbar$, where $\tau_{s,x,y,z}$ are the relaxation time of the x, y, and z component of the spin (see e.g. [5, 6]).

In the opposite limit, i.e., when $\Delta\tau/\hbar \gg 1$, the spin will rotate many times around $\boldsymbol{B}_R$ before the next scattering event takes place. This implies that the spin projection transverse to $\boldsymbol{B}_R$ is reversibly lost (on average) after time $\hbar/\Delta$, while its projection along the direction of $\boldsymbol{B}_R$ is conserved. When the electron is scattered after time τ, the direction of $\boldsymbol{B}_R$ is changed, and the initial spin polarization will completely and irreversibly disappear. Hence, for this case we have $\tau_s \cong \tau$.

Summarizing, the DP mechanism is characterized by the following three characteristics. First, the spin relaxation time becomes longer for shorter values of the scattering time τ (assuming $\Delta\tau/\hbar \ll 1$), i.e., in heavily diffusive systems the DP spin relaxation mechanism is weakened. This feature makes it distinguishable from the other spin relaxation mechanisms (see below). Secondly, note that the spin diffusion length L_s is independent of scattering time τ, despite the fact that the spin relaxation time is enhanced by increasing the scattering rate. We have $L_s = \sqrt{D\,\tau_s} = \sqrt{v_F^2\,\tau\,\tau_s/2} = \hbar v_F/\Delta = \hbar^2/2m^*\alpha$. Hence, in 2DEGs the spin diffusion length only depends on the Rashba SOI strength α (with $\Delta = 2\alpha k_F$).

Third, note that in pure 1D case the direction of $\boldsymbol{B}_R$ (and hence spin rotation axis) is fixed. Consequently, the DP spin relaxation mechanism is absent in 1D systems. More general, it has been shown theoretically that the spin relaxation time is enhanced substantially when the electron motion is confined to a wire with a width that is smaller than the spin precession length L_s [7].

2.3.1 Other spin relaxation mechanisms

Another important spin relaxation mechanism in n-type semiconductors is the Elliott-Yafet (EY) mechanism [8]. The EY mechanism originates from the Pauli SO term which makes that the exact Bloch state is not a spin eigenstate but a superposition of spin-states, i.e., Pauli SO leads to mixing of wavefunctions of opposite spin (see Ch. 2.8). This results in a finite spin-flip probability when the spatial part of the wavefunction experiences a transition through scattering, even if the scattering process itself is spin-independent. Since spin-flip events are induced by momentum scattering, the EY mechanism results in a spin relaxation time that is proportional the (momentum) scattering time τ, i.e., $\tau_s \propto \tau$. This different dependent on τ makes the EY and the DP mechanisms experimentally distinguishable, and reflects the fact that in the EY mechanism the spin rotation occurs during scattering, whereas in the DP case the rotation happens between scattering events (see also [9]).

In epitaxially grown quantum wells, with relatively long scattering times and strong Rashba SOI, the Dyakonov-Perel mechanism is generally the dominant cause for spin relaxation. Below, we will therefore mainly focus on the DP mechanism, and assume that the Elliot-Yafet mechanism can be neglected.

2.4   Effect of a magnetic field on spin relaxation

In the above discussion we have assumed that only Rashba SOI is present, and that there is no additionally applied external magnetic field. When also an external magnetic field $\boldsymbol{B}_R$ is applied, two things will change: (1) the spin will now precess around the vectorial sum of the internal and external field ($\boldsymbol{B}_R + \boldsymbol{B}$), and (2) the electron motion will generally be affected by the external magnetic field $\boldsymbol{B}$. Both these effects have an impact on the spin relaxation process.

Since the spin precesses around the vectorial sum of the internal and external field ($\boldsymbol{B}_R + \boldsymbol{B}$), Zeeman coupling makes that the spin precession axis is less randomized by elastic scattering, as compared to the case where $\boldsymbol{B}$. Hence, the spin relaxation time can be expected to become longer.

In addition, when the external magnetic field $\boldsymbol{B}$ is applied perpendicular to the 2DEG, the electron will move along circular orbits, with the cyclotron frequency $\omega_c = e|\boldsymbol{B}|/m^*$. For $\omega_c \tau \gg 1$ the elastic scattering does not play a role anymore, and consequently $\boldsymbol{B}_R$ is always pointing in the radial direction. Since the direction of $\boldsymbol{B}_R$ is not randomized anymore but is now deterministic, the DP spin relaxation mechanism will be suppressed [5, 6].

Theoretically, the effect of a magnetic field on the spin relaxation time is usually obtained by solving the kinetic rate equation for a spin-dependent density matrix. For a 2DEG with Rashba SOI, which is subject to a large perpendicular magnetic field, and with $\Delta^2 \tau/\hbar \ll E_Z \ll E_F$, the spin relaxation rates are given by (assuming a negative g-factor) [6]

$$
\begin{aligned}
\frac{1}{\tau_{s,z}} &= \frac{\Delta^2 \tau}{\hbar^2} \frac{1}{1 + (\omega_c + \omega_L)^2\, \tau^2} \\[2ex]
\frac{1}{\tau_{s,\parallel}} &= \frac{\Delta^2 \tau}{2\hbar^2} \frac{1}{1 + \omega_c^2\, \tau^2}
\end{aligned}
\tag{2.4}
$$

where ω_L is the Larmor frequency, and $\tau_{s,z}$ and $\tau_{s,\parallel}$ are the relaxation times of the spin components perpendicular to the 2DEG, and in the plane of the 2DEG, respectively. From the above expressions it follows that the orbital effect enhances all spin relaxation times, whereas the Zeeman coupling enhances only the relaxation time of the spin components along the applied magnetic field. Note, that generally $\omega_c \gg \omega_L$, and hence the magnetic field has the largest impact on the spin relaxation times via its effect on the orbital motion of electrons.

The situation is different when we apply the magnetic field $\boldsymbol{B}$ *in* the plane of the 2DEG. For a thin enough quantum well the orbital effects due to the magnetic field are absent, and only the Zeeman coupling remains. For this case, and in the limit that $E_F \gg \Delta^2 \tau/\hbar \gg E_Z$, the relaxation time of the perpendicular spin component is calculated to be [10]

$$
\frac{\tau_{s,z}(B_\parallel)}{\tau_{s,z}(0)} \approx 1 + \frac{1}{2}\,(E_Z/E_{SOI})^2
\tag{2.5}
$$

where $E_{SOI} \equiv \hbar/\tau_s(0) = \Delta^2 \tau/2\hbar$. The relaxation times of the other spin components have not yet been examined. Hence, the spin relaxation time is determined by the competition between only two energy scales; the Zeeman energy and the a Rashba SOI related energy scale, and is independent of other details.

2.5   Quantum interference (excl. spin-dynamics)

When the temperature is low enough ($\approx 1\,\mathrm{K}$), the phase-coherence length of electrons becomes much larger than the mean free path. In this limit, quantum interference phenomena give rise to a deviation from the classical picture of electron transport, that is characterized by the Drude conductivity. The sign of the deviation depends on the spin dynamics. The study of these conductivity corrections, known as weak(anti-)localization, can therefore provide valuable information about the spin dynamics in experimental systems. Below we outline the important concepts, and will highlight the influence of the spin degree of freedom, in particular the role of Rashba SOI and Zeeman coupling. For a more complete review on this topic, and details, we refer the reader to Refs. [11, 12].

2.5.1   Conductivity correction in the absence of spin

Consider the quantum mechanical probability for an electron to go from A to B. This probability is obtained by squaring the modulus of the sum of the all probability amplitudes for an electron to pass along all possible paths (see Fig. 2.2). Neglecting the spin degree of freedom we therefore have

$$P_{A \to B} \;=\; |\sum_i A_i|^2 \;=\; \sum_i |A_i|^2 + \sum_{i \neq j} A_i A_j^* \tag{2.6}$$

The first term is the classical probability to go from A to B, and the second term is the quantum mechanical correction. To evaluate the value to the interference term, it is convenient to split the summation into two parts; paths that do self-intersect, and paths that do not (see Fig. 2.2). The summation over non-self-intersecting paths averages to zero, because the phase difference $\Delta\phi$ between each pair of scattering paths is large and random (the difference in length ΔL of the paths results in a stochastic phase difference $\Delta\phi \approx k_F \Delta L$).

In contrast, the interference of self-intersecting paths does *not* average to zero. Each self-intersecting path is characterized by a pair of probability amplitudes, say A_1 and A_2, that correspond to the amplitude of passing the loop clockwise and anti-clockwise. For these waves we have $A_1 = A_2$, independent of the length of the loop, since the length of the two time-reversed paths is identical ($\Delta L = 0$). Consequently, the probability to find a particle at the crossing X becomes

$$P \;=\; |A_1 + A_2|^2 \;=\; |A_1|^2 + |A_2|^2 + 2|A_1||A_2|\cos(\phi_1 - \phi_2) \;=\; 4\,|A_1|^2 \tag{2.7}$$
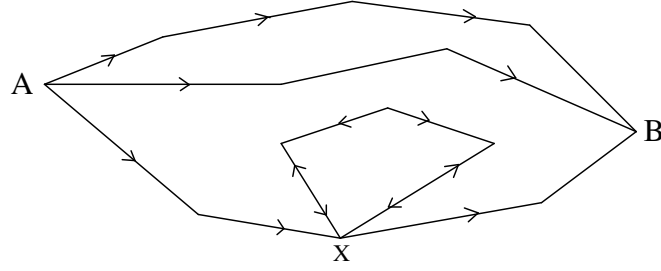
Figure 2.2: A sketch of various semiclassical paths for an electron to go from A to B. At point X the path is self-intersecting. The incoming wave at X will split into two parts which traverse the loop in opposite directions (indicated by the arrows). The interference between these time-revered waves will affect the return probability to X and hence affects the total probability for a particle to go from A to B.

Hence, the probability of finding the particle at X is enhanced by a factor two, and consequently the probability to find it at point B is reduced, i.e., the conductivity is reduced below its classical value.

Since only the interference of time-reversed (or self-intersecting) paths affects the conductivity, the magnitude of the conductivity correction depends on the probability of an electron to return to its starting point. Assuming Brownian motion [13], the dynamics is described by the diffusion equation

$$\left(\frac{\partial}{\partial t} - D \frac{\partial^2}{\partial \boldsymbol{r}^2} \right) W(\boldsymbol{r}, t) \;=\; \delta(\boldsymbol{r}) \, \delta(t) \tag{2.8}$$

where $W(\boldsymbol{r}, t)$ denotes the probability of finding the particle at a position $\boldsymbol{r}$ from the origin after a time-interval t. The solution of Eq. (2.8) is

$$W(\boldsymbol{r}, t) \;=\; \frac{1}{(4\pi Dt)^{d/2}} \; \exp\left(\frac{\boldsymbol{r}^2}{4Dt} \right) \tag{2.9}$$

Hence, the return-probability after time t is (in d-dimensions) given by $W(0, t) = (4\pi Dt)^{-d/2}$. To account for the fact that on time scales shorter or comparable to the elastic scattering time τ the diffusion approximation does not hold, the above value has to be multiplied by $[1 - \exp(-t/\tau)]$. Furthermore, the interference between time-reversed path must take place within the inelastic scattering time τ_ϕ. This condition can be taken into account by an additional factor $\exp(-t/\tau_\phi)$. Hence, the interference correction to the Drude conductivity is

$$\Delta\sigma \;=\; -\frac{e^2}{2\pi^2\hbar} \int \frac{1}{(4\pi Dt)^{d/2}} \; \exp(t/\tau_\phi)[1 - \exp(t/\tau)] \; dt \tag{2.10}$$

For 2D electron gases or thin metallic films we obtain from Eq. (2.10)

$$\Delta\sigma = -\frac{e^2}{2\pi^2\hbar}\ln(\tau_\phi/\tau + 1) \tag{2.11}$$

2.5.2 Effect of a perpendicular magnetic field

A small magnetic field, applied perpendicular to the 2D electron gas, will not affect the classical motion of electrons. It does change, however, the phase of the probability amplitude of the paths. Specifically we have

$$A_1 \rightarrow A_1 \exp\left(i\frac{e}{\hbar}\oint \boldsymbol{A}\cdot d\boldsymbol{l}\right) = A_1 \exp\left(i\frac{\pi\boldsymbol{B}\cdot\boldsymbol{S}}{\Phi_0}\right) \tag{2.12}$$

where $\boldsymbol{A}$ is the vector potential, $\Phi_0 = h/2e$ is the elementary quantum of magnetic flux, and $\boldsymbol{B}\cdot\boldsymbol{S}$ is the magnetic flux Φ enclosed by the scattering path. For the time-reversed path $d\boldsymbol{l} \rightarrow -d\boldsymbol{l}$, and hence the phase difference becomes $\Delta\phi(B) = 2\pi\Phi/\Phi_0$; i.e., $\Delta\phi$ does no longer vanish for all time-reversed paths, but depends now on the enclosed flux. Consequently, the sum over all time-revered paths that enclose roughly one flux quantum or more, will average to zero; i.e., a magnetic flux suppresses the weak-localization correction.

The theoretical expression for the conductivity correction in the presence of a magnetic field can be obtained by substituting $\boldsymbol{p} \rightarrow \boldsymbol{p} + e\boldsymbol{A}$, i.e.

$$\left[\frac{\partial}{\partial t} + D\left(-i\frac{\partial}{\partial \boldsymbol{r}} - \frac{2e}{\hbar}\boldsymbol{A}(\boldsymbol{r})\right)^2 + \frac{1}{\tau_\phi}\right]W(\boldsymbol{r},t) = \delta(\boldsymbol{r})\,\delta(t) \tag{2.13}$$

For a 2DEG or thin film we consequently obtain (see e.g. [12, 11])

$$\Delta\sigma(B) = -\frac{e^2}{2\pi^2\hbar}\left\{\Psi\left(\frac{1}{2} + \frac{\tau_B}{\tau}\right) - \Psi\left(\frac{1}{2} + \frac{\tau_B}{\tau_\phi}\right)\right\} \tag{2.14}$$

where $\Psi(x)$ denotes the Digamma function, with $\Psi(x) = \sum_n(n+x)^{-1}$, and $\tau_B = \hbar/4eDB$. This expression gives the magnetoconductance at small values of B, and hence allows to determine τ_ϕ experimentally.

2.5.3 Effect of an in-plane magnetic field

Experimental systems always have a finite width and are not perfectly 2D. Hence, an in-plane magnetic field $B_\parallel$ does not only cause Zeeman coupling to the spin,
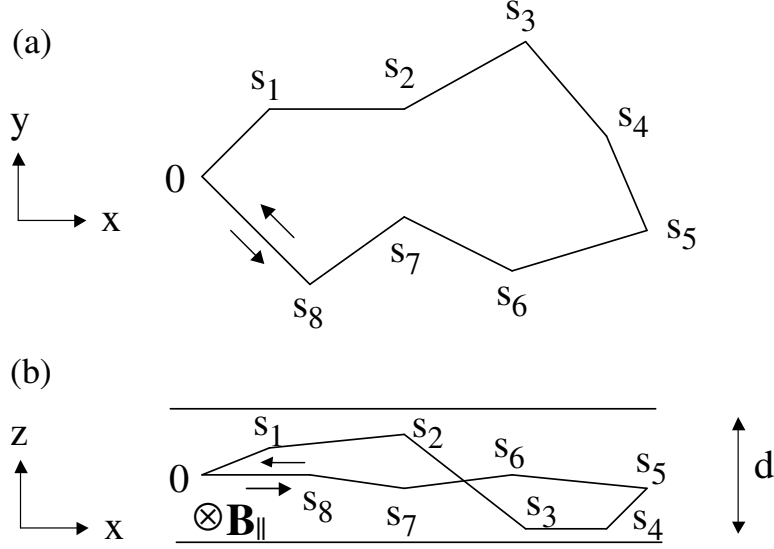
Figure 2.3: An example of a time-reversed trajectories, where scattering events are denoted by "s". The topview of the trajectory is sketched in (a), whereas the electron motion in the lateral direction is indicated in (b). The thickness of the sample is denoted by "d". The lateral electron motion results in enclosure of magnetic flux, and hence causes dephasing of the time-reversed paths.

but also results in a magnetic flux through the quantum well or metal film, which affects quantum interference.

Consider a thin metal film with thickness d in the presence of $B_\parallel$ (see Fig. 2.3). The vector potential can then be chosen as $\boldsymbol{A}(r) = (0, -(z - d/2)B_\parallel, 0)$. Inserting this into Eq. (2.13), and noting that we can neglect the z-dependence of $W(\boldsymbol{r}, t)$ for $D \ll l_\phi$, we obtain the following effective 2D diffusion equation [12]

$$\left[\frac{\partial}{\partial t} - D \left(\frac{\partial^2}{\partial x^2} + \frac{\partial^2}{\partial y^2} \right) + \frac{1}{\tau_\phi} + \frac{1}{\tau_{B_\parallel}} \right] W(\boldsymbol{r}, t) = \delta(\boldsymbol{r})\,\delta(t) \tag{2.15}$$

where $1/\tau_{B_\parallel}$ is given by

$$\frac{1}{\tau_{B_\parallel}} = D\left(\frac{2e}{\hbar}\right)\frac{1}{d} \int_0^d dz\,\boldsymbol{A}^2(z) = \frac{D}{3}\left(\frac{ed}{\hbar}\right)^2 B_\parallel^2 \tag{2.16}$$

Clearly, from Eq. (2.15) it follows that the in-plane magnetic field results in a phase-breaking rate ($\propto B_\parallel^2$), which adds to the inelastic rate $1/\tau_\phi$.

In the above derivation it was implicitly assumed that the electronic probability distribution is uniform over the thickness of the sample, and hence Eq. (2.16) is only (approximately) valid for thin metal films. In narrow quantum wells with perfect interfaces, electrons occupy well defined subbands $\Psi_n(z)$, and hence the center of mass of the electrons does not dependent on its motion in the xy plane. In case of finite surface roughness, however, the motion in the along the z-axis becomes coupled to its motion in the xy plane, similar as depicted in Fig. 2.6. Hence, surface roughness results in a non-vanishing dephasing rate. The surface roughness can be characterized by two parameters Δ and L, where Δ is the root-mean-square of the fluctuation height, and L is the distance over which the fluctuations are correlated. For $L \ll l_{tr}$ (with l_{tr} is the mean free path), it has been predicted that the dephasing rate is given by [14]

$$\frac{1}{\tau_{B_\parallel}} \approx \sqrt{\pi}\,\frac{e^2}{\hbar^2}\,v_F\,\Delta^2\,L\,B_\parallel^2 \tag{2.17}$$

where v_F is the Fermi velocity. Also in this case the dephasing rate is proportional to $B_\parallel^2$, but it does not depend on the thickness d of the quantum well.

Apart from surface roughness, also other mechanisms can cause dephasing of time-reversed waves, such as a z-dependence in the scattering potential [15], and an asymmetric confinement potential of the electrons in the quantum well [15]. In practice, however, surface roughness is often the dominant mechanism.

From the above it follows that $B_\parallel$ enhances the effective dephasing rate of time-revered waves $(1/\tau_\phi \rightarrow 1/\tau_\phi + 1/\tau_{B_\parallel})$, and hence suppresses quantum interference, analogous to a perpendicular field. As we will show in Chapter 2.6.3, the competition between Rashba SOI and Zeeman coupling adds *another* term to the dephasing rate.

2.6 Quantum interference (incl. spin-dynamics)

In the above discussion we have neglected the spin degree of freedom. If we would take into account also Zeeman coupling - but no Rashba SOI - the above results would be identical (for $E_Z \tau/\hbar \ll 1$). This is because in the presence of (only) Zeeman coupling the spin is a good quantum number, and interference takes place within each spin subband separately. Hence, the phase-shift in the wavefunction due to the Zeeman energy is equal for both time-reversed waves. Zeeman coupling *alone* is therefore not expected to result in any dephasing.

In contrast, the presence of SOI makes that the spin is not a conserved quantity, and the spin precesses around the randomly fluctuating field $\boldsymbol{B}_R$. This leads

to mixing of the spin subbands in the interference process, and has a profound impact on quantum interference. Specifically, the interference correction to the Drude conductivity changes sign, i.e., weak localization (WL) becomes weak anti-localization (WAL) in the presence of strong SOI (see e.g. [11, 12, 16]).

The origin of the sign-change lies in the fact that the spin evolution of waves travelling along time-reversed paths is *not equal* (see Ch. 2.6.1. for a more formal description). If we consider SOI due to impurities, the spin rotates slightly during each scattering event, and will have a certain spin direction when it arrives back at the origin. The time-reversed wave scatters at the same points, but in the opposite time-order. Consequently, also the spin rotations at the scatters occur in the opposite time-order. Since 3D spin rotations do not commute (or equivalently, Pauli spin matrices do not commute), the final spin directions of the time-revered waves is *not* the same when they arrive back at the origin. In fact, for strong SOI the angle between the two final spin directions is more often 2π than 0, resulting - on average - in destructive interference (WAL).

2.6.1 Path integral technique

There are several techniques to obtain the interference correction in the presence of SOI. The most transparent method is probably based on a path integral technique, analogous to Chapter 2.5, but now with the spin explicitly taken into account. This Chapter is largely based on work by Chakravarty and Schmid [12].

The propagation amplitude of an electron is given by the following Feynman path integral

$$K = \int \mathrm{d}\boldsymbol{r_t} \; \mathrm{T} \exp(\frac{i}{\hbar} S[\boldsymbol{r}_t, \boldsymbol{\sigma}_t]) \tag{2.18}$$

where T denotes time ordering, and S is the action (which generally depends on the position and spin direction). This quantity is the generalization of "'A_i'" in Chapter 2.5. Including the spin, we obtain the following expression for the (quasi) return probability $\tilde{W}_{\boldsymbol{r}_t}$ ($= A_t A_{-t}^*$) for a given scattering path $\boldsymbol{r}_t$

$$
\begin{aligned}
\tilde{W}_{\boldsymbol{r}_t} &= \frac{1}{2} \sum_{\sigma,\sigma'=\uparrow,\downarrow} \langle\sigma| \, \mathrm{T} \exp(\frac{i}{\hbar} S[\boldsymbol{r}_t, \boldsymbol{\sigma}_t]) \, |\sigma'\rangle \langle\sigma| \, \mathrm{T} \exp(\frac{i}{\hbar} S[\boldsymbol{r}_{-t}, \boldsymbol{\sigma}_t]) \, |\sigma'\rangle^* \\
&\qquad\qquad\qquad\qquad\qquad\qquad\qquad\qquad\qquad\qquad\qquad\qquad\qquad (2.19) \\
&= \frac{1}{2} \sum_{\sigma,\sigma'=\uparrow,\downarrow} \langle\sigma| \, \mathrm{T} \exp(\frac{i}{\hbar} S[\boldsymbol{r}_t, \boldsymbol{\sigma}_t]) \, |\sigma'\rangle \langle\sigma'| \, \mathrm{T} \exp(-\frac{i}{\hbar} S^*[\boldsymbol{r}_t, \boldsymbol{\sigma}_t]) \, |\sigma\rangle
\end{aligned}
$$

In the last step we used the property that the adjoint of a time ordered sequence leads to an anti-time-ordered sequence: $\{\mathrm{T}f[\boldsymbol{r}_t]\}^* = \mathrm{T}_a f^*[\boldsymbol{r}_t] = \mathrm{T}f^*[\boldsymbol{r}_{-t}]$. This

form allows to consider the product of two matrix elements as a matrix element of the direct product of two spins. Hence, we can write the quasi return probability (for a single scattering path) in the following way

$$
\tilde{W}_{\boldsymbol{r}_t} = \frac{1}{2} \sum_{\sigma^a, \sigma^b = \uparrow, \downarrow} \langle \sigma^a \sigma^b | \, \mathrm{T} \, \exp \big[\frac{i}{\hbar} (S[\boldsymbol{r}_t, \boldsymbol{\sigma}_t^a] - S^*[\boldsymbol{r}_t, \boldsymbol{\sigma}_t^b]) \big] \, | \sigma^b \sigma^a \rangle
$$

$$
= \frac{1}{2} \sum_{\sigma^a, \sigma^b = \uparrow, \downarrow} \langle \sigma^a \sigma^b | \, \mathrm{T} \, \exp \big[i \int dt \, \boldsymbol{\Omega}(\dot{\boldsymbol{r}}_t, \boldsymbol{r}_t) \cdot (\boldsymbol{\sigma}_t^a + \boldsymbol{\sigma}_t^b) \big] \, | \sigma^b \sigma^a \rangle
$$

(2.20)

In the last step the kinetic part in the action drops out, since it is real. The only remaining term in the action stems from the SOI term, and is here assumed to have the form: $H_{SOI} \propto (\nabla V(\boldsymbol{r}_t) \times \dot{\boldsymbol{r}}_t) \cdot \boldsymbol{\sigma}_t \propto \hbar \, \boldsymbol{\Omega}(\dot{\boldsymbol{r}}_t, \boldsymbol{r}_t) \cdot \boldsymbol{\sigma}_t$.

To find the total quasi probability for returning to the starting point in time t_0 we have to average Eq. (2.20) over all possible scattering paths $\boldsymbol{r}_t$ that return to the origin in time t_0. In doing so, first notice that $(\boldsymbol{\sigma}_t^a + \boldsymbol{\sigma}_t^b)$ is the total spin, which does not depend on time and can be taken out of the integral (and drop the index t). This also makes the time-ordering operation superfluous, and can be neglected from now on. Furthermore, note that for a Gaussian distributed variable ϕ, we have $\langle\langle \exp[i\phi] \rangle\rangle = \exp[-\langle\langle \phi^2 \rangle\rangle/2]$, where $\langle\langle \, \rangle\rangle$ denotes averaging. Hence, assuming $\boldsymbol{\Omega}(\dot{\boldsymbol{r}}_t, \boldsymbol{r}_t)$ to be Gaussian distributed, we find

$$
\tilde{W}_{t_0} = \frac{1}{2} W_{t_0} \sum_{\sigma^a, \sigma^b = \uparrow, \downarrow} \langle \sigma^a \sigma^b | \langle\langle \, \exp \big[i(\boldsymbol{\sigma}^a + \boldsymbol{\sigma}^b) \cdot \int_{-t_0/2}^{t_0/2} dt \, \boldsymbol{\Omega}(\dot{\boldsymbol{r}}_t, \boldsymbol{r}_t) \big] \, \rangle\rangle_{t_0} | \sigma^b \sigma^a \rangle
$$

$$
= \frac{1}{2} W_{t_0} \sum_{\sigma^a, \sigma^b = \uparrow, \downarrow} \langle \sigma^a \sigma^b | \, \exp \big[- (\boldsymbol{\sigma}^a + \boldsymbol{\sigma}^b)^2 \frac{t_0}{6 \, \tau_s} \big] \, | \sigma^b \sigma^a \rangle
$$

(2.21)

where W_{t_0} is the classical return probability, i.e., without taking the phase into account. Here we have also introduced the spin relaxation rate $1/\tau_s$, which is proportional to $\boldsymbol{\Omega}^2$ [12].

Since the eigenstates of the total spin are the singlet $|0, 0\rangle$ and triplet states $|1, 1\rangle, |1, 0\rangle, |1, -1\rangle$, it is convenient to rewrite $|\sigma^a \sigma^b\rangle$ in this basis. We have $|\uparrow\uparrow\rangle = |1, 1\rangle$, and $|\downarrow\downarrow\rangle = |1, -1\rangle$. Furthermore, we can write

$$| \uparrow \downarrow \rangle \;=\; \frac{1}{2} \left(| \uparrow \downarrow \rangle + | \downarrow \uparrow \rangle \right) \;+\; \frac{1}{2} \left(| \uparrow \downarrow \rangle - | \downarrow \uparrow \rangle \right)$$

$$\quad\;=\; \frac{1}{\sqrt{2}} | 1, 0 \rangle \;+\; \frac{1}{\sqrt{2}} | 0, 0 \rangle \tag{2.22}$$

$$| \downarrow \uparrow \rangle \;=\; \frac{1}{\sqrt{2}} | 1, 0 \rangle \;-\; \frac{1}{\sqrt{2}} | 0, 0 \rangle$$

Hence, the summation in Eq. (2.21) can alternatively be written in the following way (defining $A \equiv W_{t_0} \exp[-(\boldsymbol{\sigma}^a + \boldsymbol{\sigma}^b)^2 \, t_0 / 6\tau_s]$)

$$2 \, \tilde{W}_{t_0} \;=\; \langle \uparrow\uparrow \, | \, A \, | \, \uparrow\uparrow \rangle + \langle \downarrow\downarrow \, | \, A \, | \, \downarrow\downarrow \rangle + \langle \uparrow\downarrow \, | \, A \, | \, \uparrow\downarrow \rangle + \langle \downarrow\uparrow \, | \, A \, | \, \downarrow\uparrow \rangle \tag{2.23}$$

$$\;=\; \langle 1, 1 | \, A \, | 1, 1 \rangle + \langle 1, 0 | \, A \, | 1, 0 \rangle + \langle 1, -1 | \, A \, | 1, -1 \rangle - \langle 0, 0 | \, A \, | 0, 0 \rangle$$

Hence, the triplets each contribute $\frac{1}{2} W_{t_0} \exp(-4 \, t_0 / 3\tau_s)$ to the quasi return probability, and the singlet gives a *negative* contribution equal to $-\frac{1}{2} W_{t_0}$ (destructive interference). The total quasi return probability is given by [12]

$$\tilde{W}_{t_0} \;=\; \frac{1}{2} W_{t_0} \left[3 \exp(-4 \, t_0 / 3\tau_s) - 1 \right] \tag{2.24}$$

For $t_0 / \tau_s > 1$ the (conductivity-decreasing) interference correction due to the triplet is suppressed, and only the (conductivity-enhancing) interference correction due to the singlet remains. In other words, for a given SOI strength (i.e., τ_s), the self-intersecting scattering paths that are longer that the spin-relaxation length contribute to the enhancement of the conductivity, whereas shorter scattering paths decrease the conductivity (see Fig. 2.4). The total conductivity correction is the sum over all the scattering paths (i.e., all values of t_0), and hence depends on the distribution of scattering path lengths.

If we apply a (small) perpendicular magnetic field, we introduce a phase-shift (see Chapter 2.5.2), which makes that time-reversed paths that enclose one or more flux quanta do no longer contribute to the interference correction. Hence, the long scattering paths that enhance the conductivity in the presence of SOI will dephase first, and consequently the conductivity first decreases with magnetic field. For stronger values of the magnetic field the conductivity increases again, since then also the short scattering paths (which lead to localization) dephase (see Fig. 2.4). This gives rise to the characteristic (non-monotonic) magnetoconductance, as was first derived by Hikami, Larkin and Nagaoka [17].
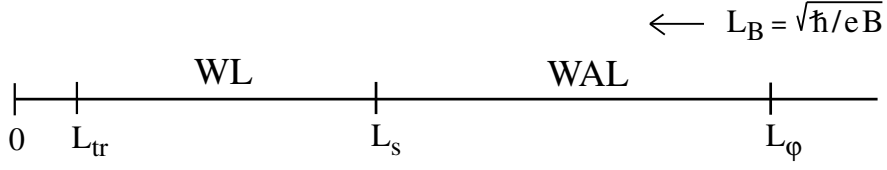
$$\longleftarrow \ L_B = \sqrt{\hbar/e\,B}$$

WL WAL

0 L_{tr}	L_s	L_φ

Figure 2.4: Sketch of the relevant length-scales in quantum interference. The interference of waves travelling along time-reversed paths that are shorter/longer than the spin relaxation length L_s give rise to a decrease/enhancement of the conductivity (WL/WAL). The mean free path L_{tr} and the phase coherence length L_ϕ give respectively the lower and upper bound for quantum interference. When a magnetic field is applied the magnetic length L_B replaces L_ϕ as upper length scale for interference.

2.6.2 Magnetoconductance in presence of Rashba SOI

In the previous section it was implicitly assumed that the SOI is due to impurity scattering. For this type of SOI the spin only rotates slightly during each scattering process, but does not precess between scattering events. This picture of the spin-dynamics is correct for thin metal films [11], but does not hold for quantum wells with Rashba SOI. In the case of Rashba SOI, the spin is precessing around $B_\parallel$ *between* scattering events, and the spin rotation during each scattering event is negligible. The theory for the magnetoconductance in this case was developed by Iordanskii, Lyanda-Geller, and Pikus [18]. Since their derivation is less transparent and more involved than the one above, we refer the reader to the original paper for details. Here we only state that the magnetoconductance as a function of a small perpendicular magnetic field $B_\perp$ (but neglecting Zeeman coupling) is given by (with $\Delta\sigma(B_\perp) = \sigma(B_\perp) - \sigma(0)$)

$$\Delta\sigma(B_\perp) \;=\; -\frac{e^2}{2\pi h}\left\{\frac{1}{a_0} + \frac{2a_0 + 1 + H_s}{a_1(a_0 + H_s) - 2H_s}\right.$$
$$-\sum_{n=1}^{\infty}\left[\frac{3}{n} - \frac{3a_n^2 + 2a_n H_s - 1 - 2(2n+1)H_s}{(a_n + H_s)a_{n-1}a_{n+1} - 2H_s[(2n+1)a_n - 1]}\right]$$
$$\left. + 2\ln H_{tr} \;+\; \Psi(1/2 + H_\phi) \;+\; 3C\right\} \tag{2.25}$$

where C is the Euler constant, and

$$a_n = n + \frac{1}{2} + H_\phi + H_s \qquad H_{s,tr,\phi} = \frac{\hbar}{4eDB_\perp \tau_{s,tr,\phi}} \qquad \frac{1}{\tau_s} = \frac{\Delta^2 \tau_{tr}}{2\hbar^2} \tag{2.26}$$

with τ_{tr} the elastic scattering time, τ_s the Dyakonov-Perel spin-relaxation time, τ_ϕ the inelastic scattering time, and $\Delta = 2\alpha k_F$ the Rashba spin-split energy. We will use Eq. (2.25) frequently in this Thesis to fit the experimental data, and to extract the phase-coherence time τ_ϕ and the spin relaxation time τ_s. For the fit to the ILP theory, we have summed the second line in Eq. (2.25) up to $n = 50.000$ (convergence had been reached).

We note that in the full ILP theory SOI terms proportional to k as well as to k^3 are taken into account. For quantum wells with strong Rashba SOI, we only need to consider the SOI term proportional to k, and the magnetoconductance expression reduces to Eq. (2.25). Specifically, Ω_3 in Ref. [18] can be put equal to 0, and Ω_1 corresponds to $\Delta/2$.

Further, we note that Eq. (2.25) was derived in the diffusion approximation, implying that Eq. (2.25) is only valid for $H_{tr} \ll 1$, i.e., the magnetic flux through an area of the mean-free-path squared ($l_{tr} \times l_{tr}$) should be much smaller than unity. Also, it is assumed that the spin-split energy Δ is much smaller than the impurity broadening, i.e., $\Delta\tau/\hbar \ll 1$ [19]. For the experimental data analysis described in this Thesis both these conditions were always satisfied.

2.6.3 Competition between Rashba and Zeeman coupling

In the above Chapters the additional effect of Zeeman coupling on quantum interference and the magnetoconductance has been neglected. Although Zeeman coupling *alone* is not expected to induce significant changes, the *interplay* between Rashba SOI and Zeeman coupling is predicted to affect quantum interference profoundly [20, 21]. In particular, in the limit that the Zeeman coupling can be treated as a small perturbation in comparison to Rashba SOI, the interplay between Zeeman coupling and Rashba SOI is predicted to cause time-reversal symmetry breaking. In other words, the competition between Zeeman coupling and Rashba SOI is predicted to result in an additional (spin-induced) dephasing rate of time-reversed waves $1/\tau_{B_\parallel,\mathrm{spin}}$, which is given by [21]

$$\frac{\hbar}{\tau_{B_\parallel,\mathrm{spin}}} = \frac{E_Z^2}{E_{SOI}} \tag{2.27}$$

with $E_Z = g^*\mu_B B_\parallel$ is the Zeeman energy, and $E_{SOI} \equiv \hbar/\tau_s = \Delta^2\tau/2\hbar$ is the effective Rashba SOI energy in diffusive systems. This spin-induced dephasing rate, Eq. (2.27), is generally much smaller than the dephasing rate due to the magnetic flux through the 2DEG, assuming a perpendicularly applied magnetic field (see Ch. 2.5.2). When the magnetic field is applied *in* the plane of the

quantum well, however, the dephasing due to the orbital effect of $B_\parallel$ is much smaller (see Ch. 2.5.3), and spin-effects might become visible. In this case, the total dephasing rate of time-reversed waves is given by (with $E_Z \ll E_{SOI}$)

$$\frac{1}{\tau_\phi(B_\parallel)} \quad = \quad \frac{1}{\tau_\phi(0)} \quad + \quad \frac{1}{\tau_{B_\parallel,\text{orbital}}} \quad + \quad \frac{1}{\tau_{B_\parallel,\text{ spin}}} \tag{2.28}$$

$$= \quad \frac{1}{\tau_\phi(0)} \quad + \quad \sqrt{\pi}\,\frac{e^2}{\hbar^2}\,v_F\,\Delta^2\,L\,B_\parallel^2 \quad + \quad \frac{1}{\hbar}\,\frac{E_Z^2}{E_{SOI}} \tag{2.29}$$

Which of these dephasing terms is the dominant depends on the details of the quantum well. If the orbital dephasing mechanism can be neglected (as in our samples; see Ch. 7 and 8), Zeeman coupling results in a suppression of weak anti-localization. In other words, in the presence of strong SOI, additional Zeeman coupling results in a *decrease* in conductivity. Specifically, the change in conductivity is given by [21]

$$\sigma(B_\parallel) - \sigma(0) \quad = \quad -\frac{e^2}{2\pi^2\hbar}\ln\left(1 + \frac{\tau_\phi(0)}{\tau_{B_\parallel,\text{spin}}}\right) \tag{2.30}$$

This equation, and Eqs. (2.28) and (2.29), are only valid for $E_Z \ll E_{SOI}$. So far, there exist no theoretical predictions what happens when the Zeeman energy is *strongly* affecting the spin dynamics, i.e., when $E_Z \gtrsim E_{SOI}$. In Chapters 7 and 8 we will address this situation experimentally.

2.7 Aharonov-Bohm oscillations

In the previous Chapters we have discussed quantum interference phenomena in 2D systems. In this Chapter we focus on interference effects in another kind of structure, namely a ballistic 1D ring. In this case the electron path is well-defined, and the interference between waves moving in opposite direction gives rise to well-known Aharonov-Bohm (AB) magnetoconductance oscillations [22].

The origin of the AB effect lies in the fact that the vector potential modifies the the canonical momentum of an electron, $\boldsymbol{p} \to \boldsymbol{p} + e\boldsymbol{A}$. This results in a change in the acquired phase by the electron after travelling a certain distance. Note, that infinitely many functions $\boldsymbol{A}$ can be found that satisfy $\boldsymbol{B} = \boldsymbol{\nabla} \times \boldsymbol{A}$, and hence the canonical momentum and the acquired phase in the wavefunction of the electron cannot be determined uniquely. However, the *phase difference* between two interfering partial electronic waves, or a particle travelling along a closed loop, is well-defined.

The total phase acquired by an electron propagating along a closed loop is given by (neglecting the spin degree of freedom)

$$\Delta\phi \;=\; \frac{1}{\hbar}\oint \boldsymbol{p}\cdot d\boldsymbol{l} \;=\; \frac{1}{\hbar}\oint (m\boldsymbol{v} + e\boldsymbol{A})\cdot d\boldsymbol{l} \;=\; \Delta\phi_v + \Delta\phi_A \tag{2.31}$$

here the first term is due to the velocity of the electron and the second term comes from the vector potential. This term can be written as

$$\Delta\phi_A \;=\; \frac{e}{\hbar}\oint \boldsymbol{A}\cdot d\boldsymbol{l} \;=\; \frac{e}{\hbar}\oint (\boldsymbol{\nabla}\times\boldsymbol{A})\cdot d\boldsymbol{S} \;=\; \frac{e}{\hbar}\boldsymbol{B}\cdot\boldsymbol{S} \;=\; 2\pi\frac{\Phi}{\Phi_0} \tag{2.32}$$

with $\Phi_0 = h/e$ is the flux quantum, and Φ is the magnetic flux enclosed by the the loop with area S. Note that we do not need to specify $\boldsymbol{A}$ explicitly to obtain the phase difference $\Delta\phi_A$, since only $\boldsymbol{\nabla}\times\boldsymbol{A} = \boldsymbol{B}$ enters in the equation. Notice further that $\oint \boldsymbol{A}\cdot d\boldsymbol{l} = \int_0^\pi \boldsymbol{A}\cdot d\boldsymbol{l} - \int_0^{-\pi} \boldsymbol{A}\cdot d\boldsymbol{l}$, and hence Eq. (2.32) also provides the phase difference between two partial waves travelling along the different arm of a 1D ring. Since a phase difference is only distinguishable Mod(2π), *any* effect will show periodic behavior as a function of the enclosed flux, including the conductance. In first order approximation, the conductance G of the ring is given by

$$G(B) \;\propto\; P_{A\to B} \;=\; |A_1 + A_2|^2 \;=\; 2|A_1|^2\left[1 + \cos(\Delta\phi_A + \Delta\phi_v)\right]$$
$$\tag{2.33}$$
$$=\; 2|A_1|^2\left[1 + \cos(2\pi\Phi/\Phi_0 + \Delta\phi_v)\right]$$

assuming $|A_1| = |A_2|$, and with $\Delta\phi_v$ is either 0 or π for a doubly connected ring
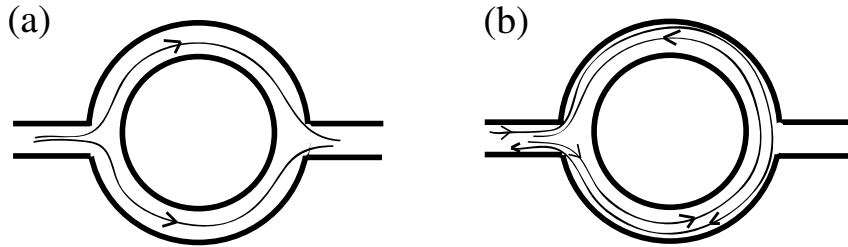

Figure 2.5: The interference of electron paths that lead to h/e oscillations are sketched in Fig. a. The interference of time-reversed waves results in $h/2e$ AAS oscillations (Fig. b). Upon ensemble averaging only the AAS oscillations survive.

(Onsager relation [23]). Hence, the conductance shows h/e periodic AB oscillations. Also higher order interference processes are possible (see Fig. 2.5): waves that travel completely around the ring in opposite directions and then interfere, will give rise to $h/2e$ oscillations (known as Altshuler-Aronov-Spivak (AAS) oscillations [24]). Note that AAS oscillations originate from the interference between time-reversed waves, and hence $\Delta\phi_v \propto \Delta L$ is always equals 0, independent of the path. This makes that the AAS oscillations are not damped out upon ensemble averaging, in contrast to h/e oscillations.

2.7.1 Effect of the spin-dynamics on AB oscillations

The occurrence of AB oscillations does *only* rely on the charge of electrons, *not* on their spin degree of freedom. The spin-dynamics can affect the AB oscillations in an observable way, however, analogous to the (spin-induced) crossover from weak localization to weak anti-localization in 2D systems.

In case of homogeneous Zeeman coupling, i.e., when the spin is a good quantum number, the spin degree of freedom is not expected to affect the periodicity of the AB oscillations (as in the case of weak localization). In case of inhomogeneous magnetic fields, however, or for a ring with Rashba SOI, the spin-dynamics is predicted to induce a spin- and travel-direction dependent phase-shift in the wavefunction. It has been demonstrated that this spin-induced phase shift is equivalent to a spin-dependent "magnetic" flux, just as the AB phase is equivalent to an AB flux [27]. Since the spin-dependent "magnetic" flux adds to the real magnetic flux, the spin-dynamics is expected to cause a deviation from h/e periodicity of the AB oscillations [26, 27].

The spin-induced phase-shift can be written as the sum of two terms $\phi_s = \phi_d + \phi_g$, where ϕ_d is the dynamical phase and ϕ_g the so-called geometrical phase. The dynamical phase depends on the energy of the electron and on time (e.g., uniform Zeeman coupling will cause a spin-induced dynamical phase that equals $\phi_d = \pm \int_0^t dt' E_Z t'/\hbar$). The spin-induced geometrical phase emerges from the basic laws of quantum mechanics, just as the charge-induced (geometrical) AB-phase (eq. 2.32). This geometrical spin phase is known as the geometrical Berry phase [28] (although only the spin-induced phase *difference* or effective flux is well-defined, as in the case of the vector potential).

2.7.2 The geometrical Berry phase

To illustrate the concept of the geometrical Berry phase it is instructive to consider the following example (where the dynamical and geometrical spin-phase can

easily be obtained). Suppose an electron is at rest at the origin, and is subject to a magnetic field whose magnitude is constant but whose direction is changing with time $\mathbf{B}(t) = B_0(\sin\alpha\cos\omega t, \sin\alpha\sin\omega t, \cos\alpha)$ (see Fig. 2.6). The Hamiltonian of this system is then given by

$$\mathbf{H}(t) \;=\; \frac{ge}{2m}\mathbf{B}(t)\cdot\mathbf{S} \;=\; \frac{\hbar\omega_L}{2}\begin{pmatrix} \cos\alpha & e^{-i\omega t}\sin\alpha \\ e^{i\omega t}\sin\alpha & -\cos\alpha \end{pmatrix} \tag{2.34}$$

where $\omega_L = geB_0/2m$ is the Larmor frequency. The eigenspinors $|\Phi_\uparrow(t)\rangle$ and $|\Phi_\downarrow(t)\rangle$ of $H(t)$, with $H(t)|\Phi_{\uparrow,\downarrow}(t)\rangle = \pm\hbar\omega_L/2\,|\Phi_{\uparrow,\downarrow}(t)\rangle$, are given by

$$|\Phi_\uparrow(t)\rangle = \begin{pmatrix} \cos\frac{\alpha}{2} \\ e^{i\omega t}\sin\frac{\alpha}{2} \end{pmatrix} \qquad\qquad |\Phi_\downarrow(t)\rangle = \begin{pmatrix} \sin\frac{\alpha}{2} \\ -e^{i\omega t}\cos\frac{\alpha}{2} \end{pmatrix}$$

These eigenspinors represent the spin-up and spin-down states along the *instantaneous* direction of $\mathbf{B}(t)$, but they do *not* satisfy the time-dependent Schrödinger equation. The true eigenstates of are found from

$$i\hbar\frac{\partial}{\partial t}|\Psi(t)\rangle \;=\; H(t)|\Psi(t)\rangle \tag{2.35}$$

Using the trial wavefunction $|\Psi(t)\rangle$, which is defined as

$$|\Psi(t)\rangle \;=\; \begin{pmatrix} \gamma_1(t)\cos\frac{\alpha}{2} \\ \gamma_2(t)\sin\frac{\alpha}{2} \end{pmatrix} \tag{2.36}$$

we find the following set of coupled differential equations for the time-dependent expansion coefficient $\gamma_1(t)$ and $\gamma_2(t)$:

$$i\,\frac{\partial\gamma_1(t)}{\partial t}\cos\frac{\alpha}{2} \;=\; \frac{\omega_L}{2}\left[\cos\alpha\cos\frac{\alpha}{2}\gamma_1(t) \;+\; \sin\alpha\sin\frac{\alpha}{2}e^{-i\omega t}\gamma_2(t)\right]$$

$$\tag{2.37}$$

$$i\,\frac{\partial\gamma_2(t)}{\partial t}\sin\frac{\alpha}{2} \;=\; \frac{\omega_L}{2}\left[\sin\alpha\cos\frac{\alpha}{2}e^{i\omega t}\gamma_1(t) \;-\; \cos\alpha\sin\frac{\alpha}{2}\gamma_2(t)\right]$$

This set of equations can easily be solved, and gives

$$\gamma_1(t)\,e^{i\omega t/2} \;=\; \cos\frac{\Omega t}{2} \;+\; i\frac{\omega_L+\omega}{\Omega}\sin\frac{\Omega t}{2}$$

$$\tag{2.38}$$

$$\gamma_2(t)\,e^{-i\omega t/2} \;=\; \cos\frac{\Omega t}{2} \;+\; i\frac{\omega_L-\omega}{\Omega}\sin\frac{\Omega t}{2}$$

where we have defined $\Omega = (\omega^2 + \omega_L^2 - 2\omega\,\omega_L \cos\alpha)^{1/2}$. Therefore, the exact time-dependent solution of the Schrödinger equation is explicitly given by

$$|\Psi(t)\rangle = \begin{bmatrix} (\cos\frac{\Omega t}{2} - i\frac{\omega_L + \omega}{\Omega}\sin\frac{\Omega t}{2})\cos\frac{\alpha}{2}\,e^{-i\omega t/2} \\ (\cos\frac{\Omega t}{2} - i\frac{\omega_L - \omega}{\Omega}\sin\frac{\Omega t}{2})\sin\frac{\alpha}{2}\,e^{i\omega t/2} \end{bmatrix} \qquad (2.39)$$

For either $\omega \gg \omega_L$ or $\omega \ll \omega_L$ we can set $(\omega_L + \omega)/\Omega = (\omega_L - \omega)/\Omega = 1$. Within this approximation we then have

$$|\Psi(t)\rangle = \begin{bmatrix} \cos\frac{\alpha}{2}\,e^{-i(\omega+\Omega)t/2} \\ \sin\frac{\alpha}{2}\,e^{i(\omega-\Omega)t/2} \end{bmatrix} \qquad (2.40)$$

and hence, using $(\omega_L + \omega)/\Omega = (\omega_L - \omega)/\Omega = 1$ once more, we find in the adiabatic limit ($\omega \ll \omega_L$) and the strongly non-adiabatic limit ($\omega \gg \omega_L$) the following approximate solutions for the time-dependent Schrödinger equation

$$\omega \gg \omega_L : \qquad |\Psi(t)\rangle = \begin{pmatrix} \cos\frac{\alpha}{2}\,e^{-i\omega t} \\ \sin\frac{\alpha}{2} \end{pmatrix} e^{i\omega_L(\cos\alpha)t/2}$$

$$\omega \ll \omega_L : \qquad |\Psi(t)\rangle = \begin{pmatrix} \cos\frac{\alpha}{2}\,e^{i\omega(\cos\alpha-1)t/2} \\ \sin\frac{\alpha}{2}\,e^{i\omega(\cos\alpha+1)t/2} \end{pmatrix} e^{-i\omega_L t/2}$$

Hence, in the adiabatic limit, the spin-up state after one period of the magnetic field ($t = T = 2\pi/\omega$) is given by

$$|\Psi_\uparrow(T)\rangle = \begin{pmatrix} \cos\frac{\alpha}{2} \\ \sin\frac{\alpha}{2} \end{pmatrix} e^{-i\pi\frac{\omega_L}{\omega}}\,e^{i\pi(\cos\alpha-1)} = \begin{pmatrix} \cos\frac{\alpha}{2} \\ \sin\frac{\alpha}{2} \end{pmatrix} e^{-iE_+T/\hbar}\,e^{i\pi(\cos\alpha-1)} \quad (2.41)$$

This can alternatively be written in the following form

$$|\Psi_\uparrow(T)\rangle = e^{-iE_\uparrow T/\hbar}\,e^{i\pi(\cos\alpha-1)}\,|\Psi_\uparrow(0)\rangle \qquad (2.42)$$

where the first phase, $E_\uparrow T/\hbar$, is the dynamical phase ϕ_d. It depends on the energy of the spin-up state and on the travel time (note that since the transport is adiabatic the spin is the whole time in the instantaneous $E_\uparrow$ state [29]). The second phase, $\pi(\cos\alpha - 1)$, is the geometrical Berry phase ϕ_g, which exclusively depends on the (solid) angle α described by the spin.

Doing the same calculations for the spin-down state we find

$$|\Psi_\downarrow(T)\rangle \;=\; e^{-iE_\downarrow T/\hbar} \, e^{-i\pi(\cos\alpha - 1)} \, |\Psi_\downarrow(0)\rangle \tag{2.43}$$

Hence the geometrical Berry phase is *opposite* for the two spin-directions.

The above discussion gives a specific example where the geometrical Berry phase plays a role. The concept of the Berry phase is by no means however limited to problems involving time-dependent magnetic fields. The Berry phase generally plays a role in systems with a certain time-dependent parameter $\mathbf{R}(t)$, which is described by the Hamiltonian $H(\mathbf{R}(t))$. Assuming the time-evolution of the state of the system to be adiabatic, i.e., it always remains in the nth eigenstate $|n, \mathbf{R}(t)\rangle$, the geometrical Berry phase ϕ_g is generally given by [28]

$$\phi_g \;=\; -\operatorname{Im} \int_{\boldsymbol{R}(0)}^{\boldsymbol{R}(t)} \langle n, \boldsymbol{R} | \, \boldsymbol{\nabla}_{\boldsymbol{R}} \, | n, \boldsymbol{R} \rangle \; d\boldsymbol{R} \tag{2.44}$$

Even if the evolution of the system is non-adiabatic the wavefunction acquires a geometrical phase, as demonstrated by Aharonov and Anandan [30]. The concept of the geometrical phase is therefore very general, and relevant in many situations.

One of this situations is the case of a 1D ring with Rashba SOI. The Rashba field $\boldsymbol{B}_R$ in a 1D ring is pointing in the radial direction, and in the presence of additional Zeeman coupling, the spin makes a solid angle α while travelling around the ring. Fig. 2.6 shows that this case is similar to the case described above. In Chapters 5 and 6 we will discuss the geometrical phases in more detail, as well as the problems to observe it in real solid state samples.
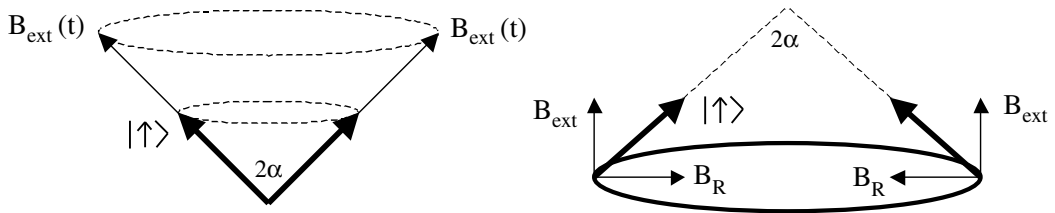

Figure 2.6: Two examples where the spin describes a solid angle. In the left graph the spin $| \uparrow \rangle$ follows (adiabatically) a rotation of the external magnetic field B_{ext} in time. In the right graph the combination of a (time-independent) external field and the internal Rashba field B_R results in a solid angle of the spin as the electron is travelling around the ring.

2.8 Determination of the Rashba coefficient α

So far, we have only discussed the basic characteristics of Rashba SOI and its influence on the spin-dynamics and phase-coherent transport in quantum wells and ring structures. In this Chapter we will outline the microscopic *origin* of Rashba SOI. Also, we will discuss what determines its strength, and why the Rashba strength α is tuneable by applying external gate voltages. This Chapter is largely based on work by Winkler [31] and Lassnig [32]. We refer the reader to these references for more details.

To obtain the strength of the Rashba SOI α theoretically, for a given quantum well, it is necessary to perform bandstructure calculations. A detailed determination of all the energy bands in the crystal for all values of $\boldsymbol{k}$ is in general a very complex and involved task. For semiconductors, however, it is often sufficient to calculate the electron states in the vicinity of the fundamental gap, since the relevant values of $\boldsymbol{k}$ ($k \lesssim k_F$) are usually small. This allows to make simplifying assumptions, and to base the bandstructure calculations on framework of the so-called $\boldsymbol{k} \cdot \boldsymbol{p}$ method, combined with the envelope function approximation (EFA).

2.8.1 The $\boldsymbol{k} \cdot \boldsymbol{p}$ approximation method

Crystalline solids are characterized by a regular pattern of atoms. Hence, electrons moving through such a crystal are subject to a regular potential landscape $V_0(r)$ that has the periodicity of the underlying lattice. The non-relativistic, single-particle Hamiltonian is in this case given by (assuming $\boldsymbol{B} = 0$)

$$\hat{H} = \frac{\mathbf{p}^2}{2m_0} + V_0(r) - \frac{e\hbar}{4m_0{}^2c^2}\boldsymbol{\sigma} \cdot \mathbf{p} \times \boldsymbol{\nabla}V_0(r) \tag{2.45}$$

where m_0 is the free electron mass, and c is the speed of light. The last term is known as the Pauli spin-orbit interaction term, and arises from the electric field $\boldsymbol{\nabla}V_0(r)$ of the atomic cores. Neglect the Pauli SOI term for a moment, and using Bloch functions $e^{i\mathbf{k}\cdot\mathbf{r}}u_{n\mathbf{k}}(r)$ as trial wavefunctions, the Schödinger equation can be written in the following form

$$\left[\frac{\boldsymbol{p}^2}{2m_0} + V_0(r) + \frac{\hbar^2}{2m_0}\mid \boldsymbol{k} \mid^2 + \frac{\hbar}{m_0}\boldsymbol{k} \cdot \boldsymbol{p}\right] u_{n\boldsymbol{k}}(r) = E_{\boldsymbol{k}}^n \, u_{n\boldsymbol{k}}(r) \tag{2.46}$$

where $E_{\boldsymbol{k}}^n$ is the energy of the nth band, and $\boldsymbol{p} = -i\hbar\boldsymbol{\nabla}$. Note that the exponential factor $e^{i\boldsymbol{k}\cdot\mathbf{r}}$ of the Bloch functions is "divided out", which results in the additional

$|\boldsymbol{k}|^2$ and the $\boldsymbol{k} \cdot \boldsymbol{p}$ term in the Hamiltonian. The advantage of this is, that the eigenfunctions $u_{n\boldsymbol{k}}(r)$ of Eq. (2.46) have now the periodicity of the lattice. Hence, Eq. (2.46) needs to be solved for a single primitive cell only, instead of for the whole crystal. Moreover, for small values of $\boldsymbol{k}$ we can neglect the last two terms in Eq. (2.46), and take them into account by perturbation theory. This method is known as the $\boldsymbol{k} \cdot \boldsymbol{p}$ approximation, and is a powerful tool in determining bandstructure properties of semiconductors.

The band-edge energies and corresponding wavefunctions can be obtained by solving Eq. (2.46), and then setting $\boldsymbol{k} = 0$ (note that the $\boldsymbol{k} \cdot \boldsymbol{p}$ term does not vanish in general for $\boldsymbol{k} = 0$, since one first has to take the gradient and then let $k \to 0$). The resulting band-edge functions $u_{n0}(r)$ form a complete and orthonormal set of functions, which is often used as a basis for perturbation theory. If we calculate, for example, the matrix elements of the last two terms of Eq. (2.46) in this basis, $\langle u_{m0}(r) \mid \frac{\hbar^2}{2m_0} \boldsymbol{k}^2 - i \frac{\hbar^2}{m_0} (\boldsymbol{k} \cdot \boldsymbol{\nabla}) \mid u_{n0}(r) \rangle$, we can determine the dispersion relations $E_n(\boldsymbol{k})$, and hence also the effective masses in the conduction and valence bands.

Such a perturbative treatment can also be used to determine the influence of the Pauli SOI term $\frac{e\hbar}{4m_0^2c^2} \boldsymbol{\sigma} \cdot \boldsymbol{p} \times \boldsymbol{\nabla} V_0(r)$ on the energy bands. From these calculations it follows that this Pauli SOI term splits the (p-like) sixfold-degenerate valence band into two subbands with states having total angular momentum $j = 3/2$ and $j = 1/2$, respectively. Specifically, one obtains a heavy-hole band and a light-hole band with $j = 3/2$, and a Pauli split-off band with $j = 1/2$ (see Fig. 2.2). For the s-like conduction band the matrix elements vanish. The Pauli SOI term will only affect the conduction band via higher order processes, i.e., via the $\boldsymbol{k} \cdot \boldsymbol{p}$ coupling to neighboring bands. *This Pauli SOI induced coupling to neighboring bands ultimately results in Rashba SOI in the conduction band.*

2.8.2 The envelope function approximation

The envelope function approximation (EFA) allows one to describe electron (and hole) states in the presence of electric and magnetic fields that vary slowly on the length scale of the lattice constant. For the derivation of Rashba SOI we will be particularly interested in the effect of the confinement potential $V(z)$ of the 2DEG on its energy spectrum.

The full Schödinger equation in the presence of a magnetic field $\boldsymbol{B}$ and a confinement potential $V(z)$ is given by
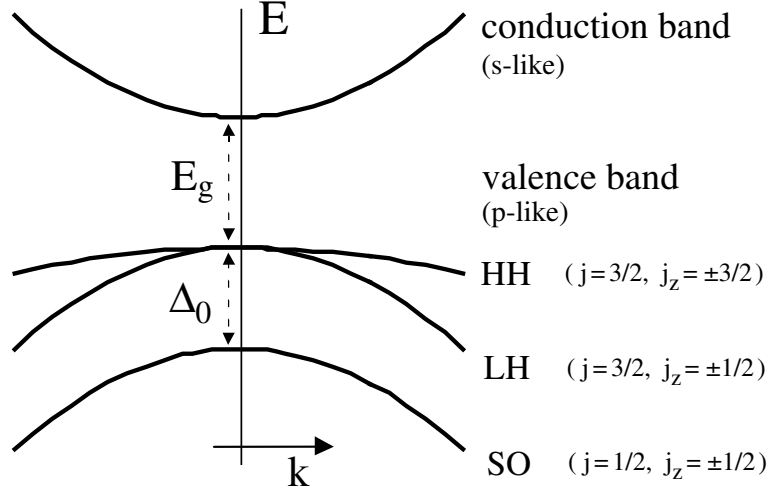
Figure 2.7: The dispersion relation of the valence and conduction bands of a typical semiconductor. Due to the Pauli SOI term, the valance band splits into three different bands; a heavy hole (HH) and light hole (LH) band, both with total angular momentum $j = 3/2$, and a Pauli split-off band with total angular momentum $j = 1/2$. The conduction band is, in first order approximation, not affected by the Pauli SOI term.

$$
\left[\frac{(-i\hbar\boldsymbol{\nabla} + e\boldsymbol{A})^2}{2m_0} \quad + \quad V_0(r) \quad + \quad \frac{\hbar}{4m_0^2 c^2}(-i\hbar\boldsymbol{\nabla} + e\boldsymbol{A}) \cdot \boldsymbol{\sigma} \times (\boldsymbol{\nabla}V_0) \; + \right.
$$

$$
\left. + \; V(z) \; + \; \frac{g_0}{2}\mu_B\boldsymbol{\sigma} \cdot \boldsymbol{B} \right] \Psi(r) \; = \; E \, \Psi(r) \qquad (2.47)
$$

Note that $V(z)$ is neglected in the Pauli SOI interaction term, because it is much smaller than the contribution from the atomic cores ($\nabla V(z) \ll \nabla V_0(r)$). In order to obtain the (approximate) energy spectrum in this case, we treat the last three terms in Eq. (2.47) as perturbations and expand the wavefunction $\Psi(r)$ in terms of the band-edge Bloch functions $u_{n0}(r)$ times a spinor $|\sigma\rangle$.

$$
\Psi(r) \; = \; \sum_{n',\sigma'} \Phi_{n',\sigma'}(r) \, u_{n'0}(r) \, | \, \sigma'\rangle \qquad (2.48)
$$

The position dependent expansion coefficients $\Phi_{n,\sigma}(r)$ modulate the fast oscillating Bloch functions $u_{n0}(r)$, and are therefore called envelope functions. The choice of using the band-edge Bloch functions as a basis is again based on the

fact that the dominant part of the Hamiltonian (the first two terms) is diagonal in this basis; the last three terms will result in (small) off-diagonal elements in the matrix form of the Hamiltonian.

Inserting this trial wavefunction in Eq. (2.47), and multiplying from the left by $\langle \sigma \mid u_{n0}^*(r) \rangle$ and integrating over a unit cell, we obtain the following set of coupled equations (the envelope function are assumed to be constant over the unit cell and can be taken out of the integration).

$$\sum_{n',\sigma'} \Bigg[\left(E_{n'}(0) + \frac{(-i\hbar\boldsymbol{\nabla} + e\boldsymbol{A})^2}{2m_0} + V(z) \right) \delta_{n,n'}\,\delta_{\sigma,\sigma'} \;\; + \;\; \frac{g_0}{2}\mu_B\,\boldsymbol{\sigma}\cdot\boldsymbol{B}\;\delta_{n,n'}$$

$$+ \; \Delta_{\sigma,\sigma'}^{n,n'} \; + \; \tfrac{1}{m_0}(-i\hbar\boldsymbol{\nabla} + e\boldsymbol{A})\cdot P_{\sigma,\sigma'}^{n,n'} \; \Bigg] \; \Phi_{n',\sigma'}(r) \; = \; E\,\Phi_{n,\sigma}(r) \qquad (2.49)$$

The summation runs over all the energy bands n of the crystal, and over the two spin directions σ. The quantities $P_{\sigma,\sigma'}^{n,n'}$ and $\Delta_{\sigma,\sigma'}^{n,n'}$ are defined as follows:

$$P_{\sigma,\sigma'}^{n,n'} \; \equiv \; \langle \sigma \mid \langle u_{n0} \mid \; \boldsymbol{p} \; \mid u_{n'0} \rangle \mid \sigma' \rangle \qquad\qquad\qquad (2.50)$$

$$\Delta_{\sigma,\sigma'}^{n,n'} \; \equiv \; \langle \sigma \mid \langle u_{n0} \mid \; \frac{\hbar}{4m_0^2c^2}\,\boldsymbol{p}\cdot\boldsymbol{\sigma}\times(\boldsymbol{\nabla}V_0) \; \mid u_{n'0} \rangle \mid \sigma' \rangle \qquad (2.51)$$

The left hand side of Eq. (2.49) is called the multiband Hamiltonian, or envelope function Hamiltonian, which contains (implicitly) all the information about all the energy bands in the crystal or quantum well. In order to obtain the energy spectrum explicitly, we have to solve this infinite-dimensional set of coupled differential equations. Obviously, this is generally an impossible task. An approximate solution can be obtained by considering a multiband Hamiltonian that contains only a finite number of bands, or formally stated, to work in a reduced Hilbert space. Specifically, to obtain the energy spectrum of the conduction band, it is often a good approximation to consider only the $\boldsymbol{k}\cdot\boldsymbol{p}$ coupling between the conduction band and neighboring bands. The influence of remote bands on the energy spectrum can be taken into account by perturbation theory, which will lead in general to additional terms in the reduced multiband Hamiltonian. Differently stated, in order to obtain the same energy spectrum in the reduced multiband Hamiltonian and the full infinite-dimensional Hamiltonian, we need to add terms in the reduced Hamiltonian. This way we obtain the *effective* Hamiltonian operator on the reduced Hilbert space. In practice, this effective multiband Hamiltonian can be obtained by quasi-degenerate perturbation theory, also known as "Löwdin partitioning" [33]. Ultimately, this procedure allows to determine the effective Hamiltonian operator for the conduction band only (containing the Rashba SOI term).

2.8.3 The 8×8 Kane model

In order to obtain the effective EFA Hamiltonian for the conduction band in narrow-gap semiconductors, it is enough to consider the $\boldsymbol{k} \cdot \boldsymbol{p}$ coupling between the conduction band and the neighboring valence bands. This is known as the 8×8 Kane model, and the corresponding EFA Hamiltonian reads

$$
\boldsymbol{H}_{8\times 8} = \begin{pmatrix} V_c(z)\,\|_{2\times 2} & \sqrt{3}\,P\,\boldsymbol{T}\cdot\boldsymbol{k} & -\frac{1}{\sqrt{3}}\,P\,\boldsymbol{\sigma}\cdot\boldsymbol{k} \\ \sqrt{3}\,P\,\boldsymbol{T}^{\dagger}\cdot\boldsymbol{k} & (V_v(z)-E_g)\,\|_{4\times 4} & 0 \\ -\frac{1}{\sqrt{3}}\,P\,\boldsymbol{\sigma}\cdot\boldsymbol{k} & 0 & (V_\Delta(z)-E_g-\Delta_0)\,\|_{2\times 2} \end{pmatrix}
$$

with $\hbar\boldsymbol{k} = -i\hbar\boldsymbol{\nabla}+e\boldsymbol{A}$, E_g and Δ_0 are the fundamental energy gap and the Pauli SOI gap, respectively (see Fig. 2.7), and P is the Kane's momentum matrix element [34]. The matrices $\boldsymbol{T}$ are defined in Ref. [35]. $V_{c,v}(z)$ includes the position dependence of the band edges. This z-dependence is absent, of course, in bulk semiconductors, but is generally present when we confine the electrons to two dimensions, i.e., in quantum wells (see Fig. 2.8).

From this 8×8 Kane Hamiltonian it is possible to construct the effective 2×2 conduction band Hamiltonian (for the two spin directions). This EFA Hamiltonian for the conduction band is (assuming $V_{v,c}(z), E_F \ll E_g$) [31, 36]

$$
\hat{H}_c^{3D} = \frac{\hbar^2 \boldsymbol{k}^2}{2m^*} + V_c(z) + g^*\mu_B\,\boldsymbol{\sigma}\cdot\boldsymbol{B} + \kappa\,\boldsymbol{\sigma}\cdot\boldsymbol{k}\times\boldsymbol{\nabla}(V_v(z)+V_\Delta(z)) \quad (2.52)
$$

The first term is the kinetic energy, $V_c(z)$ is the position-dependent band edge energy (see Fig. 2.8), the third term is the effective Zeeman energy, and the last term is the Rashba SOI. Note that it follows from Eq. (2.52) that the Rashba term depends on the potential gradient *in the valence band*. The quantities m^*, g^* and κ are given by the following expressions:

$$
\frac{m_0}{m^*} \approx \frac{2P^2}{3m_0}\left[\frac{2}{E_g}+\frac{1}{E_g+\Delta_0}\right] \quad (2.53)
$$

$$
\frac{g^*}{2} \approx -\frac{2P^2}{3m_0}\left[\frac{1}{E_g}-\frac{1}{E_g+\Delta_0}\right] \quad (2.54)
$$

$$
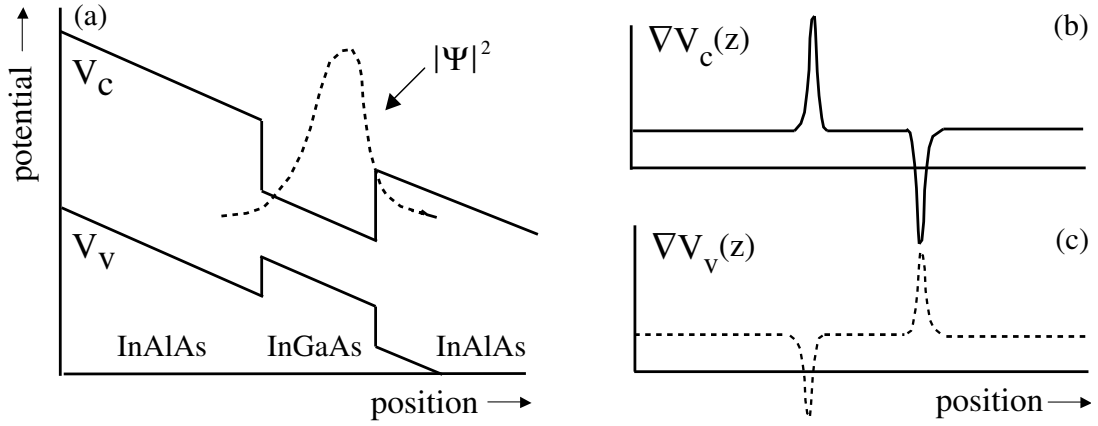\kappa \approx -\frac{P^2}{3}\left[\frac{1}{E_g^2}-\frac{1}{(E_g+\Delta_0)^2}\right] \quad (2.55)
$$

Figure 2.8: A sketch of the typical potential profile of the conduction and valence band of an asymmetrically doped InAlAs/InGaAs/InAlAs quantum well [40]. The electronic wavefunction in the confinement direction (or density $|\Psi|^2$) is indicated by the dashed curve. Figs. (b) and (c) show the corresponding (position-dependent) electric fields in the conduction and valence band, respectively. Note that the electric fields at a quantum well interface is *opposite* for the two bands.

Note that κ vanishes in the limit of vanishing Pauli SOI ($\Delta_0 \to 0$). Hence, *the atomic electric field felt by the* Bloch *functions is a crucial prerequisite for having Rashba SOI in the conduction band, in addition to having a non-vanishing expectation value of* $\nabla(V_v(z) + V_\Delta(z))$, *felt by the* envelope *function.* Notice also that the effective g-factor and the Rashba prefactor κ become larger for narrow-gap materials, i.e., for small values of E_g. *This makes the Rashba SOI generally particular important in narrow-gap materials,* such as InAs and InGaAs ($\kappa = 117.1$ $e\mathring{A}^2$ for InAs, versus 5.2 $e\mathring{A}^2$ for GaAs, for example [31]).

2.8.4 Rashba SOI strength in a quantum well

The last step is to calculate the effective 2×2 Hamiltonian for electrons in a quantum well (i.e., H_c^{2D}). Therefore we impose that the confining potential $V_c(z)$ (or band bending) is large, which is achieved by sandwiching a narrow-gap semiconductor between two large-gap semiconductors (see Fig. 2.8(a)). More accurately stated, $V_c(z)$ is the self-consistent confinement potential, which also includes depletion and the Hartree contribution [32].

In a thin quantum well, the confinement energy in the z-direction is the dominant energy scale, and therefore we can obtain the wavefunctions and (2D)

subband energies by neglecting the Zeeman and Rashba SOI term, in first order approximation. Since the Hamiltonian is translational invariant in the plane of the quantum well, the eigenfunctions can be written as $\Psi_n(r) = e^{i(k_x x + k_y y)} \Phi_n(z)$, and $\Phi_n(z)$ is obtained from

$$\left[-\frac{d}{dz} \left(\frac{\hbar^2}{2m^*(z)} \right) \frac{d}{dz} + V_c(z) \right] \Phi_n(z) = E_n \Phi_n(z) \tag{2.56}$$

If the quantum well is thin enough, i.e., when $E_1 - E_0 \gg \hbar^2 k_F^2 / 2m^*$, all the electrons are in the lowest subband E_0, with wavefunction $\Phi_0(z)$. The effective 2D Hamiltonian operator for electrons in the quantum well is then given by $\hat{H}_c^{2D} = \langle \Phi_0(z) \mid \hat{H}_c^{3D} \mid \Phi_0(z) \rangle$, or explicitly

$$\hat{H}_c^{2D} = \frac{p_x^2 + p_y^2}{2m^*} + E_0 + g^* \mu_B \boldsymbol{\sigma} \cdot \boldsymbol{B} + \alpha \left(\sigma_x p_y - \sigma_y p_x \right) \tag{2.57}$$

where the Rashba SOI strength α given by the following expression:

$$\alpha = \langle \Phi_0(z) \mid \kappa \frac{d}{dz} [V_v(z) + V_\Delta(z)] \mid \Phi_0(z) \rangle \tag{2.58}$$

Note that in the derivation of this expression for α it was assumed that $V_{v,c}(z), E_F \ll E_g$, which allowed to treat κ as a z-independent constant. Without these simplifying assumption, the more accurate expression for α becomes [32]

$$\alpha = \langle \Phi_0(z) \mid \frac{d}{dz} \left[\frac{1}{E_F - V_v(z) - E_g} - \frac{1}{E_F - V_\Delta(z) - \Delta_0} \right] \mid \Phi_0(z) \rangle \tag{2.59}$$

which reduces to Eq. (2.58) for $V_{v,c}(z), E_F \ll E_g$. Note that *the average electric field that is acting on the conduction electrons vanishes*, i.e., $\langle \Phi_0(z) \mid \nabla V_c(z) \mid \Phi_0(z) \rangle = 0$, consistent with Ehrenfest's theorem (which states that on average there is no force acting on a bound state [37]). This theorem does not imply, however, that the value of α should also vanish, because in Eq. (2.48) we evaluate the expectation value of the electric field in the valence band *with the wavefunction of the conductance band* (i.e., Ehrenfest's theorem does not apply). In fact, because the sign of the electric field at the quantum well interfaces is *opposite* for the valence and the conduction band (see Fig 2.8 (b) and (c)), this expectation value and hence α, does not vanish (especially when the wavefunction $\Phi_0(z)$ has a different amplitude in the left- and right quantum well interface [38]). Only

when the (self-consistent) confinement potential has inversion symmetry, i.e when $V_{v,\Delta}(z) = V_{v,\Delta}(-z)$, the Rashba SOI vanishes ($\alpha = 0$).

From Eqs. (2.58) and (2.59) it also becomes obvious why the Rashba SOI strength can be controlled by applying a gate voltage: A gate voltage will affect the shape of the electron confinement potential, i.e., it will affect the z-dependence of the conduction and valence band $V_{c,v,\Delta}(z)$. These induced changes in $V_{c,v,\Delta}(z)$ do affect the expectation values for the Rashba SOI strength α (see Eqs. (2.58) or (2.59)). This has also been demonstrated experimentally [38, 39].

Apart from applying a gate voltage, the band structure of the conductance and valence band can also be affected by the position of the carrier supply layer(s) in the heterostructure (see Chapter 3 for details). This possibility has been demonstrated experimentally in Ref. [40], and has also been exploited in this Thesis.

References

[1] Y.A. Bychkov and E.I. Rashba, J. Phys. C **17**, 6093 (1984)

[2] For Rashba we have $\hat{H}_R(\mathbf{p}, \boldsymbol{\sigma}) = \hat{H}_R(-\mathbf{p}, -\boldsymbol{\sigma})$. In contrast, for Zeeman coupling we have $\hat{H}_Z(\mathbf{p}, \boldsymbol{\sigma}) \neq \hat{H}_Z(-\mathbf{p}, -\boldsymbol{\sigma})$.

[3] M.I. Dyakonov and V.I. Perel, Sov. Phys. JETP **33**, 1053 (1971); Sov. Phys. Solid State **13**, 3023 (1972)

[4] M.I. Dyakonov and V.Y. Kachorovskii, Sov. Phys. Semicond. **20**, 110 (1986)

[5] A. A. Burkov and L. Balents Phys. Rev. B **69**, 245312 (2004)

[6] M.M. Glazov, Phys. Rev. B **70**, 195314 (2004)

[7] A.A. Kiselev and K.W. Kim, Phys. Rev. B **61**, 13115 (2000); A.A. Kiselev and K.W. Kim, Phys. Stat. Sol. B **221**, 491 (2000)

[8] Y. Yafet, Phys. Rev. **85**, 478 (1952); R.J. Elliot, Phys. Rev. **96**, 266 (1954)

[9] see, e.g., G.E. Pikus and A.N. Titkov, "Optical Orientation", edited by F. Meier and B.P. Zakharchenya (Amsterdam, 1984)

[10] V.A. Froltsov, Phys. Rev. B **64**, 45311 (2001)

[11] G. Bergmann, Physics Reports **107**, 1 (1984);

[12] S. Chakravarty and A. Schmid, Physics Reports **140**, 193 (1986)

[13] This is justified when λ_F is much smaller than the mean free path, and the interference of time-reversed path does hardly affect the electron motion.

[14] H. Mathur and H.U. Baranger, Phys. Rev. B **64**, 235325 (2001);

[15] J.S. Meyer, A. Altland, and B.L. Altshuler, Phys. Rev. Lett. **89**, 206601 (2002); V.I. Fal'ko and T. Jungwirth, Phys. Rev. B **65**, R81306 (2002)

[16] G. Bergmann, Phys. Rev. Lett. **48**, 1046 (1982)

[17] S. Hikami, A.I. Larkin, and Y. Nagaoka, Prog. Theor. Phys. **63**, 707 (1980)

[18] S.V. Iordanskii, Y.B. Lyanda-Geller, and G.E. Pikus, JETP Lett. **60**, 206 (1994) (Pis'ma Zh. Eksp. Teor. Fiz. **60**, 199 (1994))

[19] Y. Lyanda-Geller, Phys. Rev. Lett. **80**, 4273 (1998)

[20] S. Maekawa and H. Fukuyama, J. Phys. Soc. Jpn. **50**, 2516 (1981)

[21] A.G. Malshukov, K.A. Chao, and M. Willander, Phys. Rev. B **56**, 6436 (1997); A.G. Malshukov, V.A. Froltsov, and K.A. Chao, Phys. Rev. B **59**, 5702 (1999)

[22] Y. Aharonov and D. Bohm, Phys. Rev. **115**, 485 (1959)

[23] L. Onsager, Phys. Rev. **38**, 2265 (1931)

[24] B.L Altshuler, A.G. Aronov, and B.Z. Spivak, JETP Lett. **33**, 94 (1981)

[25] Y. Meir, Y. Gefen, and O. Entin-Wohlman, Phys. Rev. Lett. **63**, 798 (1989); O. Entin-Wohlman, Yuval Gefen, Yigal Meir, and Y. Oreg, Phys. Rev. B **45**, 11890 (1992)

[26] D. Loss, P. Golddbart, and A.V. Balatsky, Phys. Rev. Lett. **65**, 1655 (1990); D. Loss and P.M. Goldbart, Phys. Rev. B **45**, 13544 (1992); A. Stern, Phys. Rev. Lett. **68**, 1022 (1992); H. Mathur and A.D. Stone, Phys. Rev. Lett. **68**, 2964 (1992); Y. Yi, T. Qian and Z. Su, Phys. Rev. B **55**, 10631 (1997)

[27] Y. Meir, Y. Gefen, and O. Entin-Wohlman, Phys. Rev. Lett. **63**, 798 (1989); O. Entin-Wohlman, Yuval Gefen, Yigal Meir, and Y. Oreg, Phys. Rev. B **45**, 11890 (1992)

[28] M.V. Berry, Proc. R. Soc. London A **392**, 45 (1984)

[29] The exact transition probability to the instantaneous spin-down direction is

$$|\langle \Psi_\uparrow(t)|\Phi_\downarrow(t)\rangle|^2 = \left[\frac{\omega}{\Omega} \sin\alpha \sin\frac{\Omega t}{2} \right]^2$$

In the adiabatic limit we have $\omega \ll \Omega$, and therefore the transition probability goes to zero, i.e., the initial spin-up state keeps pointing along $\boldsymbol{B}$.

[30] Y. Aharonov and J. Anandan, Phys. Rev. Lett. **58**, 1593 (1987)

[31] R. Winkler, *Spin-Orbit Coupling Effects in Two-Dimenional Electron and Hole Systems* (Springer-Verlag, Berlin, 2003)

[32] R. Lassnig, Phys. Rev. B **31**, 8076 (1985)

[33] P.O. Löwdin, J. Chem. Phys. **19**, 1396 (1951); J.M. Luttinger and W. Kohn, Phys. Rev. **97**, 869 (1955); See also Ref. [31].

[34] E.O. Kane, J. Phys. Chem. Solids **1**, 249 (1957)

[35] H.R. Trebin, U. Rössler, and R. Ranvaud, Phys. Rev. B **20**, 686 (1979); or see p. 65 of [31].

[36] F.J. Ohkawa and Y. Uemura, J. Phys. Soc. Jpn **37**, 1325 (1974); T. Darnhofer and U. Rössler, Phys. Rev. B **47**, 16020 (1993); See also Ref. [31].

[37] J.J. Sakurai, Modern Quantum Mechanics, revised edition, Addison-Wesley, Redwood City, 1994.

[38] G. Engles, J. Lange, T. Schäpers, and H. Lüth, Phys. Rev. B **55**, R1958 (1997); T. Schäpers, G. Engels, J. Lange, T. Klocke, M. Hollfelder, H. Lüth, J. Appl. Phys. **83**, 4324 (1998); P. Pfeffer and W. Zawadzki, Phys. Rev. B **59**, R5312 (1999)

[39] J. Nitta, T. Akazaki, H. Takayanagi, and T. Enoki, Phys. Rev. Lett. **78**, 1335 (1997); D. Grundler, Phys. Rev. Lett. **84** 6074 (2000);

[40] T. Koga, J. Nitta, T. Akazaki, and H. Takayanagi, Phys. Rev. Lett. **89**, 46801 (2002)

Chapter 3

Materials and device fabrication

3.1   Introduction

In semiconductor heterostructures, bandgap engineering makes it possible to trap electrons in a very narrow potential well. The motion in the growth direction is then quantized, and the electrons form a 2D electron gas (2DEG). 2DEGs are attractive as compared to metallic structures, because the mobility of the carriers is very high. Moreover, many relevant parameters can be controlled by applying a gate voltage, such as the electron density, the elastic scattering rate, as well as the Rashba SOI strength (see also below). These properties make it possible to study systematically the effects of Rashba SOI on quasi-ballistic (and phase-coherent) transport, in different kind of structures.

In this Thesis we discuss (1) the effect of Rashba SOI on Aharonov-Bohm conductance oscillations measured in a ring structure, and (2) the effect of the competition between Rashba SOI and Zeeman coupling on phase-coherent transport in 2D systems (Hall bars), in particular its effect on the spin relaxation time and on the dephasing of electronic waves.

For the fabrication of these two kinds of samples, i.e., the ring structure and the Hall bars, we have used two different kinds of heterostructures (with different Rashba SOI strengths). The heterostructure growth, as well as the device fabrication, has been performed in the NTT Basic Research Laboratories, Atsugi, Japan, in the group of prof. dr. J. Nitta. Below we briefly describe the characteristics of the different heterostructures. In Section 3.3 the sample fabrication procedure is described, and finally, in Section 3.4 the measurement setup is briefly outlined.

3.2   Heterostructures

The first kind of heterostructure that has been used in this Thesis is an InAs-inserted $In_{0.53}Ga_{0.47}As/In_{0.52}Al_{0.48}As$ heterostructure, which was grown by molecular beam epitaxy (MBE) on a Fe-doped semi-insulating (100) InP substrate. The whole layer structure of this wafer is sketched in Fig. 3.1. All InGaAs and InAlAl layers were lattice matched to InP. The 2DEG channel is formed in the undoped InAs layer (only the lowest subband is occupied by electrons due to the small layer thickness). The carriers are provided by the doped InAlAs layer, which has a doping density of $N = 4 \times 10^{18}$ cm^{-3} (the doping layer controls the position of the Fermi level in the 2DEG; when it is above the bottom of the conduction band edge of the 2DEG, mobile carriers are induced in the 2DEG). An undoped In-AlAs layer is separating the 2DEG channel from the doping layer, which reduces scattering from ionized impurities in the doping layer, and hence enhances the

```
┌─────────────────────────────────────────┐
│   InAlAs gate Schottky layer  (20 nm)    │
├─────────────────────────────────────────┤
│        InGaAs  layer  (13.5 nm)          │
├─────────────────────────────────────────┤
│      InAs  quantum well  (4 nm)          │
├─────────────────────────────────────────┤
│       InGaAs  layer  (2.5 nm)            │
├─────────────────────────────────────────┤
│      InAlAs  spacer layer  (6nm)         │
├─────────────────────────────────────────┤
│  doped  InAlAs  carrier-supply layer (7nm)│
├─────────────────────────────────────────┤
│         InAlAs  buffer layer             │
├─────────────────────────────────────────┤
│                                          │
│     semi-insulating  InP  substrate      │
│                                          │
└─────────────────────────────────────────┘
```

Figure 3.1: Schematic overview of the layer structure of the first kind of heterostructure that has been used in this Thesis (Chapter 6). The doping density in the carrier supply layer is $N = 4 \times 10^{18} \text{cm}^{-3}$.

electron mobility μ of the electrons in the 2DEG (μ is typically 50.000 cm^2/Vs). Note that the carrier supply layer is underneath the 2DEG channel. The structure is therefore called an "inverted" heterostructure. The advantage of inverted heterostructures is that they generally have a lower gate leakage current and a higher breakdown voltage when a voltage is applied to a top-gate electrode, as compared to a normal type heterostructure.

Figure 3.2 shows the conduction band profile and the electron density distribution of the heterostructure drawn in Fig. 3.1, for three different electron densities ($n_e = 1, 2, 3 \cdot 10^{12}$ cm^{-2}). As is apparent from Fig. 3.2, the conduction band edge depends on the position along the growth direction, and has no inversion symmetry. The same holds true for the valence band (not shown). For all densities, the electrons are mainly positioned in the narrow InAs layer. The electrons in this layer are confined by an (inversion) asymmetric confinement potential, caused by the asymmetry in the layer structure, in particular the asymmetry in the doping with respect to the InAs conduction layer. Notice that the asymmetry in confinement potential depends on the precise electron density.

In the previous Chapter it was shown that the Rashba strength in the quantum well depends on the asymmetry of the confinement potential, and hence from Fig. 3.2 it follows that the Rashba strength depends on the electron density. Since the electron density can be modified by applying a gate voltage, so can the Rashba strength. Note that gate voltage will also modify the slope in the con-
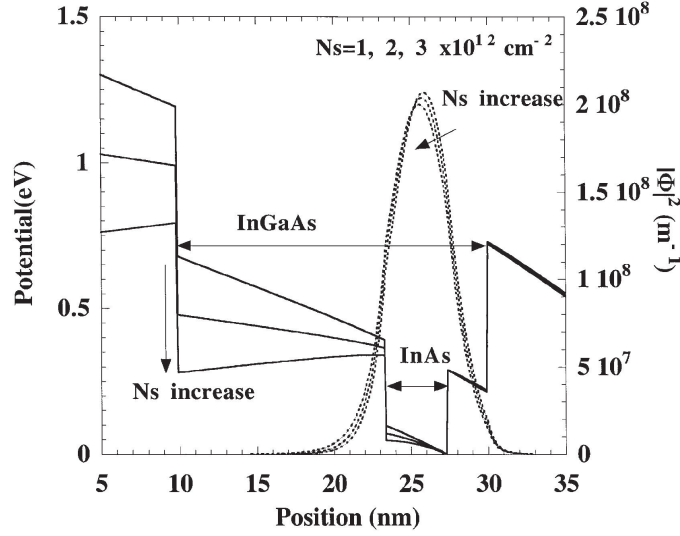
Figure 3.2: The calculated conduction band diagram of the first kind of heterostructure, for three different electron densities (solid lines). The electron density distribution $|\Phi|^2$ for the three different densities is indicated by the dashed lines. The Figure is taken from Ref. [2].

duction band, and hence results in an additional change in the Rashba strength [1]. The Rashba SOI strength in this wafer is estimated (from the analysis of the Shubnikov-de Haas oscillations) to be $\alpha \approx 1 \cdot 10^{-11}$ eVm for $n_e = 1.75 \cdot 10^{12}$ cm^{-2}, and $\alpha \approx 0.65 \cdot 10^{-11}$ eVm for $n_e = 2.5 \cdot 10^{12}$ cm^{-2} (for more details see Ref. [2]).

The second kind of heterostructure is schematically depicted in Fig. 3.3. It is an In$_{0.52}$Al$_{0.48}$As/In$_{0.53}$Ga$_{0.47}$As/In$_{0.52}$Al$_{0.48}$As based heterostructure that is grown by metal-organic chemical vapor deposition (MOCVD) on a Fe-doped semi-insulating InP substrate. All the layers are again lattice matched to InP, and the 2DEG is now formed in the 10 nm wide InGaAs layer (only the lowest subband is occupied by electrons). The interesting feature of this heterostructure is that two separate doping layers have been introduced, one on either side of the 2DEG. We denote the doping levels of the top and bottom carrier supply layer as N_2 and N_1, respectively. By varying the ratio N_2/N_1, while keeping $N_1 + N_2$ constant, the degree of structural inversion asymmetry of the quantum well can be controlled (see Fig. 3.4), i.e., this way the Rashba strength can be controlled by doping means. Four different heterostructures have been grown, where $N_1 + N_2$ was kept fixed to 4×10^{18} cm^{-3}, and the ratio N_2/N_1 was chosen to be 0, $\frac{1}{3}$, 1 and 3, respectively.

| InAlAs gate Schottky layer (20 nm) |
| doped InAlAs carrier-supply layer (7nm) |
| InAlAs spacer layer (6nm) |
| InGaAs quantum well (10 nm) |
| InAlAs spacer layer (6nm) |
| doped InAlAs carrier-supply layer (7nm) |
| InAlAs buffer layer |
| semi-insulating InP substrate |

Figure 3.3: Schematic overview the the layer structure of the second kind of heterostructures that have been used in this Thesis (Chapters 7 and 8).

Figure 3.4 shows the results of the self-consistent Poisson-Schrödinger calculation for the four different wafers (the potentials are plotted relative to the Fermi energy) [3]. The electron density was fixed to $n_e = 7 \cdot 10^{11}$ cm^{-2}. For the heterostructure with the largest asymmetry in the doping ($N_2/N_1 = 0$), the slope in the potential is also largest. For more symmetrically doped heterostructures the confinement potential of the electrons in the InGaAs layer becomes more symmetric. Hence, the Rashba strength can be controlled by controlling the doping ratio N_2/N_1. For $N_2/N_1 = 0$, $1/3$, and 1 the Rashba spin-split energy $\Delta = 2\alpha k_F$ is estimated to be $\Delta \approx 1.8$, 1.4, and 0.5 meV, respectively, from the analysis of the magnetoconductance (see Fig. 3.10) [3, 6].

3.3 Device fabrication

In this Thesis we describe systematically the phase-coherent transport properties of two types of samples: ring structures and Hall bars. The fabrication procedure of these two structures is briefly outlined below.

3.3.1 Fabrication & characterization of the ring structure

The ring structure has been fabricated by electron beam lithography (EBL), in combination with electron cyclotron resonance dry etching (ECR). The advan-
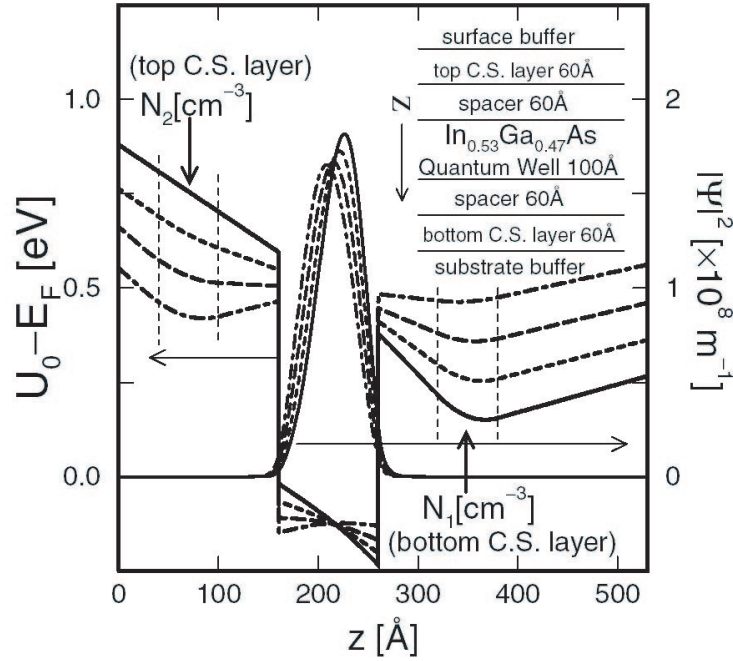
Figure 3.4: The calculated self-consistent band structure of the four different heterostructures of the second kind. The electron sheet density is $n_s = 7 \cdot 10^{12}$ cm^{-2}. The solid, short-dashed, long-dashed, and dash-dotted curves denote the bandstructure for $N_2/N_1 = 0$, $\frac{1}{3}$, 1, and 3, respectively. The inset shows again schematically the layer structure, where "C.S. layer" stands for the carrier supply layer. The figure is taken from Ref. [3].

tage of ECR etching in comparison to wet etchant methods is that ECR etching is isotropic for all crystal orientations, and hence side etching is reduced in this process. The fabrication procedure for defining a ring structure in the heterostructure is schematically depicted in Fig. 3.5. First, a layer of (positive) organic resist (poly-methyl-methacrylate, PMMA) is spun on top of the heterostructure. Then, the ring structure is defined by electron beam writing in the electron-sensitive resist. The exposed parts of the resist are subsequently removed by a developer (solution of methyl isobutyl ketone, MIBK, and iso-propyl alcohol, IPA). In the next step the part of the heterostructure that is not covered by the resist is removed by ECR dry etching. Note that the etching should be deep enough to remove the 2DEG layer (indicated by the dashed line), as well as the doping layer (not shown). The last step is to remove the layer of PMMA-resist with acetone.

Subsequently, the ring is covered by an Au/Ti gate electrode. This procedure is schematically depicted on the right-hand side of Fig. 3.5. Again, a PMMA
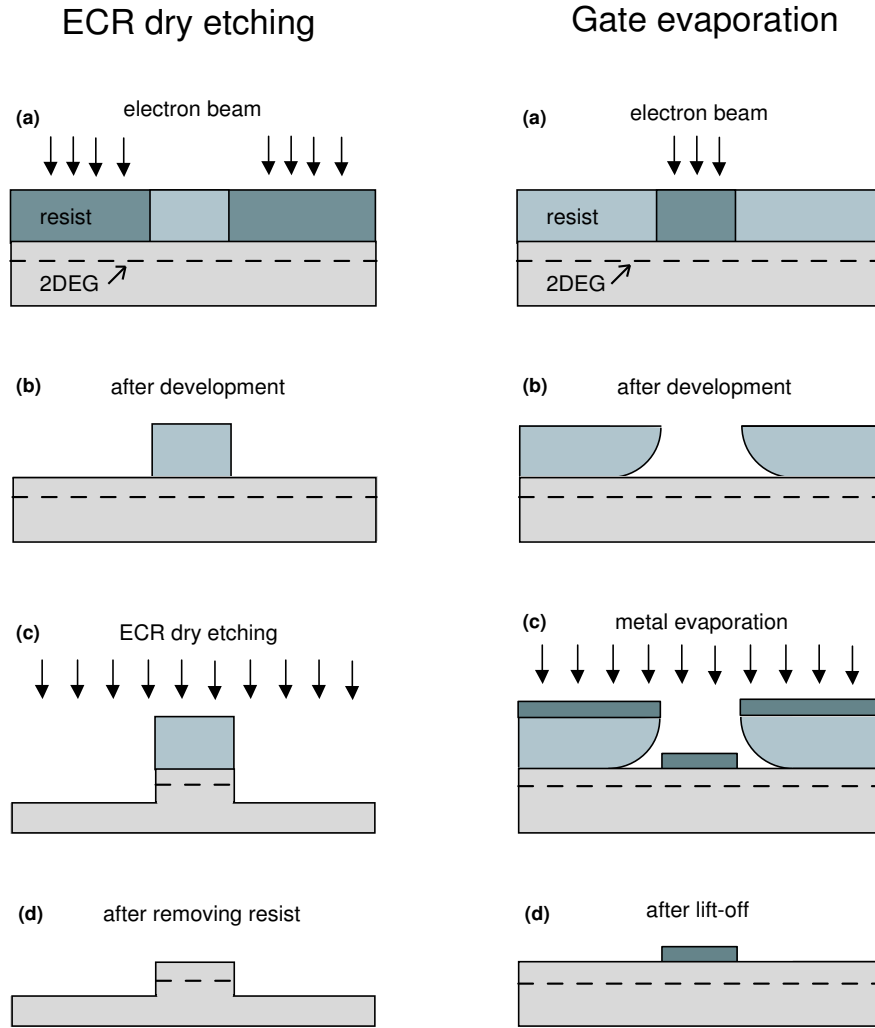
Figure 3.5: Schematic overview of the fabrication procedure for (dry) etching a ring structure (left column), and evaporating a metallic gate electrode (right column).

layer is spun onto the heterostructure, and the exposed parts of the resist are removed by the developer. In the next step a thin layer of Titanium ($\approx 5\,\mathrm{nm}$) is evaporated, followed by a thicker Gold layer ($\approx 100\,\mathrm{nm}$). The Titanium layer acts as an adhesion layer. In the last step the remaining resist is removed by acetone, and hence the metal film on top of the resist is removed as well. This is the so-called "lift-off" process, which is made possible by the undercut in the PMMA resist (caused by the significant electron scattering at the heterostructure toplayer during the electron beam exposure). In order to measure transport properties of the ring, Ohmic contacts are connected to the 2DEG by evaporating AuGeNi contacts, and subsequently annealing them.

Figure 3.6 shows a SEM picture of one of the resulting ring structures. The mean radius and width of the arms of the ring are approximately 350 nm and 180 nm, respectively. A metallic gate is covering the whole ring, allowing to change the electron density n_e. At $V_g = 0$V the electron density n_e was estimated to be $1.75 \cdot 10^{12}$ cm^{-2} (from Shubnikov-de Haas measurements in the bulk 2DEG), and changes about linearly with gate voltage V_g, following the relation $dn_e/dV_g \approx 1.7 \cdot 10^{12}$ cm^{-2}/V. The mean free path and the mobility are estimated to be about $0.8\,\mu$m and 48.000 cm^2/Vs, respectively (at $V_g = 0$ V). Hence, transport in the ring is quasi-ballistic [4].
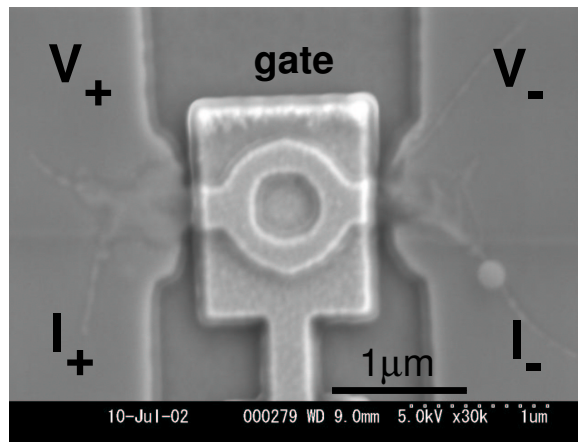
Figure 3.6: SEM picture of the fabricated ring structure. A gate electrode is covering the whole ring, allowing to change the electron density (and Rashba strength). The voltage and current contacts are indicated with $V_\pm$ and $I_\pm$, respectively.

The left-hand side of Fig. 3.7 shows a typical magnetoresistance trace of the ring (the magnetic field is applied perpendicular to the heterostructure). The resistance shows clear Aharonov-Bohm oscillations, superimposed on a randomly fluctuating background. The presence of Aharonov-Bohm oscillations shows that transport through the ring (measured at $T = 0.3$ K) is phase-coherent (τ_ϕ is typically between 2 and 10 μm, depending on the electron density). The right-hand side of Fig. 3.7 shows the Fourier transform of the measured magnetoconductance. The h/e, $h/2e$, and $h/3e$ (see inset) peaks are clearly visible in the Fourier transform. The center frequency of the h/e peak in the Fourier transform corresponds to the mean radius of the ring. The finite width of h/e peak and its irregular shape are caused by (sample specific) elastic scattering in the ring and the finite width of the arms of the ring (there are typically $7 - 15$ conducting modes in the radial direction, depending on the applied gate voltage).

In Chapter 6 we describe the statistical properties of the measured AB os-

cillations, and demonstrate in detail how sample specific features in the Fourier transform can be suppressed, in order to identify (Rashba-induced) spin effects in the Fourier transform of the measured AB oscillations.
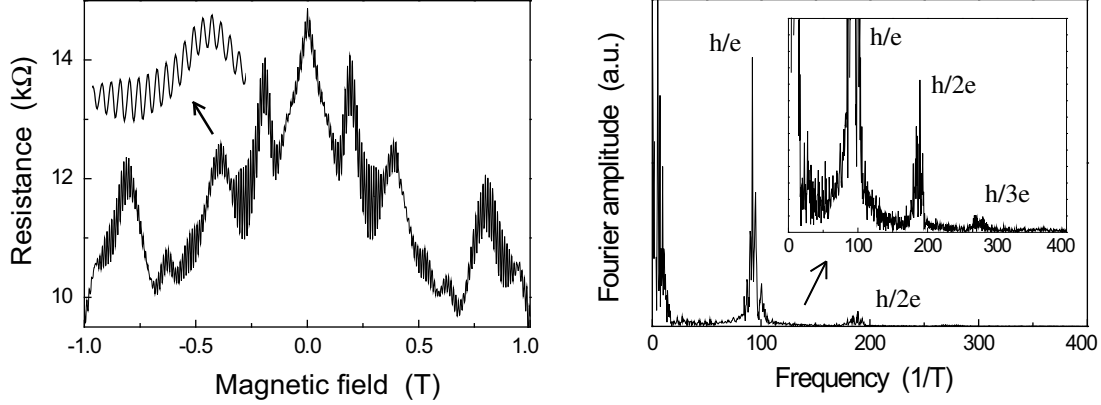

Figure 3.7: *Left:* a typical magnetoresistance measurement at $T = 0.3\,$K, showing Aharonov-Bohm (AB) oscillations, superimposed on aperiodic conductance fluctuations. *Right:* the Fourier transform of the magnetoconductance. The h/e, $h/2e$, and $h/3e$ (see inset) peaks are clearly visible in the Fourier spectrum.

3.3.2 Fabrication & characterization of the Hall bars

In Chapters 7 and 8 we study the effect of the interplay between Rashba SOI and Zeeman coupling on the spin dynamics and on phase-coherent transport. For these experiments we have fabricated Hall bar structures out of the second kind of heterostructures (Fig. 3.3). Specifically, we have studied in detail the wafers with $N_2/N_1 = 0$, $\frac{1}{3}$, and 1, each having a different Rashba SOI strength.

The Hall bars have been fabricated using standard photo-lithography and ECR dry etching. Note that in this case the pattern does not need to be written by electron beam lithography, because all the relevant dimensions are relatively large ($\gg 1\,\mu$m). The fabrication procedure of the Hall bars (using photo-masks) is essentially the same as depicted in Fig. 3.5; only the electron beam is replaced by UV light. Subsequently, the Hall bar is covered by a 100 nm thick SiO_2 layer to provide good electrical insulation to the gate electrode. The gate electrode is fabricated using photo-lithography and lift-off techniques (see Fig. 3.5), and consists again of a thin Ti-layer and a 150nm thick Au-layer. Ohmic contacts are again obtained by evaporating AuGeNi and annealing.
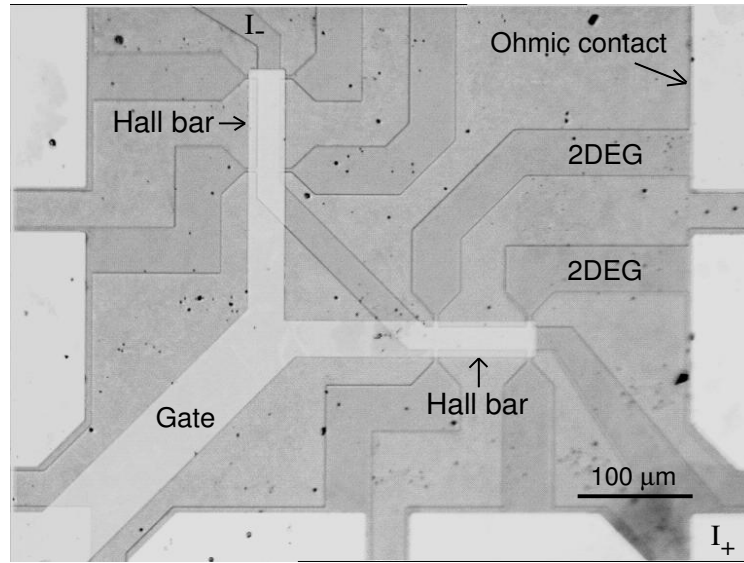
Figure 3.8: An optical picture of a fabricated sample, which consists of two Hall bars that are covered by a gate electrode (allowing to change the electron density, the elastic scattering time, and the Rashba SOI strength).

Figure 3.8 shows an optical picture of the resulting structure. Note that each sample consists of two $20 \times 80\,\mu$m Hall bars, which are aligned perpendicular to each other. This sample design allows to measure the electrical response of two different situations simultaneously. For example, when a magnetic field B is applied in the plane of the 2DEG, the electrical response with $B \perp I$ and $B \parallel I$ can be measured simultaneously. As far as phase-coherent transport is concerned, we did not find a significant difference between these two situations, however.

Figure 3.9 shows typical magnetoconductance traces, measured in the Hall bar with the weakest Rashba SOI strength (left), and the Hall bar with the strongest Rashba strength (right). The applied magnetic field is pointing perpendicular to the 2DEG. In both cases a weak anti-localization (WAL) peak is visible around $B = 0\,$T. This is an experimental signature for the presence of SOI. The size of the WAL peak gives an indication of the strength of the SOI in the sample: if the SOI strength is large, the WAL peak will also be large. The precise strength of the Rashba SOI can be determined experimentally by fitting the measured line-shape of the magnetoconductance with the theory of Iordanskii, Lyanda-Geller, and Pikus[5]. This fitting procedure simultaneously allows to determine the phase-coherence time (we find that τ_ϕ is typically $15 - 80\,$ps, depending on the wafer and electron density [6]). The effective mass was determined to be $m^* = 0.041\,m_0$ from the temperature dependence of the Shubnikov-de Haas oscillation amplitude
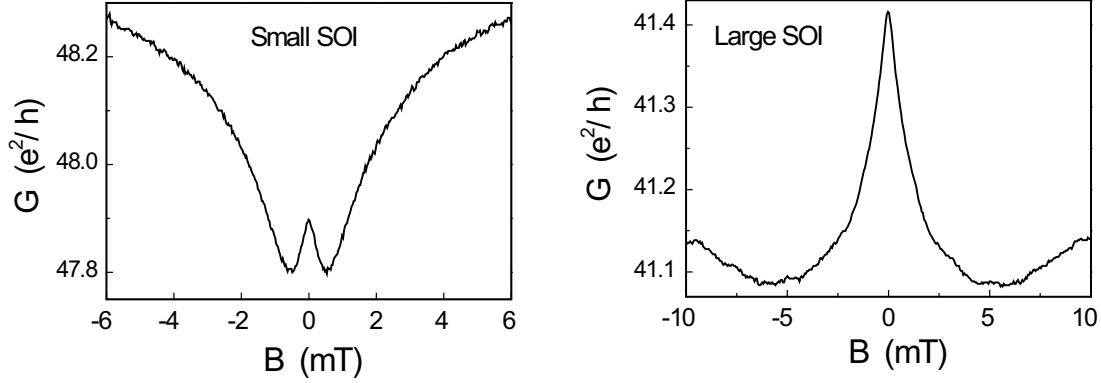
Figure 3.9: Typical magnetoconductance traces, measured in the Hall bar with the smallest Rashba SOI strength (left), and the strongest Rashba strength (right). The WAL peak around $B = 0$T is larger for the sample with larger Rashba SOI strength, consistent with theory. These measurements have been performed at $T = 1.6$K.

[3], and the elastic scattering time is typically between $0.2\,$ps and $1.2\,$ps (mobility between 1 and $6\,\mathrm{m}^2/$Vs), depending on the wafer and electron density.

Figure 3.10 gives an overview of the extracted values of the Rashba spin-split energy $\Delta = 2\alpha k_F$ for the three different wafers, for various values of the electron density n_e. Note that the wafer with the largest asymmetry in the confinement potential (see Fig. 3.4) has the largest Rashba strength α, or Rashba spin-split energy Δ, as expected. Notice further that the Rashba strength α tends to decrease with increasing electron density (see Fig. 3.4), but since simultaneously the Fermi wavevector k_F becomes larger, the Rashba spin-split energy $\Delta = 2\alpha k_F$ is relatively insensitive to the value of the electron density.

3.4 Measurement setup

In order to observe phase-coherent (and spin-dependent) transport phenomena in the ring structure and the Hall bars, it is necessary to perform the measurements at low temperatures. For the measurements of the AB conductance oscillations in the ring structure we have used a commercial ^{3}He fridge, with a base temperature of $T = 0.3\,$K. This ^{3}He fridge is equipped with a 9T superconducting magnet.

The measurements on the Hall bars have been performed in a commercial ^{4}He fridge, which reaches a base temperature of $T = 1.6\,$K (by vacuum pumping the Helium bath that surrounds the sample). This ^{4}He fridge is equipped with a 14T superconducting magnet. In addition, we have mounted home-made split-coils on the sample holder, in order to be able to apply simultaneously a small magnetic
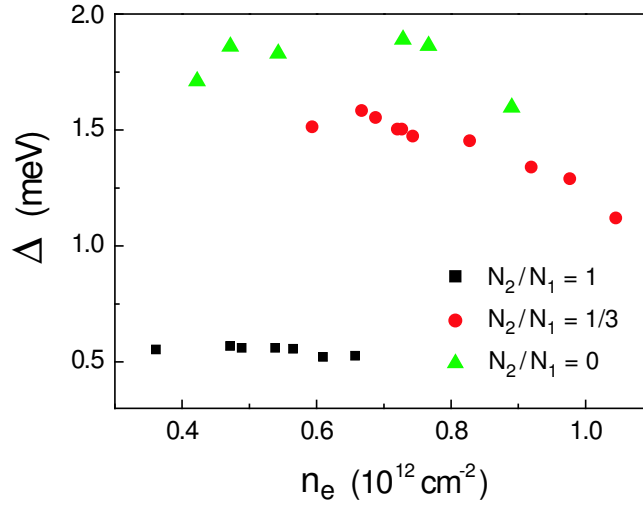
Figure 3.10: An overview of the extracted values of the Rashba spin-split energy $\Delta = 2\alpha k_F$ for the three different heterostructures, at various electron densities. These values are obtained by fitting the magnetoconductance, using the ILP theory [5].

field perpendicular to the field generated by the superconducting magnet. These split-coils generate approximately $45\,\mathrm{mT/A}$, and consist of $0.1\,\mathrm{mm}$ thick copper wire.

All the measurements have been performed by standard AC lock-in techniques, using either Princeton Applied Research lock-in amplifiers (ring structures), or Stanford Research Systems SR830 lock-in amplifiers (Hall bars).

References

[1] J. Nitta, T. Akazaki, H. Takayanagi, and T. Enoki, Phys. Rev. Lett. **78**, 1335 (1997)

[2] J. Nitta, T. Akazaki, H. Takayanagi and T. Enoki, Physica E **2**, 527 (1998)

[3] T. Koga, J. Nitta, T. Akazaki, and H. Takayanagi, Phys. Rev. Lett. **89**, 46801 (2002)

[4] J. Nitta, T. Koga, and H. Takayanagi, Physica E **12**, 753 (2002)

[5] S.V. Iordanskii, Y.B. Lyanda-Geller, and G.E. Pikus, JETP Lett. **60**, 206 (1994) [Pis'ma Zh. Eksp. Teor. Fiz. **60**, 199 (1994)]

[6] F.E. Meijer, A.F. Morpurgo, T.M. Klapwijk, T. Koga, and J. Nitta, Phys. Rev. B **70**, 201307(R) (2004)

Chapter 4

1D ring in the presence of Rashba spin-orbit interaction: Derivation of the correct Hamiltonian

We describe in detail the procedure for obtaining the correct 1D Hamiltonian of electrons moving on a ring in the presence of Rashba spin-orbit interaction. The subtlety of this seemingly trivial problem has not been fully appreciated so far and it has led to some ambiguities and errors in the existing literature. Our work illustrates the origin of these ambiguities and solves them.

4.1   Introduction

The effect of Rashba spin-orbit interaction (SOI) [1] on electrons moving in a mesoscopic ring has been studied in several contexts, such as magnetoconductance oscillations [2, 3], Peierls transition [4, 5] and persistent current [6, 7]. Essentially all these theoretical studies have employed one-dimensional (1D) model Hamiltonians. Since different Hamiltonians have been used by different authors some ambiguity currently exists with regard to the correct form of the 1D Hamiltonian. For instance, Aronov and Lyanda-Geller, who studied the effect of Rashba SOI on the Aharonov-Bohm conductance oscillations [2], used a non-hermitean operator as Hamiltonian [8]. Zhou, Li and Xue [9] noticed this fact and derived a different (hermitean) Hamiltonian operator. However, in their Hamiltonian the Rashba SOI term originates from an electric field pointing in the radial direction and not in the direction perpendicular to the plane of the ring. This is physically not correct. Subsequently others [3, 5, 7, 10] have employed a now commonly used 1D Hamiltonian for electrons on a ring, without explicitly discussing its derivation.

The purpose of this Chapter is to clearly identify the origin of the existing ambiguity and to discuss in detail the procedure to obtain the correct 1D Hamiltonian operator for electrons moving on a ring in the presence of Rashba SOI. We will show that the subtlety of this seemingly trivial problem has not been fully appreciated so far.

4.2   Derivation of the correct Hamiltonian

The "conventional" way to obtain the Hamiltonian for a 1D ring from the Hamiltonian in two dimensions consists of two steps. First the Hamiltonian operator is transformed into cylindrical coordinates r and ϕ. Then r is set to a constant and all terms proportional to derivates with respect to r are discarded (i.e., set to 0). This procedure works correctly in simple cases, such as free electrons or electrons in the presence of a (uniform or textured [11]) magnetic field. However, it does not work in the presence of Rashba SOI, as we will illustrate below.

The 2D Hamiltonian for a single electron in the presence of Rashba spin-orbit interaction and a magnetic field is given by

$$\hat{H} \;=\; \frac{1}{2m}(\mathbf{p} - e\mathbf{A})^2 \;+\; \alpha\,\hat{\sigma}\cdot\mathbf{E}\times(\mathbf{p} - e\mathbf{A}) \;+\; \mu\,\hat{\sigma}\cdot\mathbf{B} \tag{4.1}$$

where $\mathbf{A}$ is the vector potential, α is the SOI constant, $\mathbf{E}$ and $\mathbf{B}$ are pointing

in the $\hat{z}$ direction (perpendicular to the plane). In cylindrical coordinates, with $x = r \cos \phi$ and $y = r \sin \phi$, this operator reads:

$$\hat{H}(r, \phi) = -\frac{\hbar^2}{2m} \left[\frac{\partial^2}{\partial r^2} + \frac{1}{r} \frac{\partial}{\partial r} - \frac{1}{r^2}(i \frac{\partial}{\partial \phi} + \frac{\Phi}{\Phi_0})^2 \right] +$$

$$- \frac{\alpha}{r} \left(\cos \phi \, \hat{\sigma}_x + \sin \phi \, \hat{\sigma}_y \right) (i \frac{\partial}{\partial \phi} + \frac{\Phi}{\Phi_0}) + \tag{4.2}$$

$$+ i\alpha \left(\cos \phi \, \hat{\sigma}_y - \sin \phi \, \hat{\sigma}_x \right) \frac{\partial}{\partial r} + \frac{\hbar \omega_B}{2} \hat{\sigma}_z$$

with Φ is the magnetic flux through the ring, $\Phi_0 = h/e$, and $\hat{\sigma}_{x,y,z}$ are the usual Pauli spin matrices. Notice also that we have redefined α ($\alpha \to \hbar E_z \alpha$).

If we now set r to a constant value ($r = a$) and neglect the derivative terms, we obtain

$$\hat{H}(\phi) = -\frac{\hbar^2}{2ma^2} (i \frac{\partial}{\partial \phi} + \frac{\Phi}{\Phi_0})^2 + \frac{\hbar \omega_B}{2} \hat{\sigma}_z$$

$$\tag{4.3}$$

$$- \frac{\alpha}{a} \left(\cos \phi \, \hat{\sigma}_x + \sin \phi \, \hat{\sigma}_y \right)(i \frac{\partial}{\partial \phi} + \frac{\Phi}{\Phi_0})$$

This operator, used by Aronov and Lyanda-Geller [2], is not hermitean, as can be easily shown by calculating its matrix elements in any complete basis; i.e., the "conventional" procedure fails.

In order to find the correct form for the 1D Hamiltonian we go back to the full 2D Hamiltonian (Eq. 4.2). To this Hamiltonian we add a potential $V(r)$, which forces the electron wavefunctions to be localized on the ring in the radial direction. Specifically $V(r)$ is small in a narrow region around $r = a$ and large outside this region. For a narrow ring (steep confining potential) the confining energy in the radial direction is much larger than the SOI energy, the Zeeman energy and the kinetic energy in the azimuthal direction. This allows us to solve the Hamiltonian for the radial wavefunction first and treat $\hat{H}_{SOI}$, $\hat{H}_{Zeeman}$ and $\hat{H}_{kin}(\phi)$ as a perturbation. Specifically we write $\hat{H} = \hat{H}_0 + \hat{H}_1$, where

$$\hat{H}_0 = -\frac{\hbar^2}{2m} \left[\frac{\partial^2}{\partial r^2} + \frac{1}{r} \frac{\partial}{\partial r} \right] + V(r) \tag{4.4}$$

and the perturbation Hamiltonian $\hat{H}_1$ is given by

$$\hat{H}_1 = \frac{\hbar^2}{2ma^2} \left(i\frac{\partial}{\partial\phi} + \frac{\Phi}{\Phi_0}\right)^2 + \frac{\hbar\omega_B}{2}\,\hat{\sigma}_z$$

$$- \frac{\alpha}{r}\left(\cos\phi\,\hat{\sigma}_x + \sin\phi\,\hat{\sigma}_y\right)\left(i\frac{\partial}{\partial\phi} + \frac{\Phi}{\Phi_0}\right) \qquad (4.5)$$

$$+ i\alpha\left(\cos\phi\,\hat{\sigma}_y - \sin\phi\,\hat{\sigma}_x\right)\frac{\partial}{\partial r}$$

The eigenfunctions of $\hat{H}_0$ are separable in r and ϕ, i.e. $\Psi(r,\phi) = R(r)\,\Phi(\phi)$, since $\hat{H}_0$ does not depend on ϕ. In the limit of a very narrow (1D) ring all electrons will be in the lowest radial mode $R_0(r)$. We then have an infinitely degenerate set of states $\Psi_n(r,\phi) = R_0(r)\,\Phi_n(\phi)$ over which we have to diagonalize $\hat{H}_1$. Here, the $\Phi_n(\phi)$ denote a complete set of spinors in the ϕ direction.

The matrix elements of $\hat{H}_1$ are calculated from

$$a_{mn} = \langle\Phi_m(\phi)|\langle R_0(r)|\,\hat{H}_1(r,\phi)\,|R_0(r)\rangle|\Phi_n(\phi)\rangle \qquad (4.6)$$

from which we can read the correct 1D Hamiltonian $\hat{H}(\phi)$ directly

$$\hat{H}_{1D}(\phi) = \langle R_0(r)|\,\hat{H}_1(r,\phi)\,|R_0(r)\rangle \qquad (4.7)$$

In order to obtain the 1D Hamiltonian explicitly, we have to calculate the lowest radial mode for a given confining potential. If we assume without loss of generality (since we will consider the limit of a truly 1D ring) a harmonic confining potential, $V(r) = \frac{1}{2}K(r-a)^2$, we have to solve

$$-\frac{\hbar^2}{2m}\left[\frac{\partial^2 R(r)}{\partial r^2} + \frac{1}{r}\frac{\partial R(r)}{\partial r}\right] + \frac{1}{2}K(r-a)^2 R(r) = E\,R(r) \qquad (4.8)$$

In the limit of a 1D ring we may neglect the $\frac{1}{r}\frac{\partial}{\partial r}$ term in comparison to the $\frac{\partial^2}{\partial r^2}$ term and obtain the harmonic oscillator equation [12]. The lowest energy normalized solutions is then given by

$$R_0(r) = \left(\frac{\gamma}{a\sqrt{\pi}}\right)^{\frac{1}{2}} e^{-\frac{1}{2}\gamma^2(r-a)^2} \qquad (4.9)$$

where $\gamma^4 = mK/\hbar^2$. The 1D limit is achieved by letting γ go to infinity.

From Eqs. (4.5) and (4.7) we can now derive the 1D Hamiltonian explicitly. Since $\hat{H}_1$ contains terms dependent or r and derivatives with respect to r we have to calculate their expectation value. We obtain the following result

$$\langle R_0(r)| \frac{1}{r} |R_0(r)\rangle \;=\; \int_0^\infty R_0^2(r)\, dr \;=\; \frac{1}{a} \tag{4.10}$$

and the expectation value of $\frac{\partial}{\partial r}$ is given by

$$\langle R_0(r)| \frac{\partial}{\partial r} |R_0(r)\rangle \;=\; \int_0^\infty R_0(r) \frac{\partial R_0(r)}{\partial r}\, r\, dr \;=\; -\frac{1}{2a} \tag{4.11}$$

From this we conclude that we can not safely disregard the $\frac{\partial}{\partial r}$ term in order to obtain the correct 1D Hamiltonian.

It is worth stressing that it is not essential to choose a harmonic potential, nor to make any approximation as we have done above for simplicity, in order to obtain these results. To show this, let $|\rho_0(r)\rangle$ be the lowest radial mode for an arbitrarily given confining potential. We define $|\rho_0'(r)\rangle = \frac{1}{\sqrt{r}}|\rho_0(r)\rangle$. From direct calculations it follows that $\langle \rho_0|\frac{1}{2r} + \frac{\partial}{\partial r} |\rho_0\rangle = \langle \rho_0'| \frac{1}{r}\frac{\partial}{\partial r} |\rho_0'\rangle = \frac{1}{2} \rho_0'^2|_0^\infty = \frac{1}{2} r\rho_0^2|_0^\infty = 0$. We then obtain $\langle \rho_0| \frac{\partial}{\partial r} |\rho_0\rangle = -\langle \rho_0| \frac{1}{2r} |\rho_0\rangle$. Therefore for the lowest radial mode in the 1D limit we always get $\langle \rho_0| \frac{\partial}{\partial r} |\rho_0\rangle = -\frac{1}{2a}$, independent of the precise form of $|\rho_0(r)\rangle$ and thus of the precise shape of the radial confining potential which is used in the calculation.

Having established the generality of our result, we can now write the 1D Hamiltonian explicitly. From Eqs. (4.5),(4.7),(4.10) and (4.11) we obtain

$$\hat{H}_{1D}(\phi) \;=\; \frac{\hbar^2}{2ma^2} \left(i\frac{\partial}{\partial\phi} + \frac{\Phi}{\Phi_0}\right)^2 \;+\; \frac{\hbar\omega_B}{2}\, \hat{\sigma}_z$$

$$-\; \frac{\alpha}{a} \left(\cos\phi\, \hat{\sigma}_x + \sin\phi\, \hat{\sigma}_y\right) \left(i\frac{\partial}{\partial\phi} + \frac{\Phi}{\Phi_0}\right) \tag{4.12}$$

$$-\; i\frac{\alpha}{2a} \left(\cos\phi\, \hat{\sigma}_y - \sin\phi\, \hat{\sigma}_x\right)$$

This is the correct form of the 1D Hamiltonian operator for electrons on a ring, in the presence of Rashba SO interaction and Zeeman coupling.

The last term in Eq. (4.12) is neglected if we follow the "conventional" procedure. It is only recovered by following the procedure described above. In the simple cases mentioned earlier (e.g., free electrons), there are no terms present

in the Hamiltonian proportional to both $\frac{\partial}{\partial r}$ and some function of ϕ (i.e., the two dimensional Hamiltonian is separable). In these cases the "conventional" procedure produces the correct result. In all other cases it is necessary to take into account properly the confinement of the wavefunction in the radial direction as we have shown in this paper in order to obtain the correct 1D Hamiltonian on a ring.

4.3   Conclusions

In short, what we have described in this paper is a formally correct procedure to project the original Hamiltonian (Eq. 4.2) defined on the Hilbert space of spinors in two dimensions on a restricted Hilbert sub-space, spanned by the complete set of spinors $\Phi_n(\phi)$, which are function of the ϕ coordinate only.

References

[1] E.I. Rashba, Sov. Phys. Solid State. **2**, 1109 (1960)

[2] A.G. Aronov and Y.B. Lyanda-Geller, Phys. Rev. Lett. **70**, 343 (1993)

[3] Y.S. Yi, T.Z. Qian and Z.B. Su, Phys. Rev. B **55**, 10631 (1997)

[4] L. Hu, H. Li and G. He, Phys. Rev. B **62**, 16744 (2000)

[5] Y.S. Yi, A.R. Bishop, Phys. Rev. B **58**, 4077 (1998)

[6] S.L. Zhu, Y.C. Zhou and H.Z. Li, Phys. Rev. B **52**, 7814 (1995)

[7] T.Z. Qian, Y.S. Yi and Z.B. Su, Phys. Rev. B **55**, 4065 (1997)

[8] We note that the Hamiltonian used by Aronov and Lyanda-Geller becomes hermitean in the limit of large angular momentum ($\langle i\frac{\partial}{\partial \phi} + \frac{\Phi}{\Phi_0} \rangle \gg 1$). In this limit, the eigenfunctions of the Hamiltonian calculated by these authors are correct.

[9] Y.C. Zhou, H.Z. Li and X. Xue, Phys. Rev. B **49**, 14010 (1994)

[10] T. Choi, S.Y. Cho, C.M Ryu and C.K. Kim, Phys. Rev. B **56**, 4825 (1997)

[11] D. Loss, P. Goldbart and A.V. Balatsky, Phys. Rev. Lett. **65**, 1655 (1990); A. Stern, Phys. Rev. Lett. **68**, 1022 (1992)

[12] Using the resulting approximate radial wavefunction, Eq.(4.9), we obtain $\langle \frac{1}{r}\frac{\partial}{\partial r} \rangle / \langle \frac{\partial^2}{\partial r^2} \rangle = e^{-\gamma^2 a^2}/\gamma a\sqrt{\pi}$. This is a small quantity when the radius of the ring is much larger than the width of the arms which goes to zero for a truly 1D ring ($\gamma \to \infty$). Therefore $\langle \frac{1}{r}\frac{\partial}{\partial r} \rangle$ can be neglected in the 1D limit.

Chapter 5

Spin-induced geometrical phases in a 1D ring with Rashba SOI: a tuneable conductor

We propose a spin-based conductance modulator that does not require any ferromagnetic electrode or an external magnetic field. This device is based on quantum interference in an Aharonov-Bohm ring with tuneable Rashba SOI strength. We calculate the (spin-dependent) phase shifts between clockwise and anti-clockwise moving waves, and obtain the conductance of the ring as a function of the Rashba strength. We find that tuning the Rashba strength by means of a gate voltage allows to modulate the conductance of the ring.

5.1   Introduction

One of the most simple and appealing examples of using the spin degree of freedom for a conductance modulator, or field effect transistor (FET), was proposed by Datta and Das in 1990 [1]. As discussed in Chapter 1, the Datta-Das spin-FET consists of two ferromagnetic electrodes separated by a 2DEG with Rashba SOI. The key idea of this device is that the injected spins precess around the Rashba field when they are moving towards the collector. A modulation of the conductance is achieved by controlling the alignment of the carrier's spin with respect to the magnetization vector of the (ferromagnetic) collector electrode. Note that phase-coherence is not required for the operation of this spin-FET.

Since the functionality of the Datta-Das spin-FET depends crucially on the spin injection and -detection efficiency, large affords have been dedicated to demonstrate spin injection from ferromagnetic contacts into semiconductors. So far, the experimentally achieved spin injection is rather small, however, mainly due to the conductivity mismatch between the (metallic) ferromagnet and the (semiconducting) 2DEG with Rashba SOI [2]. Consequently, the expected conductance modulation in such structures is small (see also [3]). Another practical problem of the spin-FET is that the 2DEG is very sensitive to the perpendicular component of the stray field from the ferromagnetic electrodes [4].

In this Chapter we propose a spin-based conductance modulator that even works without any ferromagnetic electrodes and any external magnetic field. The conductance modulation is due to spin-dependent interference in an Aharonov-Bohm (AB) ring with Rashba SOI. In contrast to the Datta-Das spin-FET, our proposed "spin-interference device" utilizes the *phase-coherent* properties of the carrier's spin when it is moving around the ring, rather than controlling the carrier's spin-direction in space. Specifically, in this Chapter we calculate the spin-induced phase shifts that are acquired by the wavefunctions during a cyclic evolution in an AB ring with Rashba SOI, and show that these spin-induced phase shifts give rise to a large modulation of the conductance of the ring. Moreover, we show that the phase shifts, and hence the conductance of the ring, can be controlled by means of a gate voltage.

5.2   Eigenvalue equation for a 1D ring

To calculate the transport properties of a one dimensional ring in the presence of Rashba SOI and Zeeman coupling, we first calculate its eigenenergies and eigenstates. The Hamiltonian H for electrons moving on the 1D ring was derived in Chapter 4 and is given by

$$
\hat{H}_{\mathrm{1D}}(\phi) = \frac{\hbar^2}{2ma^2}\left(-i\frac{\partial}{\partial\phi}+\frac{\Phi}{\Phi_0}\right)^2 + \frac{\hbar\omega_B}{2}\,\hat{\sigma}_z
$$

$$
+ \frac{\alpha}{a}\left(\cos\phi\,\hat{\sigma}_x + \sin\phi\,\hat{\sigma}_y\right)\left(-i\frac{\partial}{\partial\phi}+\frac{\Phi}{\Phi_0}\right) \tag{5.1}
$$

$$
- i\frac{\alpha}{2a}\left(\cos\phi\,\hat{\sigma}_y - \sin\phi\,\hat{\sigma}_x\right)
$$

where $\hat{\sigma}_{x,y,z}$ are the Pauli matrices, a is the radius of the ring, $\Phi = \pi a^2 B_z$ is the magnetic flux through the ring, $\Phi_0 = h/e$ is the elementary flux quantum, and $\omega_B = eB_z/m_0$ is the Larmor frequency. By substituting the Pauli spin matrices explicitly, we obtain the following 2×2 Hamiltonian (with $\omega_0 = \hbar/ma^2$)

$$
\hat{H} = \begin{bmatrix} \dfrac{\hbar\omega_0}{2}\left(-i\dfrac{\partial}{\partial\phi}+\dfrac{\Phi}{\Phi_0}\right)^2 + \dfrac{\hbar\omega_B}{2} & \dfrac{\alpha}{a}\,e^{-i\phi}\left(-i\dfrac{\partial}{\partial\phi}+\dfrac{\Phi}{\Phi_0}-\dfrac{1}{2}\right) \\[3mm] \dfrac{\alpha}{a}\,e^{i\phi}\left(-i\dfrac{\partial}{\partial\phi}+\dfrac{\Phi}{\Phi_0}+\dfrac{1}{2}\right) & \dfrac{\hbar\omega_0}{2}\left(-i\dfrac{\partial}{\partial\phi}+\dfrac{\Phi}{\Phi_0}\right)^2 - \dfrac{\hbar\omega_B}{2} \end{bmatrix} \tag{5.2}
$$

In order to find the eigenfunctions and eigenenergies, we first note that the Hamiltonian is rotationally invariant, and hence the total angular momentum in the z direction, J_z, is conserved. Formally, this can be shown by the fact that $J_z = -i\frac{\partial}{\partial\phi}+\frac{1}{2}\sigma_z$ commutes with the Hamiltonian, i.e. $[J_z,H]=0$. Consequently, the eigenfunctions of the Hamiltonian (5.2) can be written as the eigenfunctions of the J_z operator times a two-component spinor $|\sigma\rangle$, i.e.

$$
\Psi_\sigma(\phi) = e^{in\phi}\begin{bmatrix} 1 & 0 \\ 0 & e^{i\phi} \end{bmatrix}|\sigma\rangle \tag{5.3}
$$

with $J_z\Psi_\sigma(\phi) = (n+1/2)\,\Psi_\sigma(\phi)$. Note that n must be an integer for an isolated ring with no leads, to make the wavefunction single-valued $[\Psi_\sigma(\phi) = \Psi_\sigma(\phi+2\pi)]$. The spinor states $|\sigma\rangle$ and the eigenenergies E_σ can be found by inserting Eq. (5.3) into Hamiltonian (5.2). This yields the following eigenvalue equation

$$
\begin{bmatrix} \dfrac{\hbar\omega_0}{2}\left(n+\dfrac{\Phi}{\Phi_0}\right)^2 + \dfrac{\hbar\omega_B}{2} & \dfrac{\alpha}{a}\left(n+\dfrac{\Phi}{\Phi_0}+\dfrac{1}{2}\right) \\[3mm] \dfrac{\alpha}{a}\left(n+\dfrac{\Phi}{\Phi_0}+\dfrac{1}{2}\right) & \dfrac{\hbar\omega_0}{2}\left(n+\dfrac{\Phi}{\Phi_0}+1\right)^2 - \dfrac{\hbar\omega_B}{2} \end{bmatrix}|\sigma\rangle = E_\sigma|\sigma\rangle \tag{5.4}
$$

5.2.1 Eigenstates and eigenenergies for B=0

Let us first analyse the situation when $B = 0$, i.e., when ω_B and Φ vanish. The eigenenergies in this case are easily obtained by diagonalizing the 2×2 matrix, and we obtain the following energy spectrum

$$E_{\sigma=\pm} \;=\; \frac{\hbar\omega_0}{2}\left[\left(n+\frac{1}{2}\right)^2 + \frac{1}{4}\right] \;+\; \sigma\left(\left|n+\frac{1}{2}\right|\right)\left[\left(\frac{\hbar\omega_0}{2}\right)^2 + \left(\frac{\alpha}{a}\right)^2\right]^{1/2} \quad (5.5)$$

The corresponding eigenfunction depend on the spin-label σ, as well as on the sign of $(n + 1/2)$. Note that for electrons moving *anti-clockwise* we have $n + 1/2 > 0$, whereas for *clockwise* moving electrons we have $n + 1/2 < 0$. For anti-clockwise moving electrons $(n + 1/2 > 0)$, the eigenstates are given by

$$\Psi_\uparrow^+ \;=\; e^{in\phi}\begin{bmatrix} \sin\frac{\theta}{2} \\ \cos\frac{\theta}{2}\,e^{i\phi} \end{bmatrix} \qquad\qquad \Psi_\downarrow^+ \;=\; e^{in\phi}\begin{bmatrix} \cos\frac{\theta}{2} \\ -\sin\frac{\theta}{2}\,e^{i\phi} \end{bmatrix} \qquad (5.6)$$

with $\tan\theta = 2\,m\,a\,\alpha/\hbar^2$. In contrast, for clockwise moving electrons (i.e. for $n + 1/2 < 0$), the eigenstates are given by

$$\Psi_\uparrow^- \;=\; e^{-i|n|\phi}\begin{bmatrix} \cos\frac{\theta}{2} \\ -\sin\frac{\theta}{2}\,e^{i\phi} \end{bmatrix} \qquad\qquad \Psi_\downarrow^- \;=\; e^{-i|n|\phi}\begin{bmatrix} \sin\frac{\theta}{2} \\ \cos\frac{\theta}{2}\,e^{i\phi} \end{bmatrix} \qquad (5.7)$$

Figure 5.1 shows the spin eigenstates for the clockwise and anti-clockwise moving electrons. It follows that the spin is describing a solid angle 2θ as it is travelling around the ring. It is interesting to note that the solid angle θ does not depend on the value of n, i.e. the solid angle does *not* depend on the magnitude of the velocity of the electron, nor on the Fermi energy. Notice, however, that the direction (and magnitude) of the Rashba field $\boldsymbol{B}_R$ do depend on the momentum and travel direction of the electrons. Finally, notice that the spin eigenstate is not exactly aligned with the Rashba field, i.e. the spin does not adiabatically follow the local Rashba field $\boldsymbol{B}_R$. Only in the limit of very strong Rashba SOI, i.e. when $\tan\theta \to \infty$, the spin dynamics becomes adiabatic, and the spin will follow exactly the local direction of $\boldsymbol{B}_R$.

5.3   Conductance of a 1D ring with Rashba SOI

Let us proceed by discussing the transport properties of the 1D ring when two current leads are connected to it (see Fig. 5.1). Consider an electronic wave,
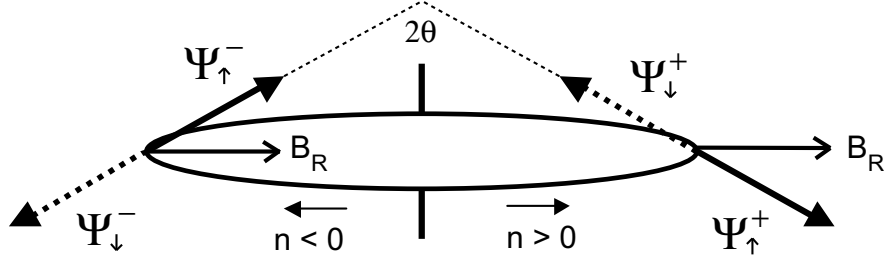
Figure 5.1: Schematic overview of the spin-direction of the four eigenstates ($\Psi^{\pm}_{\uparrow,\downarrow}$) in the ring. The solid and dashed arrow indicate the spin-up and spin-down state, respectively. The spin is not exactly aligned with the Rashba field B_R, but describes a solid angle 2θ (with $\tan\theta = 2\,m\,a\,\alpha/\hbar^2$), independent of the velocity ($\propto n$) of the electron. Depending on the travel direction, n is either positive or negative.

incident to the ring. When the wave arrives at the ring it will generally split into four partial waves (there are two possible travel directions around the ring, and two possible spin states for each travel direction). All four partial waves have acquired a certain phase when they arrive at the outgoing current lead. Depending on the phase difference between the partial waves, the interference at the outgoing current lead can be constructive or destructive. Hence the conductance of the ring crucially depends on the acquired phase differences (as well as the final spin directions of the four partial waves at the outgoing lead, since waves with orthogonal spins do not interference).

Formally, in the linear regime, the conductance is described by the Landauer formula [5, 6]

$$G = \frac{e^2}{h} \sum_{m',m=1}^{M} \sum_{\sigma',\sigma} T^{\sigma',\sigma}_{m',m} \tag{5.8}$$

where $T^{\sigma',\sigma}_{m',m}$ denote the transmission probability between incoming (m,σ) and outgoing (m',σ') states, where m is the mode index and σ is the spin state. For a 1D (single-mode) ring we have $M = m = m' = 1$. In order to calculate $T^{\sigma',\sigma}$ in a convenient way, we choose different spin quantization axes for σ and σ'. Specifically, we choose the spin quantization axes for σ and σ' in the direction of the spin eigenstates in the ring at the incoming and outgoing lead, respectively (i.e. the angle between the quantization axes σ and σ' is 2θ). Assuming strong coupling between the ring and the current leads, and neglecting waves that travel

around the ring more than once before leaving the ring, $T^{\sigma',\sigma}$ is in the lowest order approximation given by

$$T^{+,+} \;=\; \frac{1}{4}\,|\,e^{in^+_\downarrow \pi} + e^{-i|n^-_\uparrow|\pi}\,|^2 \;=\; \frac{1}{2}\,\big[\,1\,+\,\cos\pi(n^+_\downarrow - |n^-_\uparrow|)\,\big] \tag{5.9}$$

$$T^{-,-} \;=\; \frac{1}{4}\,|\,e^{in^+_\uparrow \pi} + e^{-i|n^-_\downarrow|\pi}\,|^2 \;=\; \frac{1}{2}\,\big[\,1\,+\,\cos\pi(n^+_\uparrow - |n^-_\downarrow|)\,\big] \tag{5.10}$$

$$T^{+,-} \;=\; T^{-,+} \;=\; 0 \tag{5.11}$$

where n^λ_σ denotes the quantum number of the wave with spin σ and travel direction λ. Note that for clockwise moving electrons $n^-_{\uparrow,\downarrow} < 0$ by definition (and $n^+_{\uparrow,\downarrow} > 0$). To avoid any possible confusion with signs, we have written $n^-_{\uparrow,\downarrow} = -|n^-_{\uparrow,\downarrow}|$. Using this notation, the conductance of the ring in the simplified case discussed above is given by

$$G \;=\; \frac{e^2}{h}\,\big[\,1\,+\,\frac{1}{2}\cos\pi(n^+_\downarrow - |n^-_\uparrow|)\,+\,\frac{1}{2}\cos\pi(n^+_\uparrow - |n^-_\downarrow|)\,\big] \tag{5.12}$$

Due to the two external leads the values of n^λ_σ no longer need to be an integer. In fact, the good coupling to the leads imposes that the energy of all four partial waves is equal to the Fermi energy, i.e. $E_\sigma(n^\lambda_\sigma) = E_F$. Hence, the value of $n^+_\uparrow - |n^-_\downarrow|$ at the Fermi level can be obtained from the following equation

$$E_F \;=\; \frac{\hbar\omega_0}{2}\Big[\big(n^+_\uparrow + \tfrac{1}{2}\big)^2 + \tfrac{1}{4}\Big]\,+\,\big(\,|n^+_\uparrow + \tfrac{1}{2}|\,\big)\Big[\big(\tfrac{\hbar\omega_0}{2}\big)^2 + \big(\tfrac{\alpha}{a}\big)^2\Big]^{1/2}$$
$$\tag{5.13}$$
$$=\; \frac{\hbar\omega_0}{2}\Big[\big(-|n^-_\downarrow| + \tfrac{1}{2}\big)^2 + \tfrac{1}{4}\Big]\,-\,\big(\,|-|n^-_\downarrow| + \tfrac{1}{2}|\,\big)\Big[\big(\tfrac{\hbar\omega_0}{2}\big)^2 + \big(\tfrac{\alpha}{a}\big)^2\Big]^{1/2}$$

From this equation we find the following (exact) expressions

$$|n^-_\downarrow| - n^+_\uparrow \;=\; 1 + \sqrt{1 + \big(\tfrac{2ma\alpha}{\hbar^2}\big)^2} \;=\; 1 + \sqrt{1 + \tan^2\theta} \;=\; 1 + \frac{1}{|\cos\theta|} \tag{5.14}$$

$$n^+_\downarrow - |n^-_\uparrow| \;=\; 1 - \sqrt{1 + \big(\tfrac{2ma\alpha}{\hbar^2}\big)^2} \;=\; 1 - \sqrt{1 + \tan^2\theta} \;=\; 1 - \frac{1}{|\cos\theta|} \tag{5.15}$$

Note that the above result does *not* depend on the precise value of the Fermi energy, but only on the solid angle θ. The conductance of the 1D ring is obtained by inserting Eqs. (5.14) and (5.15) into Eq. (5.12), and is explicitly given by the following three equivalent expressions

$$
\begin{aligned}
G &= \frac{e^2}{h} \left[1 - \cos\left(\frac{\pi}{\cos\theta}\right) \right] \\[2mm]
&= \frac{e^2}{h} \left[1 - \cos\left[\pi \sqrt{1 + \left(\frac{2ma\alpha}{\hbar^2}\right)^2} \right] \right] \\[2mm]
&= \frac{e^2}{h} \left[1 + \cos\left[2\pi a \frac{m\alpha}{\hbar^2} \sin\theta - \pi(1 - \cos\theta) \right] \right]
\end{aligned}
\tag{5.16}
$$

From the above expression it follows that the conductance of the ring depends crucially on the Rashba SOI strength α. The right-hand side of Fig. 5.2 shows the conductance of the 1D ring as a function of the Rashba strength, or more precise as a function of the parameter $2\,m\,a\,\alpha/\hbar^2 = \tan\theta$. The conductance shows quasi-periodic oscillations as a function of $2\,m\,a\,\alpha/\hbar^2$, which become periodic for $2\,m\,a\,\alpha/\hbar^2 \gg 1$ (i.e. in the adiabatic regime, when the spin is pointing parallel or anti-parallel to the Rashba field $\boldsymbol{B}_R$).

The left-hand side of Fig. 5.2 shows our proposed (spin-based) conductance modulator device. It simply consists of a ring structure that is fully covered with a gate electrode, in order to be able to control the Rashba strength, $\alpha(V_g)$.
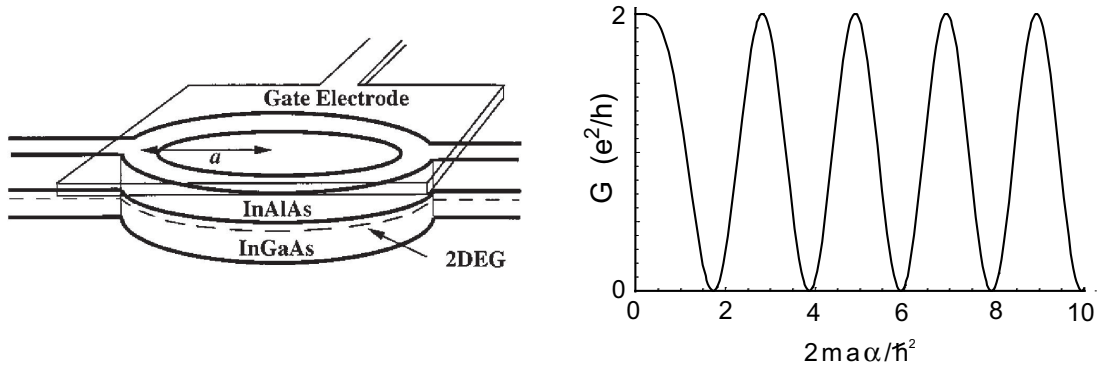

Figure 5.2: *Left:* Schematic picture of the proposed "spin-interference device", consisting of a (1D) ring structure in which the Rashba strength α is tuneable by a gate voltage. *Right:* The conductance G of the 1D ring as a function of the Rashba strength α, or more precise $2ma\alpha/\hbar^2$ (with m is the effective mass). The conductance is found to be quasi-periodic, and becomes periodic in the adiabatic regime, i.e. for $2ma\alpha/\hbar^2 \gg 1$.

In realistic devices the Rashba strength α can be tuned e.g. from $\alpha = 0.65 - 1.05 \cdot 10^{-11}$eVm [7], and hence, taking a ring with radius $a = 0.5\mu$m, and a material system with effective electron mass $m = 0.041m_0$, the phase-difference can be tuned from $\Delta\phi = \pi/\cos\theta = (2.58 - 4.64)\ \pi$. In other words, the spin-induced phase difference can be tuned by more than 2π, and consequently a large conductance modulation of the ring can be expected in experimentally accessible devices.

It is worth pointing out that the above described interference effect is expected to be robust, since the acquired phase-difference does not depend on the value of the Fermi energy itself (see Eqs. (5.14) and (5.15)). Furthermore, the independence of the phase-difference on the Fermi energy also implies that the conductance modulation will be present in a ballistic *multi-mode* ring; for each radial mode the phase-difference is given by Eqs. (5.14) and (5.15), and hence, if the different radial modes do not mix in the interference process, the conductance modulation of a multi-mode ring is still given by Eq. (5.16). Recently, it was confirmed theoretically that the conductance modulation of a 2D ring is indeed similar to the above discussed 1D case [5].

5.4   Connection to geometrical spin phases

The above obtained phase-difference, which gives rise to a modulation of the conductance of the 1D ring, is also interesting from a fundamental point of view: the (spin-induced) phase-difference can be seen as the analogue of the Aharonov-Bohm (AB) phase. As is well known, an AB phase is acquired by a charged particle when it encircles a magnetic flux (or magnetic moment). In 1984 Aharonov and Casher discovered that a spin (or other neutral magnetic moment) does also accumulate a phase when it is encircling an electric charge, i.e. when a spin is moving in an electric field [8]. It has been demonstrated that the situation considered by Aharonov and Casher is similar to a 1D ring with Rashba SOI, and that the AC effect results in a (spin-dependent) phase shift in the wavefunction (the AC phase) [9, 10, 11]. Just as the AB phase is intimately related with a magnetic flux through the ring, also the (spin-induced) AC phase can be viewed as an effective spin-dependent magnetic flux through the ring ($\pm\frac{\Phi}{\Phi_0} \leftrightarrow \pm\frac{1}{2|\cos\theta|}$) [12], which modulates the conductance of the ring, as shown in Fig. 5.2.

The acquired Aharonov-Casher phase can be written as the sum of two phases, $2\pi a \frac{m\alpha}{\hbar^2}\sin\theta$ and $\pi(1 - \cos\theta)$, as is shown in the last expression in Eq. (5.16). The former term, $2\pi a \frac{m\alpha}{\hbar^2}\sin\theta$, is sometimes called the *dynamical* part of the AC phase, because of its dependence on the distance travelled by the electrons

$(= 2\pi a)$ [11]. The latter term, $\pi(1 - \cos\theta)$, is a *geometrical* (spin-)phase, since it only depends on the solid angle θ, and not on spatial parameters (note that the AC phase itself, $\pi/\cos\theta$, is also a geometrical phase). Such geometrical phases were discovered by Berry in 1984 [13] from the basic laws of quantum mechanics, and received considerable attention (see e.g. [10, 11, 12, 15]). Berry showed that the wavefunction obtains a non-trivial phase when a parameter in the Hamiltonian is changed in a cyclic and adiabatic way (the geometrical Berry phase [13]). The same holds true in the non-adiabatic limit, as was shown by Aharonov and Anandan [14]. Such a situation is realized in the 1D ring, since the spin-dynamics in the ring is cyclic (solid angle θ) and non-adiabatic (the spin is not exactly aligned with B_R), and hence the term $\pi(1 - \cos\theta)$ in Eq. (5.16) can be identified as the Aharonov-Anandan phase [11].

The experimental observation of the Aharonov-Anandan phase has already been realized in optical and NMR experiments [16]. However, the observation of the Aharonov-Anandan phase, or the Aharonov-Casher phase, in solid state systems has turned out to be very difficult in practice, as will be discussed in detail in Chapter 6.

5.5 Conclusions

In conclusion, we have demonstrated that the electron wavefunction acquires a spin-dependent geometrical Aharonov-Casher phase during a cyclic evolution in a 1D ring structure with Rashba SOI. The precise value of the phase-shift, and hence the conductance of the phase-coherent ring structure, is found to depend on the Rashba SOI strength. Therefore, we have proposed to utilize a ring structure, which is uniformly covered by a gate electrode to change the Rashba SOI strength, as a spin-based conductance modulator that does not require any ferromagnetic electrodes.

References

[1] S. Datta and B. Das, Appl. Phys. Lett. **56**, 664 (1990)

[2] G. Schmidt, D. Ferrand, L.W. Molenkamp, A.T. Filip, and B.J. van Wees, Phys. Rev. B **62**, 4790 (2000); A.T. Filip, B.H. Hoving, F.J. Jedema, and B.J. van Wees, Phys. Rev. B **62**, 9996 (2000)

[3] see for a review I. Zutic, J. Fabian, and S. Das Sarma, Rev. Mod. Phys. **76**, 323-410 (2004)

[4] M. Johnson, B.R. Bennett, M.J. Yang, M.M. Miller and B.V. Shanabrook, Appl. Phys. Lett. **71**, 974 (1997); F.G. Monzon, M. Johnson and M.L. Roukes, Appl. Phys. Lett. **71**, 3087 (1997)

[5] D. Frustraglia and K. Richter, Phys. Rev. B **69**, 235310 (2004)

[6] For a review see, e.g., S. Datta, *Electronic Transport in Mesoscopic Systems* (Cambridge Unversity Press, Cambridge, 1997)

[7] J. Nitta, T. Akazaki, H. Takayanagi, and T. Enoki, Phys. Rev. Lett. **78**, 1335 (1997)

[8] Y. Aharonov and A. Casher, Phys. Rev. Lett. **53**, 319 (1984)

[9] H. Mathur and A.D. Stone, Phys. Rev. Lett. **68**, 2964 (1992); M. Choi, Phys. Rev. Lett. **71**, 2987 (1993); A.G. Aronov and Y.B. Lyanda-Geller, Phys. Rev. Lett. **70**, 343 (1993)

[10] Y.S. Yi, T.Z. Qian, and Z.B. Su, Phys. Rev. B **55**, 10631 (1997)

[11] T.Z. Qian and Z.B. Su, Phys. Rev. Lett. **72**, 2311 (1994)

[12] Y. Meir, Y. Gefen, and O. Entin-Wohlman, Phys. Rev. Lett. **63**, 798 (1989); O. Entin-Wohlman, Y. Gefen, Y. Meir, and Y. Oreg, Phys. Rev. B **45**, 11890 (1992)

[13] M.V. Berry, Proc. R. Soc. London A **392**, 45 (1984)

[14] Y. Aharonov and J. Anandan, Phys. Rev. Lett. **58**, 2167 (1983)

[15] D. Loss, P. Boldbart and A.V. Balatsky, Phys. Rev. Lett. **65** 1655 (1990); A. Stern, Phys. Rev. Lett. **68**, 1022 (1992)

[16] R. Bhandari and J. Samuel, Phys. Rev. Lett. **60**, 1211 (1988); R.Y. Chiao, A. Antaramian, K. M. Ganga, H. Jiao, S. R. Wilkinson, and H. Nathel, Phys. Rev. Lett. **60**, 1214 (1988); D. Suter, K. T. Mueller, and A. Pines, Phys. Rev. Lett. **60**, 1218 (1988)

Chapter 6

Statistical significance of fine structure in the ensemble averaged Fourier spectrum of Aharonov-Bohm oscillations

We discuss a statistical analysis of Aharonov-Bohm conductance oscillations measured in a two-dimensional ring, in the presence of Rashba spin-orbit interaction. Measurements performed at different values of gate voltage are used to calculate the ensemble-averaged modulus of the Fourier spectrum and, at each frequency, the standard deviation associated to the average. This allows us to prove the statistical significance of a splitting that we observe in the h/e peak of the averaged spectrum. Our work illustrates in detail the role of sample specific effects on the frequency spectrum of Aharonov-Bohm conductance oscillations and it demonstrates how fine structures of a different physical origin can be discriminated from sample specific features.

6.1 Introduction

The investigation of Aharonov-Bohm (AB) conductance oscillations in mesoscopic devices permits to study different aspects of phase coherent transport of electrons. One of the aspects that has recently attracted considerable attention is the effect of the electron spin [1]. It has been theoretically predicted that in the presence of Rashba SOI, the electron spin modifies the properties of AB conductance oscillations in an observable way [2, 3].

Experimental attempts have been reported in which features observed in either the envelope function of the AB oscillations or their Fourier spectrum were attributed to the presence of Rashba SOI [4, 5]. In a few cases [5] these claims were based on the interpretation of *single* magnetoconductance measurements. The interpretation of such experiments is difficult, however, due to the sample specific nature of the h/e oscillations. In particular, a certain scatter configuration in the ring might cause features that are similar to features induced by SOI. In the analysis of past experiments this possibility has not been considered thoroughly.

In this Chapter we experimentally show how sample specific effects in the Fourier spectrum of the AB oscillations can be *quantifiably* suppressed in a controlled way. In particular, we perform a statistical analysis of the ensemble averaged Fourier spectrum. At each frequency, the mean Fourier amplitude and standard deviation are calculated. We find features in the averaged Fourier spectrum that are significantly larger than the standard deviation. These features can therefore be discriminated from remnant sample specific effects and their origin attributed to a different physical phenomenon, such as spin effects.

6.2 Experimental system

The AB oscillations used in our analysis have been measured in a two dimensional ring, fabricated from an InAs-inserted, InGaAs-based heterostructure (for details on the precise layer structure, see Chapter 3, Fig. 3.1). The Rashba SOI in this quantum well is particularly strong; $\alpha \approx 0.8 \times 10^{-11}$ eVm [6, 7]. A SEM picture of the ring structure is shown in Fig. 6.1. The mean radius and width of the arms of the ring are 350nm and 180nm, respectively (the electronic width of the arms of the ring is possibly somewhat smaller than the lithographic width, due to a (thin) depletion layer at the edges). The estimated mean free path is $\simeq 1\mu m$, which is smaller than the circumference of the ring and hence transport through the ring is quasi-ballistic. A gate electrode covering the ring permits to change the Fermi energy (and k_F), as well as the Rashba SOI strength [6].
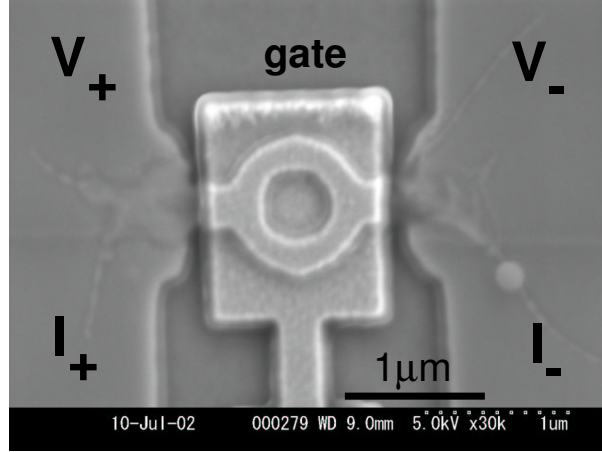
Figure 6.1: SEM picture of the Aharonov-Bohm ring structure. A gate electrode is covering the whole ring, allowing to change the electron density and the Fermi wavevector, as well as the Rashba SOI strength. The voltage and current contacts are indicated with $V_\pm$ and $I_\pm$, respectively.

6.3 Typical measurements

The magnetoconductance of the ring, $G(B)$, was measured at 49 different values of the gate voltage V_g, ranging from -55 mV to 195 mV ($\Delta V_g = 5$ mV), at a temperature of 300 mK. Three $G(B)$ curves, measured at different V_g, are shown in the left column of Fig. 6.2. Clearly visible in each $G(B)$ curve are a background increasing with magnetic field (due to the classical dynamics of the electron in a laterally confined geometry[8]), aperiodic conductance fluctuations, and periodic AB oscillations [9]. The middle column shows the AB oscillations obtained by subtracting the background from the $G(B)$ curve. Due to the small period of the oscillations, only the envelope function is visible. The right column shows the h/e peak in the Fourier spectrum.

Both the envelope function of the AB oscillations and its Fourier spectrum depend strongly on V_g. This strong V_g dependence is expected and well-known for random interference of electronic waves and shows that in a single $G(B)$ trace sample specific effects dominate the behavior of the measured AB oscillations. This precludes the attribution of a special meaning to any feature observed in a single measurement, since features appear and disappear randomly with V_g. Therefore, in practice, it is not possible to draw firm conclusions about the effect of SOI on the AB oscillations from a single $G(B)$ measurement [5].
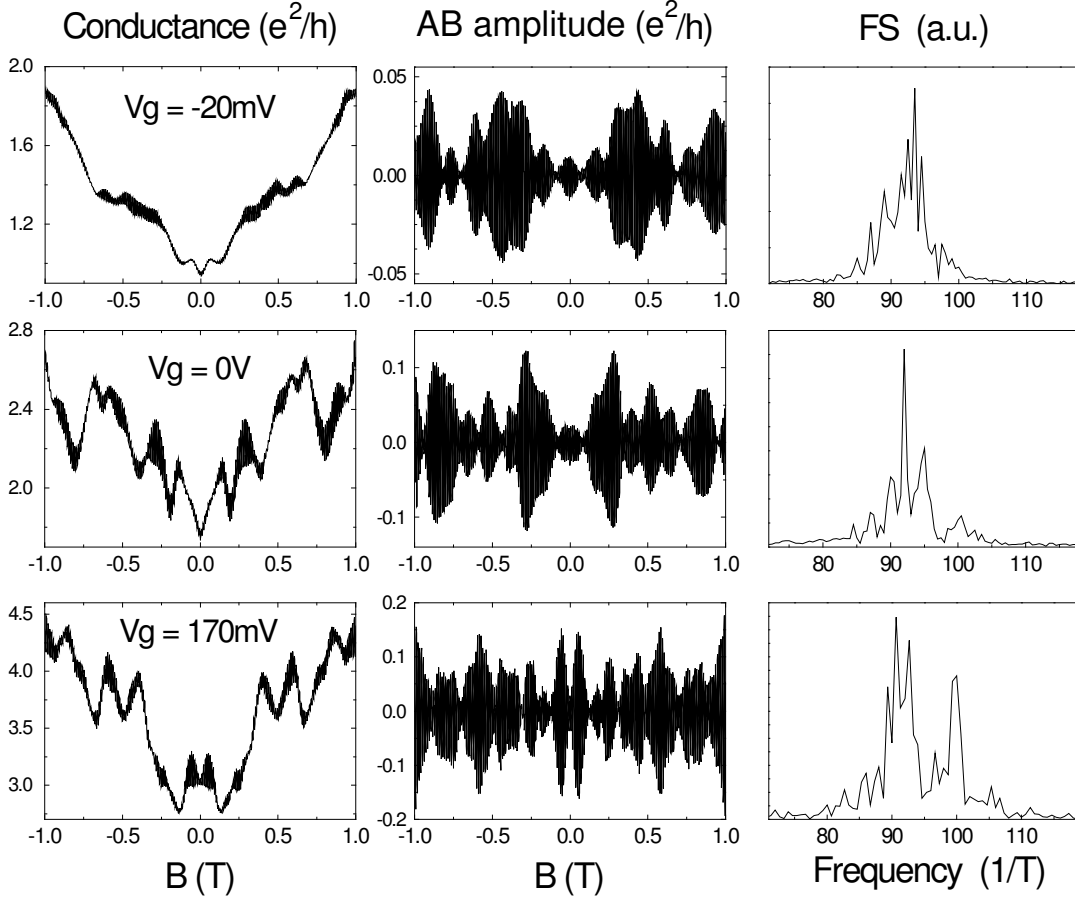
Figure 6.2: The magnetoconductance of a ring measured at different gate voltage at 300mK is shown in the left column. The envelope function of the AB oscillations, obtained by removing the positive magnetoconductance background, and the Fourier spectrum are shown in the middle and right column, respectively. It is apparent that both these quantities depend strongly on V_g, as it is typical for sample specific effects.

6.4   Suppression of sample specific effects

In order to put in evidence subtle effects possibly present in the AB oscillations, it is necessary to suppress sample specific features in a controlled way. This can be achieved by studying an *ensemble of measurements* [4], i.e. by averaging the modulus of the Fourier spectrum, $|G(\nu)|$, over different scatterer configuration. The ensemble averaged Fourier spectrum, $\langle|G(\nu)|\rangle$, is expected to be a smooth function, peaked at the frequency that corresponds to the mean radius of the ring. Superimposed on top of this smooth function, spin (or other) effects may show up as a splitting or another well-defined structure.

Theoretically, it has been proven that a (sufficiently large) change in Fermi energy is equivalent to a complete change in impurity configuration, insofar as the conductance oscillations are concerned [10]. For this reason we study the statistical properties of quantities averaged over an ensemble that consists of $G(B)$ curves measured at different gate voltage (with steps of $5\,\text{mV}$).

A "back of the envelope calculation" shows that steps of $5\,\text{mV}$ are sufficient to change the phase of the wavefunction $\Delta\phi$ between two scattering events by order unity, thereby satisfying the ergodic hypothesis [10]. Specifically, we have $dk_F/dn_e = \sqrt{\pi/2n_e}$, and $dn_e/dV_g \approx 1.7 \cdot 10^{16}\,\text{m}^{-2}/\text{V}$. Hence, for an electron density of $n_e \approx 1 \cdot 10^{16}\,\text{m}^{-2}$ and a mean free path $L_{tr} \approx 0.8\,\mu\text{m}$, the typical change phase between two scattering events with gate voltage is given by $\frac{\Delta\phi}{\Delta V_g} = L_{tr}\frac{dk_F}{dV_g} = L_{tr}\frac{dk_F}{dn_e} \cdot \frac{dn_e}{dV_g} \approx 170\,\text{V}^{-1}$. A change in gate voltage of $5\,\text{mV}$ gives therefore rise to a phase change $\Delta\phi$ of about unity, and measurements taken at different gate voltage are expected to be statistically independent.
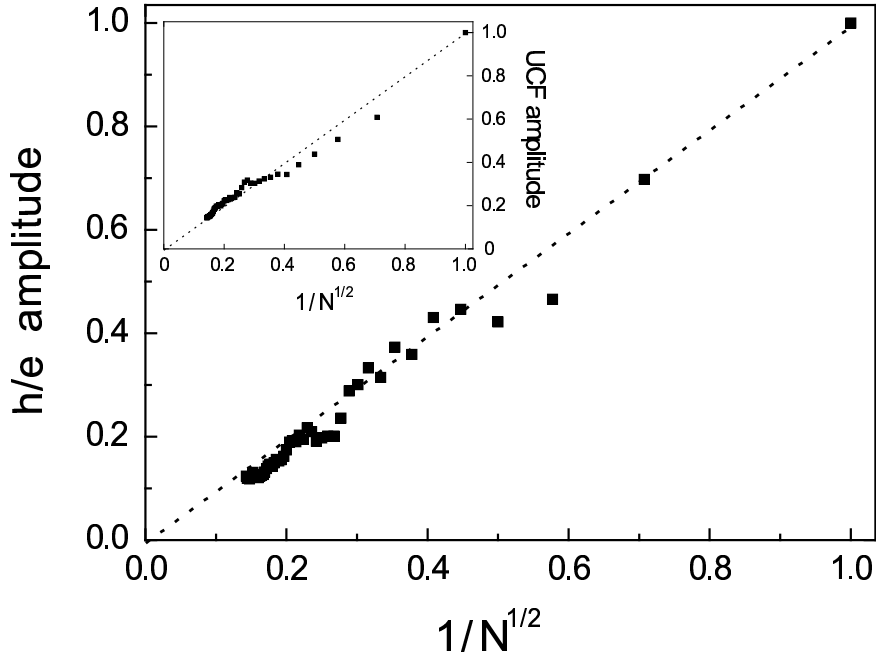

Figure 6.3: Mean amplitude of the h/e oscillations in the averaged magnetoconductance, as a function of the square root of the number N of curves used in calculating the average. The mean amplitude of the h/e oscillations is calculated by integrating the modulus of the Fourier spectrum over the width of the h/e peak. The insets shows the same analysis for the UCF amplitude (the UCF amplitude is here approximated by integrating the modulus of the Fourier spectrum beyond the $h/2e$ peak).

To show experimentally the statistical independence of $G(B)$ curves measured at different values of V_g we calculate the mean amplitude of the h/e oscillations upon averaging an increasing number N of $G(B)$ traces. The h/e oscillation amplitude in the averaged $G(B)$ is expected to be suppressed as $1/\sqrt{N}$, provided that the curves are statistically independent [11]. Fig. 6.3 shows that this is indeed the behavior observed experimentally [12]. In the inset of Fig. 6.3 we show that the (sample specific) aperiodic conductance fluctuations exhibit the same behavior, i.e. their amplitude decreases as $1/\sqrt{N}$ as well.

We note that in order to acquire the largest possible number of independent $G(B)$ curves, and therefore to obtain the largest suppression of sample specific effects, the entire range of V_g studied is rather large. This results in a sizeable (up to roughly a factor of 2) change of electron density and possibly also in a change of Rashba SOI strength, which may affect the shape of the averaged modulus of the Fourier spectrum, $\langle |G(\nu)| \rangle$. For this reason, we will first discuss the average over the whole V_g range, and then compare it to the average over a smaller V_g range. As we will show, the final results are similar for the two different V_g ranges, which suggests that the precise extension of the V_g range used in the experiments is not very critical.

6.5   Ensemble averaged Fourier spectrum

Fig. 6.4 shows a typical Fourier spectrum of a single $G(B)$ trace (upper graph), and the result of two different kinds of ensemble averaging, using the total set of 49 $G(B)$ curves measured from V_g= -55mV to 195mV. Specifically, the middle graph is a plot of the modulus of the Fourier spectrum of the average magnetoconductance, obtained by first averaging the magnetoconductance curves and then calculating the modulus of the Fourier spectrum ($\equiv |\langle G(\nu) \rangle|$). This quantity has been studied extensively in the past, and was shown to result in a suppression the h/e oscillation amplitude [11]. For this reason, the *relative* size of the sample specific structure in the Fourier spectrum does not decrease upon averaging, as it is apparent from the comparison of the upper and middle graph in Fig. 6.4. Therefore, this way of ensemble averaging does not allow the observation of subtle features possibly present in the h/e peak in the Fourier spectrum.

The bottom graph in Fig. 6.4 shows the ensemble average of the *absolute* value of the Fourier spectrum, $\langle |G(\nu)| \rangle$. This way of averaging does not suppress the h/e oscillations, since the phase information is discarded by taking the modulus of the Fourier spectrum of individual $G(B)$ traces before performing the average. This procedure results in a suppression of random features in the averaged Fourier
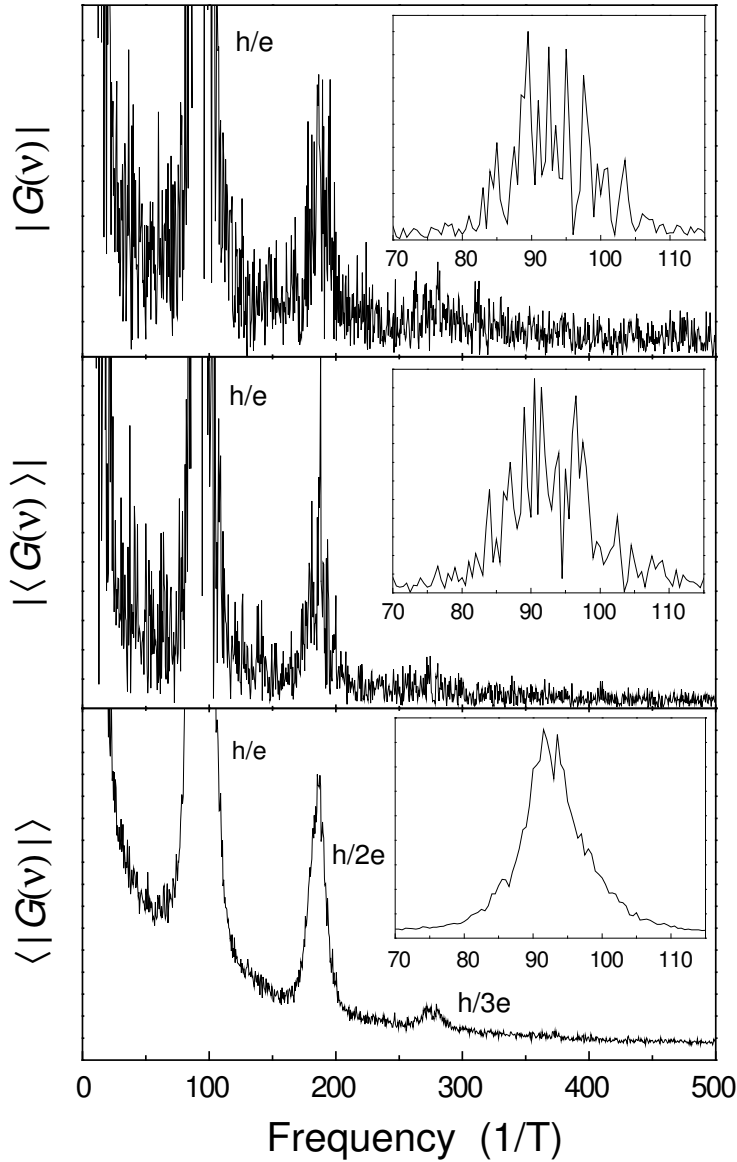
Figure 6.4: The random features present in the modulus of the Fourier spectrum of a single magnetoresistance curve (upper graph) are *not* suppressed in the modulus of the Fourier spectrum of the averaged $G(B)$, $|\langle G(\nu) \rangle|$ (middle graph). However, random features are clearly suppressed in the averaged modulus of the Fourier spectrum, $\langle |G(\nu)| \rangle$ shown in the bottom graph (in both the middle and in the bottom graph, the average is taken over $N = 49$ curves measured at different gate voltages). Note the much enhanced visibility of the $h/3e$ peak in $\langle |G(\nu)| \rangle$. The insets show the effect of samples specific features in the frequency range corresponding to the h/e peak. Also here the difference between the middle and bottom graph is obvious and a splitting is clearly visible in the h/e peak of in $\langle |G(\nu)| \rangle$ (note, in the main panel, that a small splitting is also present on top of the $h/3e$ peak)

spectrum, over the whole frequency range, as it is obvious from Fig. 6.4.

It was argued in ref [4] that this way of ensemble averaging provides information that is not easily accessible otherwise. The enhanced visibility of the third harmonic of the AB oscillations gives a direct experimental demonstration of this statement. This $h/3e$ peak is not observable in the Fourier spectrum of any single $G(B)$ curve nor in the Fourier spectrum of the averaged magnetoconductance, but it is clearly visible in the averaged modulus of the Fourier spectrum, $\langle|G(\nu)|\rangle$.

The insets in Fig. 6.4 zoom in on the h/e peak. It is apparent again that, in comparison to the upper two graphs, the sample specific "noise" is largely suppressed in the averaged modulus of the Fourier spectrum (bottom graph). In this quantity, a small splitting remains visible in the averaged h/e peak. Note that also the $h/3e$ peak in the bottom main figure shows a similar structure.

Without any further analysis, it is difficult to conclude what the origin of these features is. Specifically, this is because experimentally we only average over a finite number of scatter configurations so that the splitting may simply be some remnant sample specific structure. Only by quantifying the magnitude of these remnant features we can conclude if the splitting has physical significance.

6.6   Statistical analysis of the Fourier spectrum

We quantify the size of the remnant sample specific structure in terms of a frequency dependent standard deviation. This is obtained from the same set of N curves that we use to calculate the average modulus of the Fourier spectrum, $\langle|G(\nu)|\rangle$. At each fixed frequency ν, this set of curves corresponds to a set of N values of which we calculate the standard deviation $\sigma_{dis}(\nu)$. The statistical error associated with the average modulus of the Fourier spectrum at frequency ν is then $\sigma_{mean}(\nu) = \sigma_{dis}(\nu)/\sqrt{N}$ (central limit theorem). For an ideal ensemble average $N = \infty$ and $\sigma_{mean}(\nu) = 0$, i.e. sample specific effects are completely suppressed. However, if N is finite, $\sigma_{mean}(\nu)$ is also finite.

The upper panel of Fig. 6.5 shows the h/e peak of the averaged modulus of the Fourier spectrum and, for each frequency, $\sigma_{mean}(\nu)$, plotted as an error bar. In the main panel the average has been performed on $N = 16$ curves (with V_g ranging from -55mV to 95mV) and in the inset on $N = 49$ (V_g ranging from -55mV to 195mV). In both cases the size of the splitting is 3 to 4 times larger than σ_{mean}. The splitting is therefore statistically significant, and it is *not* due to remnant sample specific structure [13]. The size of any other structure observed in these averaged quantities is too small compared to $\sigma_{mean}(\nu)$ to exclude remnant sample specific effects as their origin. This is also true for the splitting in the
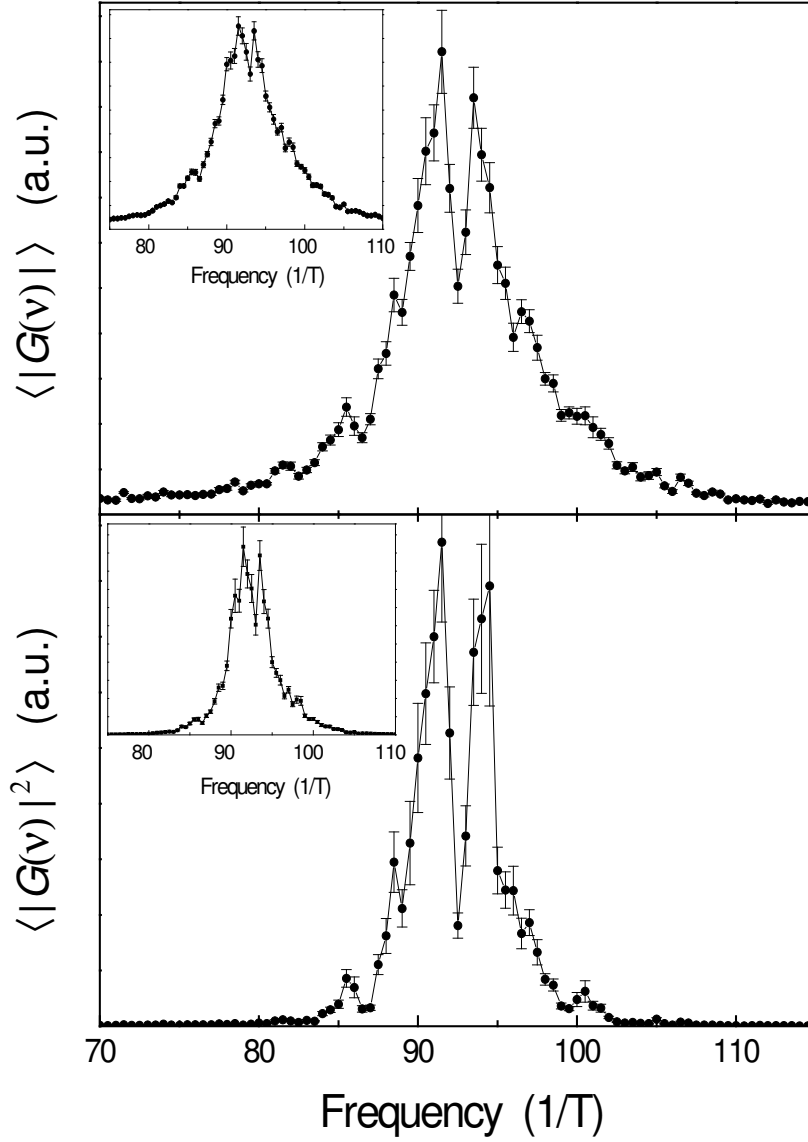
Figure 6.5: The upper graph shows the h/e peak in the averaged modulus of the Fourier spectrum and the associated statistical error σ_{mean}. The average is performed over $N = 16$ (main figure) and $N = 49$ (inset) curves, measured at different V_g. The bottom graph shows the same statistical analysis for the power spectrum. The observed splittings are significantly larger than the corresponding σ_{mean} and can therefore be discriminated from remnant sample specific features and attributed to a different physical phenomenon, such as a spin effect.
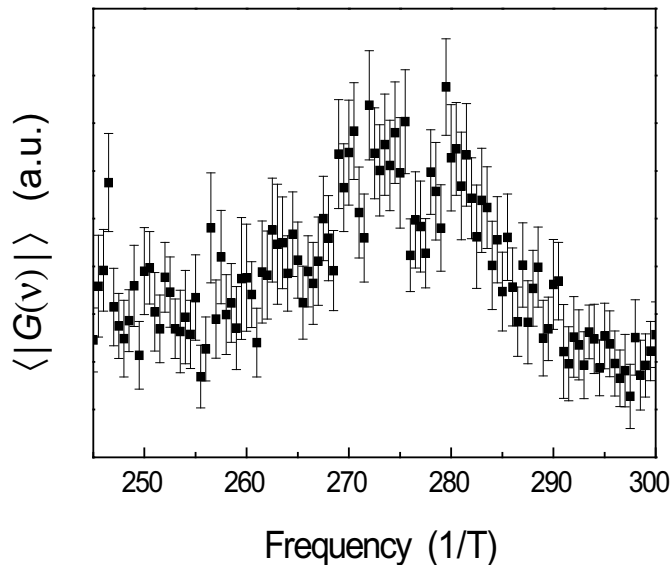
Figure 6.6: The $h/3e$ peak in the ensemble averaged modulus of the Fourier spectrum, and the associated statistical error σ_{mean} (indicated by the size of the error bar). The average is performed for $N = 49$ curves. The statistical analysis shows that the features in the $h/3e$ peak are not statistically significant, and can consequently not be discriminated from remnant sample specific features (the same is true for $N = 16$).

$h/3e$ peak visible in the bottom panel Fig. 3 (see Fig. 6.6).

We have also performed the same statistical analysis for the Fourier *power* spectrum [14]. The ensemble averaged Fourier power, $\langle|G(\nu)|^2\rangle$, and the associated statistical error, $\sigma_{power}(\nu)$, are shown in the bottom panel of Fig. 4 for $N = 16$ (main figure) and $N = 49$ (inset). Also here a statistically significant splitting is present in both cases.

The results shown in Fig. 6.5 indicate that the presence of a statistically significant splitting in the h/e peak is a robust feature. It does not depend on the precise gate voltage range used in our analysis, nor on the specific quantity analyzed, i.e. the modulus of the Fourier spectrum or the power spectrum. The result is also robust against different procedures used to calculate the Fourier spectra from the experimental data. We have analyzed our data with and without removing the background in the magnetoconductance in different ways and using different kinds of windowing procedures. In all cases the final results shows a similar, statistically significant splitting [15].

Our results confirm the conclusion of Ref. [4], namely that the h/e peak in the averaged Fourier spectrum is split in the presence of SOI, and put it on firmer grounds for two reasons. First, because the statistical analysis of the significance

of the splitting had not been previously performed. Second, because the same effect is observed in a different material system.

The size of the splitting measured here is roughly 3/T, smaller than the one found in Ref. [4] ($\approx$ 12/T). A direct comparison of the two results is however difficult, because the heterostructures used in the two experiments are different, as well as the radius of the rings (0.35 μm versus 1.05 μm). It was argued in Ref. [4] that the splitting may be a manifestation of the geometrical Berry phase. Subsequent theoretical works seem to consistently conclude that the effect of Berry phase alone is too small to account for the magnitude of the previously observed splitting [16]. This is also true for the magnitude of the splitting observed here, whose precise origin remains to be identified. More experimental work is needed to discriminate between different possible mechanisms capable of accounting for the experimental results (such as Rashba SOI [16, 3] or Zeeman coupling [3]). The work presented in this paper demonstrates a well-defined experimental procedure on which future experiments can be based.

6.7 Conclusions

In conclusion, we have discussed in detail the statistical properties of Aharonov-Bohm conductance oscillations measured in a ring with strong Rashba SOI, and have shown how random sample specific effects can be suppressed in a *quantifiable* way, up to a level that permits to reveal features of a different physical origin. In particular, we have observed a statistically significant splitting in the ensemble averaged Fourier spectrum, which is *not* a remnant sample specific feature, but possibly a manifestation of the presence of Rashba SOI.

References

[1] See, e.g., D. Loss, P. Goldbart and A.V. Balatsky, Phys. Rev. Lett **65**, 1655 (1990); A. Stern, Phys. Rev. Lett **65**, 1022 (1992)

[2] A.G. Aronov and Y.B. Lyanda-Geller, Phys. Rev. Lett. **70**, 343 (1993); Y.S. Yi, T.Z. Qian and Z.B. Su, Phys. Rev. B **55**, 10631 (1997)

[3] H.A. Engel and D. Loss, Phys. Rev. B **62**, 10238 (2000)

[4] A. F. Morpurgo, J. P. Heida, T. M. Klapwijk, B. J. van Wees, and G. Borghs, Phys. Rev. Lett. **80**, 1050 (1998)

[5] J.B. Yau, E.P. de Poortere and M. Shayegan, Phys. Rev. Lett. **88**, 146801 (2002); M.J. Yang, C.H. Yang, and Y.B. Lyanda-Geller, Europhys. Lett. **66**,

826 (2004)

[6] J. Nitta, T. Akazaki, H. Takayanagi and T. Enoki, Phys. Rev. Lett. **78**, 1335 (1997)

[7] The fabrication of the ring is described in J. Nitta, T. Koga and H. Takayanagi, Physica E **12**, 753 (2002)

[8] C.W.J Beenakker and H. van Houten, Solid State Phys. **44**, 1 (1991)

[9] Signs of weak anti-localization due to SOI are not visible in these $G(B)$ curves, since the associated magnetic field scale is well within one AB oscillation (see inset of Fig.2).

[10] B.L. Altshuler, V.E. Kravtsov and I.V. Lerner, JETP Lett. **43**, 441 (1986)

[11] See, e.g., R. Washburn and R. Webb, Rep. Prog. Phys. **55**, 1311 (1992)

[12] The mean h/e oscillation amplitude was normalized to unity for each $G(B)$ curve in order to ensure that each curve contributes equally to the average. We have checked that this normalization procedure does not affect our final results, presented in Fig.4: The same features are obtained using non-normalized $G(B)$ curves.

[13] Note that although more traces are used in the average over the larger V_g range the size of the splitting, measured in terms of σ, does not increase. This is possibly due to some averaging-out of SOI effects with large V_g ranges.

[14] The (ensemble averaged) Fourier power spectrum is equal to the Fourier transform of the (ensemble averaged) magnetic correlation function $\langle C(\Delta B) \rangle$, where $C(\Delta B) = \int G(B)G(B + \Delta B)\, dB$.

[15] The classical background and "edge effects" were found to result predominantly in low frequency components in the FS, far below the h/e peak. As a consequence, also the shape of the background (roughly above 25/T) is not/hardly affected.

[16] A.G. Malshukov, V.V. Shlyapin and K.A. Chao, Phys. Rev. B **60**, R2161 (1999); S.L Zhu and Z.D. Wang, Phys. Rev. Lett. **85**, 1076 (2000)

Chapter 7

Competition between Rashba spin-orbit interaction and Zeeman coupling in 2D electron gases

We investigate systematically how the interplay between Rashba spin-orbit interaction and Zeeman coupling affects the electron transport and the spin dynamics in InGaAs-based 2D electron gases. From the quantitative analysis of the magnetoconductance, measured in the presence of an in-plane magnetic field, we conclude that this interplay results in a spin-induced breaking of time reversal symmetry *and* in an enhancement of the spin relaxation time. Both effects are due to a partial alignment of the electron spin along the applied magnetic field, and are found to be in excellent agreement with recent theoretical predictions.

7.1   Introduction

Achieving control of the orbital motion of electrons by acting on their spin is a key concept in modern spintronics, and is at the basis of many proposals in the field of quantum information [1]. Two physical mechanisms are used to influence the dynamics of the electron spin in normal conductors: spin-orbit interaction (SOI) and Zeeman coupling. In the presence of elastic scattering, these two mechanisms affect the spin in different ways. SOI is responsible for the randomization of the spin direction whereas the Zeeman coupling tends to align the spin along the applied magnetic field. Depending on the relative strength of these interactions, this interplay of SOI and Zeeman coupling is responsible for the occurrence of a variety of physical phenomena [2, 3].

Quantum wells (QW) that define 2D electron gases (2DEGs) are particularly suitable for the experimental investigation of the competition between SOI and Zeeman coupling, since they give control over many of the relevant physical parameters. Specifically, in these systems the SOI strength can be controlled by an appropriate QW design [4] and by applying a voltage to a gate electrode [5]. The electron mobility is usually density dependent, so that the elastic scattering time can also be tuned by acting on the gate. Finally, Zeeman coupling to the spin can be achieved with minimal coupling to the orbital motion of the electrons by applying a magnetic field *parallel* to the conduction plane.

In this Chapter we study the competition of Rashba SOI and Zeeman coupling via magnetoconductance measurements in InGaAs-based 2DEGs with different Rashba SOI strength. From the detailed quantitative analysis of the weak anti-localization as a function of an applied in-plane magnetic field $B_\parallel$ (Zeeman coupling), we find that the partial alignment of the spin along $B_\parallel$ results in a spin-induced time reversal symmetry (TRS) breaking, and in an increase of the spin relaxation time. The increase in spin relaxation time is found to be quadratic with $B_\parallel$, and is strongly dependent on the SOI strength and the elastic scattering time. For both the spin-induced TRS breaking and the increase in spin relaxation time we find excellent quantitative agreement with recent theory. We also demonstrate that the quantitative analysis permits to determine the in-plane g-factor of the electrons in the quantum well.

7.2   Samples

The three InAlAs/InGaAs/InAlAs quantum wells used in this work are described in detail in Chapter 3 (see also [4]). Here, we recall that each well is designed to have a different Rashba SOI strength. The characteristic Rashba spin-split
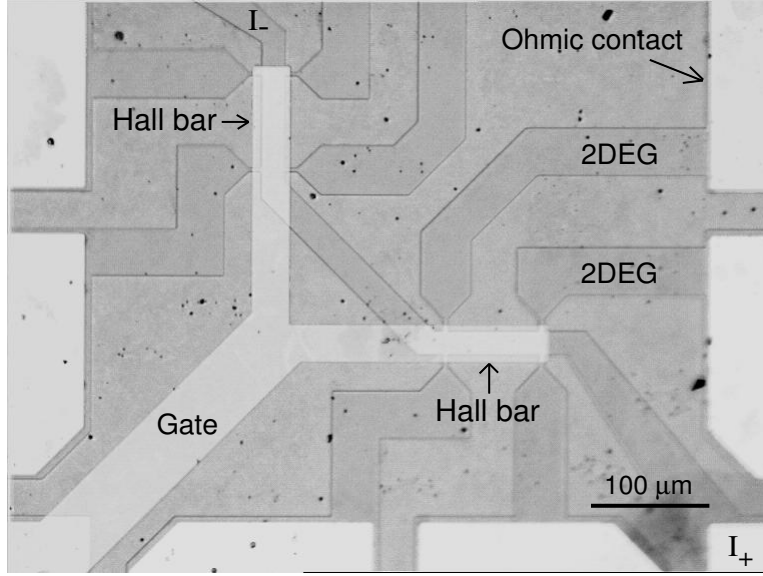
Figure 7.1: An optical picture of a fabricated sample, which consists of two Hall bars that are covered by a gate electrode (allowing to change the electron density, the elastic scattering time, and the Rashba SOI strength).

energy Δ for the different samples is typically $\Delta \approx 0.5, 1.5$ and $1.8\,\mathrm{meV}$ (in what follows we will refer to these samples as to samples 1, 2, and 3, respectively). The electron density and mobility at $V_{gate} = 0\,V$ are $n \simeq 7 \cdot 10^{15}\,m^{-2}$ and $\mu \simeq 4$ m^2/Vs. All measurements have been performed on 20 x 80 μm Hall-bar shaped devices (see Fig. 7.1), at $1.6\,\mathrm{K}$. A $14\,\mathrm{T}$ superconducting magnet is used to generate $B_\parallel$ (Zeeman coupling) and home-made split coils mounted on the sample holder are used to independently control the perpendicular field $B_\perp$. The value of $B_\perp$ is typically less than $40\,\mathrm{mT}$ (i.e., $B_\perp \ll B_\parallel$). Hence, the Zeeman coupling is created by $B_\parallel$, and $B_\perp$ is used to probe the small $B_\perp$-field quantum interference corrections to the conductance, i.e., the weak (anti-)localization signal.

We note that no significant difference in the results is observed when the in-plane field $B_\parallel$ is applied parallel or perpendicular to the direction of current flow.

7.3 Magnetoconductance in the presence of $B_\parallel$

To understand how an in-plane magnetic field (i.e., Zeeman coupling) affects the electronic transport, we first discuss the behavior of sample 1 with the weakest Rahsba SOI strength. Figure 7.2 shows the magnetoconductance of this sample
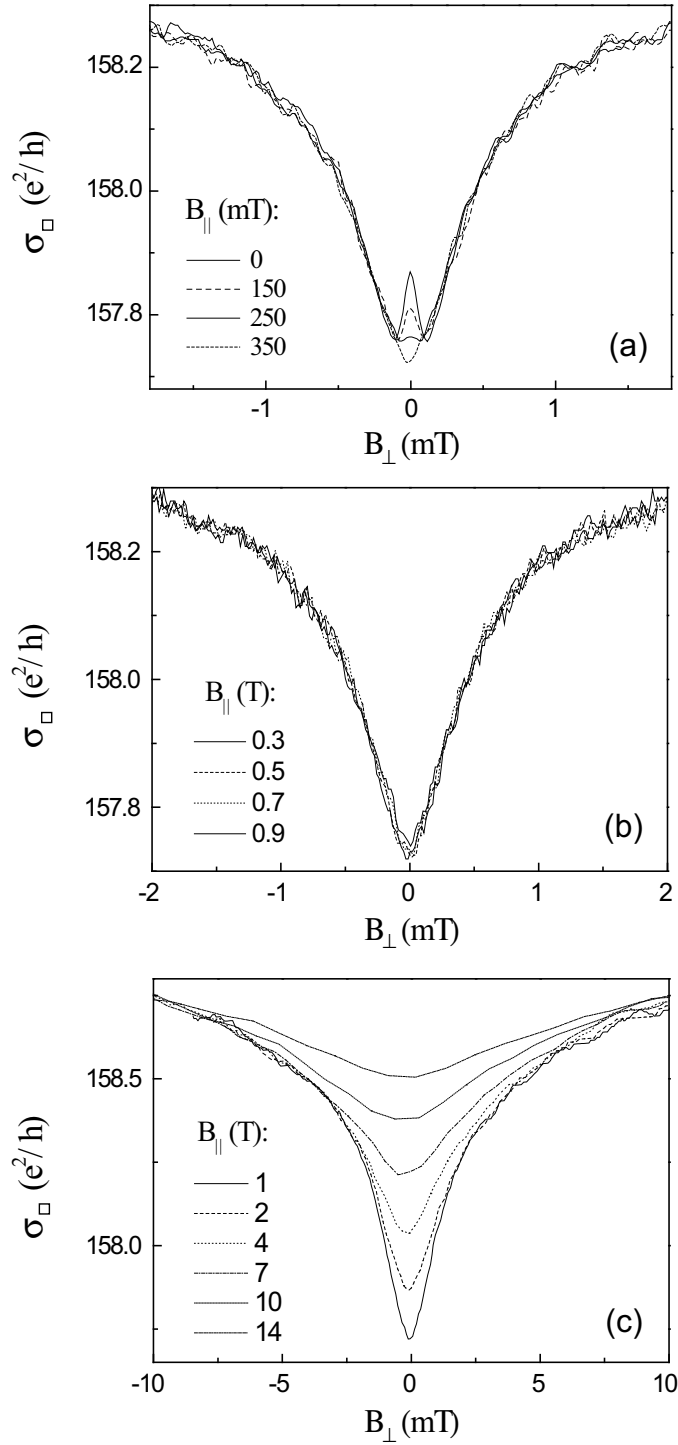
Figure 7.2: The magnetoconductance $\sigma(B_\perp)$ of sample 1 at different values of $B_\parallel$. Three regimes can be identified: increasing $B_\parallel$ from 0 to 350 mT results in a suppression of the weak anti-localization peak (a), increasing $B_\parallel$ further (up to about $B_\parallel = 1\,\mathrm{T}$) does not induce additional changes in the $\sigma(B_\perp)$-curves (b), for values of $B_\parallel$ larger than 1 T the weak localization becomes suppressed (c).

measured as a function of $B_\perp$ [7], for different *fixed* values of the in-plane field $B_\parallel$, i.e., for fixed values of the Zeeman coupling. For small values of $B_\parallel$ (main panel), the conductance exhibits a maximum at $B_\perp = 0$, due to weak anti-localization (WAL) superimposed on the background of weak-localization (WL) [8]. As $B_\parallel$ is increased, the amplitude of this maximum is reduced and eventually disappears around $B_\parallel = 300\,\mathrm{mT}$. A further increase in $B_\parallel$ does *not* result in additional changes of the magnetoconductance until $B_\parallel$ reaches approximately $1\,\mathrm{T}$ (Fig. 7.2b). Upon increasing $B_\parallel$ even further, the weak-localization signal is also suppressed on the scale of several ($\simeq 10$) Tesla (Fig. 7.2c).

These observations allow us to conclude that the suppression of weak anti-localization and of weak localization in a parallel field are due to *two distinct mechanisms* causing time reversal symmetry breaking. At large fields, $B_\parallel \gg 1\mathrm{T}$, weak localization (which is not sensitive to the spin degree of freedom) is suppressed due to TRS breaking caused by the coupling of $B_\parallel$ to the orbital motion of the electrons, owing to the finite thickness of the quantum well and the asymmetric confining potential [9] (see also Chapter 8). The suppression of the weak anti-localization peak at smaller values of $B_\parallel$ originates from a spin-induced TRS breaking due to the interplay between $B_\parallel$ (Zeeman coupling) and SOI, as predicted theoretically [10]. In this paper we will focus on the spin mechanism for TRS breaking, and discuss the orbital mechanism in Chapter 8.

The complete separation of spin and orbital TRS breaking, which is essential for the work presented here, has not been previously reported [3]. In our samples, this separation is due to the small quantum well thickness ($\approx 10nm$) and the small effective mass ($m^* \approx 0.041m_0$) which make the subband splitting in the quantum well relatively large, as well as to the relatively large gyromagnetic ratio ($g \simeq 3$) [9, 10]. It allows us to account for the magnetoconductance curves $\sigma(B_\perp)$ measured at $B_\parallel < 1\mathrm{T}$ in terms of existing theories that only consider the coupling of $B_\parallel$ to the electron spin, i.e to take only the Zeeman coupling into account, and neglect any orbital effect of $B_\parallel$. Therefore, the number of parameters that need to be introduced for the quantitative analysis of the data is the smallest possible. This makes it possible to extract the values of the phase coherence time and the spin relaxation time as a function of $B_\parallel$ (Zeeman coupling) with great accuracy, as it is needed to observe the dependence of τ_s on the in-plane magnetic field.

7.4 Quantitative analysis

We have performed a quantitative analysis of the magnetoconductance curves on all samples and for different values of the electron density n, using the theory of
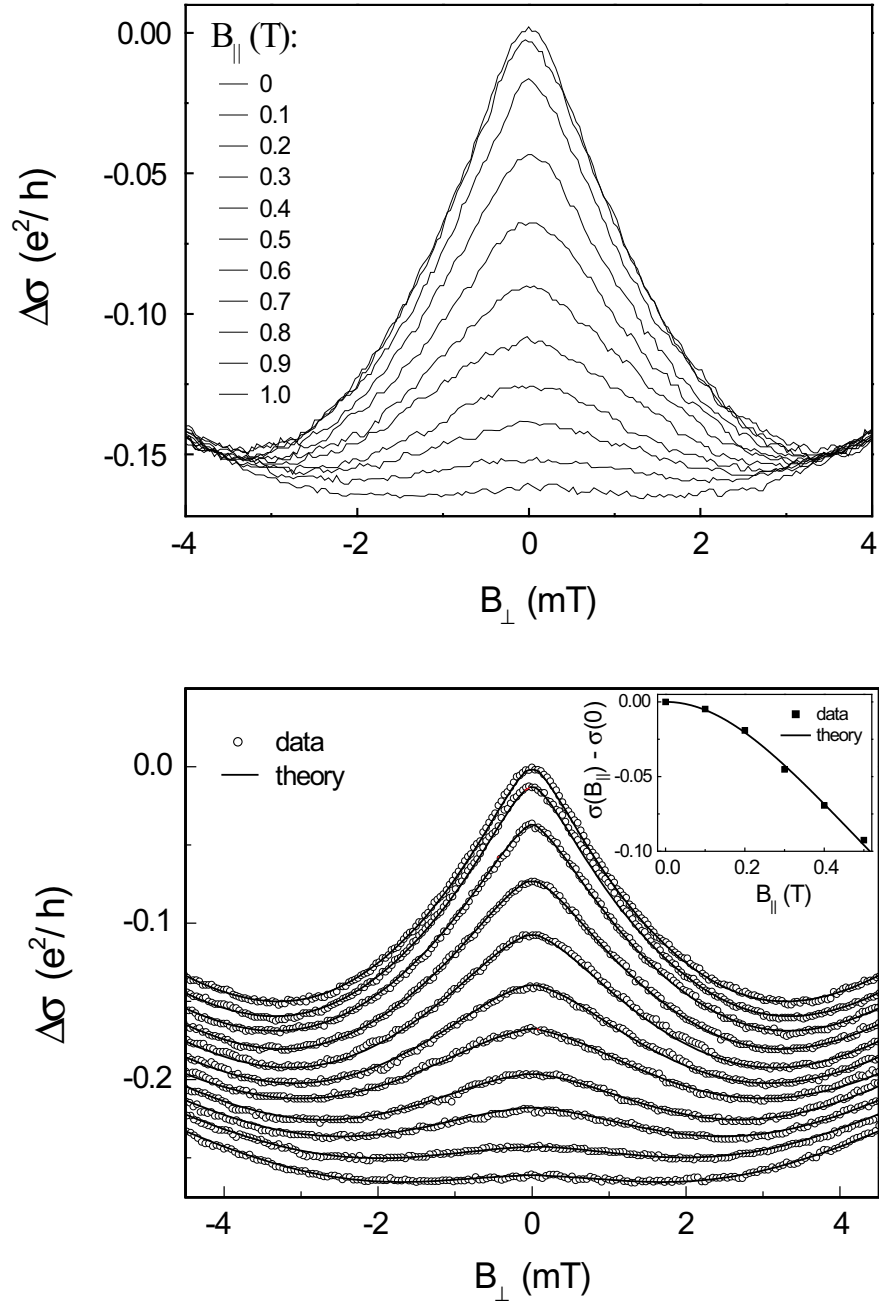
Figure 7.3: The upper graph shows the magnetoconductance of sample 2 at different fixed values of $B_\parallel$ from 0 to 1 T, in steps of 0.1 T (top to bottom). In bottom graph shows the same data (empty circles) together with the best fits to the ILP theory (solid line). The curves are shifted vertically for clarity. The inset shows the amplitude of the weak anti-localization peak at $B_\perp = 0$ as function of $B_\parallel$, i.e. $\sigma(B_\perp = 0, B_\parallel) - \sigma(0,0)$, and the best fit to the theory (solid line).

Iordanskii, Lyanda-Geller and Pikus (ILP) [11], as it is appropriate for our samples in which the spin relaxation is governed by the Dyakonov-Perel mechanism [12]. Specifically, we have used Eq. (13) of Ref. [11] to fit the $\sigma(B_\perp)$ curves measured at different values of the in-plane field. In all cases, the elastic scattering time τ and the diffusion constant were determined by conventional longitudinal and Hall resistance measurements, and the Dresselhaus term was set to zero [4]. Therefore, for each value of n and $B_\parallel$, the parameters τ_s and τ_ϕ are the only two remaining free fitting parameters. From this analysis, we find the $B_\parallel$-dependence of τ_s and τ_ϕ, i.e., $\tau_s(B_\parallel)$ and $\tau_\phi(B_\parallel)$ [13].

Here, $\tau_\phi(B_\parallel)$ denotes the upper time scale for interference between time-reversed waves. For $B_\parallel = 0$, this time scale is given by the inelastic scattering time $\tau_\phi(0)$. When $B_\parallel \neq 0$, the interplay between Rashba and Zeeman coupling is predicted to lead to a breaking of time-reversal symmetry, i.e., to a dephasing of time-reversed waves. The interplay is therefore expected to reduce the upper time scale of interference between reversed waves, i.e., this spin-induced mechanism adds to the inelastic scattering rate.

It is worth noting that in the ILP theory only one parameter is needed to account for the spin relaxation, since $\tau_s(0) \equiv \tau_{s_x}(0) = \tau_{s_y}(0) = 2\,\tau_{s_z}(0)$. In the presence of an in-plane field, however, these relations may not hold, since relaxing the spin along $B_\parallel$ costs energy ($\approx g\mu B_\parallel$) whereas relaxation in the direction perpendicular to $B_\parallel$ does not. Nevertheless, for sufficiently small $B_\parallel$ ($g\mu B_\parallel < kT$ and $\hbar/\tau_s(0)$), the ratios between the different relaxation times are expected to change only minorly under the conditions of our experiments. This allows us to treat $\tau_s(B_\parallel)$ as a *single* fitting parameter.

Figure 7.3 displays the measured magnetoconductance in sample 2 with the intermediate Rashba SOI strength (upper panel), and the results of the fitting procedure of the same set of data (lower panel). The continuous lines superimposed on the data in the lower panel represent the best fit to the ILP theory, and show that the agreement between data and theory is excellent for all values of $B_\parallel$ (i.e., for all values of the Zeeman coupling). Similar agreement is obtained for the other samples and for all the different values of the electron density n. The values of $\tau_\phi(B_\parallel)$ and $\tau_s(B_\parallel)$, as extracted from the fits, are shown in Figs. 7.4 and 7.5. Note that, since the electron mobility depends on the density, we are able to investigate how changing the elastic scattering τ affects the $B_\parallel$-dependence of the phase coherence and of the spin-relaxation time. This is of particular interest as both $\tau_\phi(B_\parallel)$ and $\tau_s(B_\parallel)$ are predicted to depend on the Dyakonov-Perel spin relaxation time $\tau_s(0)$ (see Eqs. 7.2 and 7.3), which is related to τ by the relation $1/\tau_s(0) = \Delta^2\tau/2\hbar^2$ [11].
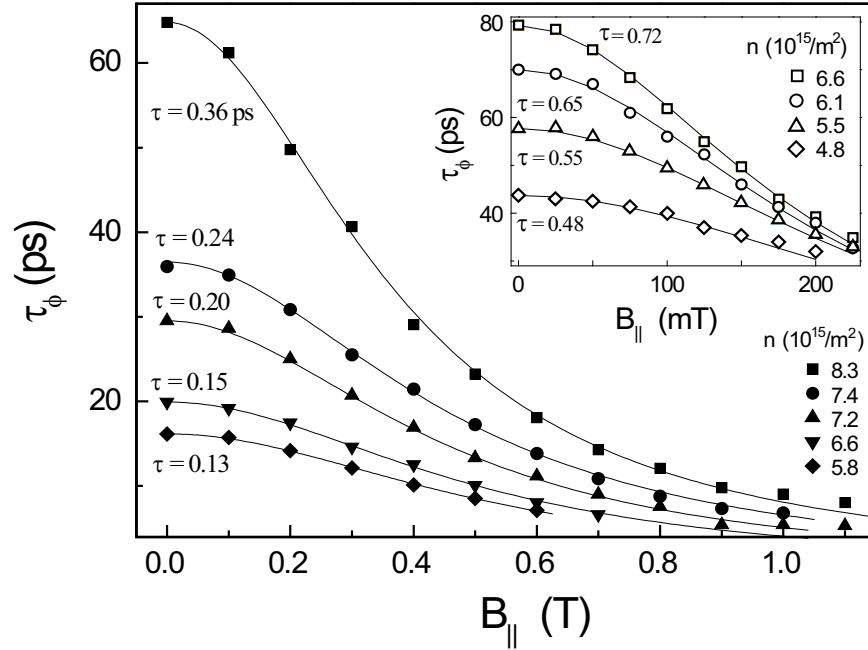
Figure 7.4: The symbols represent τ_ϕ as a function of $B_\parallel$, as extracted from the analysis of the magnetoconductance of sample 2, using the ILP theory (see Fig. 7.3). Different curves correspond to different values of n (and elastic scattering time τ). The solid lines are best fits based on the theory describing spin-induced dephasing [10]. The decrease of τ_ϕ with decreasing electron density is consistent with dephasing originating from electron-electron interaction. The inset shows the extracted $\tau_\phi(B_\parallel)$ and theoretical fits for sample 1.

7.5 The phase-coherence time: $\tau_\phi(B_\parallel)$

For all values of the electron density n, the measured $\tau_\phi(B_\parallel)$ decreases as a function of $B_\parallel$ (see Fig. 7.4), which shows quantitatively that the interplay between Rashba SOI and Zeeman coupling results in a breaking of time-reversal symmetry (TRS). Theoretically, the interplay is predicted to yield in a quadratic dependence of τ_ϕ on $B_\parallel$ [10], given by

$$\frac{\tau_\phi(B_\parallel)}{\tau_\phi(0)} = \frac{1}{1 + c B_\parallel^2} \tag{7.1}$$

where c is a constant given by:

$$c = \tau_\phi(0)\,\tau_s(0)\,(g_\parallel^*\,\mu_B/\hbar)^2 \tag{7.2}$$

and $g_\parallel^*$ is the in-plane g-factor. The solid lines in Fig. 7.4 are best fits to the data using Eq. (7.1) and treating c as a (density dependent) fitting parameter. Also in this case the agreement between experiment and theory is excellent for all values of n and for the different samples (the inset of Fig. 7.4 shows the behavior of sample 1. Equally good agreement is found for sample 3).

Using the value of c obtained from fitting the data of Fig. 7.4 we directly obtain $g_\parallel^*$ (Eq. 7.2). We find that, for each sample, the in-plane g-factor is approximately constant as a function of the electron density. The absolute values are determined to be $|g_\parallel^*| = 2.8 \pm 0.1$, $|g_\parallel^*| = 3.3 \pm 0.1$ and $|g_\parallel^*| = 3.5 \pm 0.1$, for samples 1, 2 and 3, respectively. Theoretically, the g-factor in our quantum well is predicted to depend substantially on its thickness, and is calculated to be $|g_\parallel^*| = 2.8$ and $|g_\parallel^*| = 3.5$ for a thickness of $10\,\mathrm{nm}$ and $15\,\mathrm{nm}$, respectively[14]. This agreement with theory gives additional support of our analysis in terms of spin-induced dephasing only, and shows that the measurement of weak anti-localization in the presence of an in-plane field permits to determine the in-plane g-factor. Contrary to other methods based on transport measurements, this method to determine the g-factor is suitable for disordered systems.

A different way to obtain $\tau_\phi(B_\parallel)$ (and c), apart from fitting the whole $\sigma(B_\perp)$ curves measured at fixed $B_\parallel$, is by looking at the conductance at $B_\perp = 0$ as function of $B_\parallel$. Specifically, the theory for spin-induced dephasing predicts that[10]

$$\sigma(B_\perp = 0, 0) - \sigma(B_\perp = 0, B_\parallel) = \frac{e^2}{2\pi^2\hbar}\,\ln\left(\frac{\tau_\phi(0)}{\tau_\phi(B_\parallel)}\right)$$

$$= \frac{e^2}{2\pi^2\hbar}\,\ln(1 + c\,B_\parallel^2) \tag{7.3}$$

Also in this case, the agreement between theory and data is excellent (see inset in the bottom graph of Fig. 7.3) and the fitting procedure gives values for the parameter c identical to those obtained above. This shows the consistency of our quantitative analysis and confirms once more the validity of the interpretation of the data in terms of spin-induced TRS breaking only.

7.6   The spin relaxation time: $\tau_s(B_\parallel)$

Finally, Fig. 7.5 shows the behavior of the measured spin relaxation time as function of $B_\parallel$ for different densities and different strength of SOI interaction (samples 1 and 2). In all cases, the measured spin relaxation time increases quadratically with increasing the applied in-plane field. This directly shows that the presence of an in-plane field reduces spin-randomization. The increase in $\tau_s(B_\parallel)$ is more pronounced for a small strength of the SOI interaction and for short values of the elastic scattering time τ, i.e., for long Dyakonov-Perel spin-relaxation times $\tau_s(0)$. This is because the Zeeman energy $E_Z = g\mu B_\parallel$, that drives the alignment of the electron spin along $B_\parallel$, competes with the characteristic energy associated to the spin-randomization $E_{SOI} \equiv \hbar/\tau_s(0)$. Note that the opposite behavior, i.e., τ_s decreasing with increasing B, has been recently observed in systems with different spin-relaxation mechanisms [16].

A quantitative analysis of the data requires a comparison with theory. For the case of a magnetic field normal to the conduction plane, extensive theoretical analysis exists [15]. For the case of an in-plane field, in which the behavior of τ_s is determined by the Zeeman coupling and not by orbital effects, only the relaxation time of the z-component of the spin has been calculated as a function of $B_\parallel$ [17]. When the Zeeman energy E_Z is much smaller than $E_{SOI} \equiv \hbar/\tau_s(0)$, this quantity is given by

$$\frac{\tau_{s_z}(B_\parallel)}{\tau_{s_z}(0)} \simeq 1 + \frac{1}{2}\,(\,\kappa\,g_\parallel^*\mu_B B_\parallel\,\tau_s(0)/\hbar\,)^2 \;=\; 1 + \frac{1}{2}\,(\kappa\,E_Z/E_{SOI})^2 \qquad (7.4)$$

Although theoretical predictions for $\tau_{s_x}(B_\parallel)$ and $\tau_{s_y}(B_\parallel)$ are not available, we expect $\tau_{s_x}(B_\parallel)/\tau_{s_x}(0)$ and $\tau_{s_y}(B_\parallel)/\tau_{s_y}(0)$ to exhibit the same functional dependence as $\tau_{s_z}(B_\parallel)/\tau_{s_z}(0)$ as long as $E_Z \ll E_{SOI}$ and kT. This allows us to compare the measured $\tau_s(B_\parallel)/\tau_s(0)$ to Eq. 7.4. All the quantities that appear in Eq. 7.4 are known from the previous analysis, and we add a parameter κ to achieve best fits to the data (theory [17] predicts $\kappa = 1$ in Eq. 7.4). Figure 7.5 shows that in all cases good agreement is obtained with $\kappa \simeq 1$ (continuous lines). We conclude that the qualitative behavior of the spin-relaxation time as a function of $B_\parallel$, τ and Δ (or, equivalently, $\tau_s(0)$) is the one expected, and that, within a small correction factor, our results are in quantitative agreement with theoretical predictions.

In view of the quantitative agreement between theory and data obtained throughout this work, it is worth considering the origin of the small correction factor κ. $\kappa \neq 1$ may originate from the limited accuracy with which the quantities in Eq. 7.4 are determined. The largest uncertainty comes from $g_\parallel^*$ and is
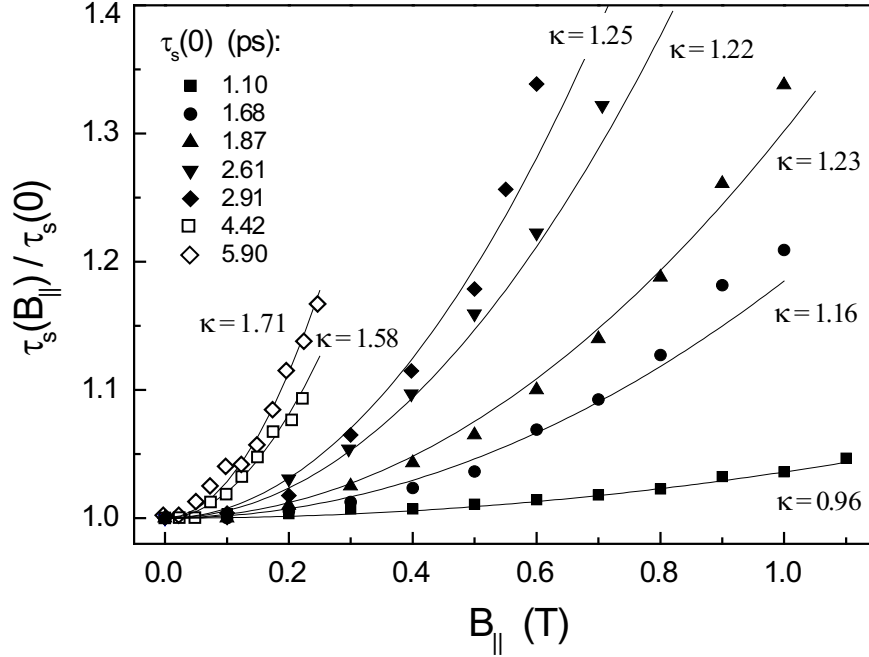
Figure 7.5: The symbols represent τ_s as function of $B_\parallel$, as extracted from the analysis of the magnetoconductance of sample 1 (open symbols) and sample 2 (filled symbols). Each set of symbols corresponds to a different value of the Dyakonov-Perel spin-relaxation time $\tau_s(0)$, with $1/\tau_s(0) = \Delta^2\tau/2\hbar^2$ (controlled by changing the gate voltage). The solid lines are best fits to the theory (Eq. 7.4), with κ as an added parameter (see text). Note that the symbol code used in this figure for τ_s corresponds to that used in Fig. 7.4 for τ_ϕ.

approximately 10%. An additional possibility is the $B_\parallel$-induced anisotropy of the in-plane spin relaxation times, i.e., $B_\parallel$ breaks spin-rotational symmetry in the 2D plane. Although this anisotropy is expected to be small for $E_Z \ll E_{SOI}$ and k_BT, as mentioned before, it may result in a deviation from $\kappa = 1$. Finally, for sample 1 with the weakest Rashba SOI, the Dresselhaus term may not be entirely negligible [18].

7.7 Conclusions

In conclusion, we have investigated how the competition between Rashba SOI and Zeeman coupling affects the orbital and spin dynamics of electrons in 2D electron gases. We have found that the the partial alignment of the electron spin

along an applied in-plane magnetic field results in a spin-induced breaking of Time Reversal Symmetry (i.e., in dephasing of time-reversed waves), and in an increase of the spin-relaxation time (which is approximately quadratic with E_Z/E_{SOI}). Our detailed quantitative analysis demonstrates the validity of recently developed theories, and also provides indications to the limits of their validity.

References

[1] S.A. Wolf, D.D. Awschalom, R.A. Buhrman, J.M. Daughton, S. von Molnar, M.L. Roukes, A.Y. Chtchelkanova, and D.M. Treger, Science **294**, 1488 (2001); D.D. Awschalom, D. Loss, and N. Samarth, *Semiconductor Spintronics and Quantum Computation* (Spinger-Verlag, Berlin, 2002); I. Zutic, J. Fabian, and S. Das Sarma, Rev. Mod. Phys. **76**, 323-410 (2004)

[2] I.L. Aleiner and V.I. Falko, Phys. Rev. Lett. **87**, 256801 (2001); R. Raimondi, M. Leadbeater, P. Schwab, E. Caroti, and C. Castellani, Phys. Rev. B, **64**, 235110 (2001); B.I. Halperin, A. Stern, Y. Oreg, J.N.H.J. Cremers, J.A. Folk, and C.M. Marcus, Phys. Rev. Lett., **86**, 2106 (2001); M. Governale, Phys. Rev. Lett. **89**, 206802 (2002); J.H. Cremers, P.W. Brouwer, and V.I. Falko, Phys. Rev. B **68**, 125329 (2003); J. Schliemann and D. Loss, Phys. Rev. B **68**, 165311 (2003); K. Held, E. Eisenberg and B.L. Altshuler, Phys. Rev. Lett. **90**, 106802 (2003)

[3] D.M. Zumbuhl, J.B. Miller, C.M. Marcus, K. Campman, and A.C. Gossard, Phys. Rev. Lett. **89**, 276803 (2002); G.M. Minkov, A.V. Germanenko, O.E. Rut, A.A. Sherstobitov, L.E. Golub, B.N. Zvonkov, and M. Willander, cond-mat/0312074 (2003)

[4] T. Koga, J. Nitta, T. Akazaki, and H. Takayanagi, Phys. Rev. Lett. **89**, 46801 (2002)

[5] J. Nitta, T. Akazaki, H. Takayanagi, and T. Enoki, Phys. Rev. Lett. **78**, 1335 (1997); G. Engels, J. Lange, T. Schapers, and H. Luth, Phys. Rev. B **55**, R1958 (1997); T. Schapers, J. Appenzeller, H. Hardtdegen, and H. Luth, J. Appl. Phys. **83**, 4324 (1998); D. Grundler, Phys. Rev. Lett. **84** 6074 (2000)

[6] Yu. A. Bychkov and E.I. Rashba, J. Phys. C **17**, 6093 (1984)

[7] Experimentally, the value of $B_\perp$ is obtained from the measurement of the Hall voltage performed simultaneously to the measurement of the longitudinal conductivity. In the presence of a large $B_\parallel$, this automatically takes into account any small misalignment of the sample.

[8] For an anaysis of WAL at $B_\parallel = 0$ see, e.g., W. Knap, C. Skierbiszewski, A. Zduniak, E. Litwin-Staszewska, D. Bertho, F. Kobbi, J. L. Robert, G. E. Pikus, F. G. Pikus, S. V. Iordanskii, V. Mosser, K. Zekentes, and Yu. B. Lyanda-Geller, Phys. Rev. B **53**, 3912 (1996); T. Hassenkam, S. Pedersen, K. Baklanov, A. Kristensen, C. B. Sorensen, P. E. Lindelof, F. G. Pikus, and G. E. Pikus, Phys. Rev. B **55**, 9298 (1997); A. Zduniak, M. I. Dyakonov, and W. Knap, Phys. Rev. B **56**, 1996 (1997)

[9] H. Mathur and H.U. Baranger, Phys. Rev. B **64**, 235325 (2001); J.S. Meyer, A. Altland, and B.L. Altshuler, Phys. Rev. Lett. **89**, 206601 (2002); V.I. Fal'ko and T. Jungwirth, Phys. Rev. B **65**, R81306 (2002)

[10] A.G. Malshukov, K.A. Chao and M. Willander, Phys. Rev. B **56**, 6436 (1997)

[11] S.V. Iordanskii, Y.B. Lyanda-Geller, and G.E. Pikus, JETP **60**, 206 (1994) (Pis'ma Zh. Eksp. Teor. Fiz. **60**, 199 (1994))

[12] M.I. Dyakonov and V.I. Perel, Sov. Phys. JETP **33**, 1053 (1971); Sov. Phys. Solid State **13**, 3023 (1972)

[13] $\tau_\phi(B_\parallel)$ is the upper cut-off time for interference of time-reversed paths (also denoted as τ_H or $\tau_{B_\parallel}$ in literature (see, e.g., [9, 10])).

[14] R. Winkler, *Spin-Orbit Coupling Effects in Two-Dimenional Electron and Hole Systems* (Springer-Verlag, Berlin, 2003), p. 133

[15] For most recent work see A.A. Burkov and L. Balents, cond-mat/0401398 (2004), and references therein.

[16] J.M. Kikkawa and D.D. Awschalom, Phys. Rev. Lett. **80**, 4313 (1998); R. Hanson, private communication, to appear in Nature.

[17] V.A. Froltsov, Phys. Rev. B **64**, 45311 (2001)

[18] N.S. Averkiev and L.E. Golub, Phys. Rev. B **60**, 15582 (1999)

Chapter 8

Universal spin-induced Time Reversal Symmetry breaking in 2D electron gases with Rashba SOI

We have experimentally studied the spin-induced time reversal symmetry (TRS) breaking as a function of the relative strength of the Zeeman energy (E_Z) and the Rashba spin-orbit interaction energy (E_{SOI}), in InGaAs-based 2D electron gases. We find that the TRS breaking, and hence the associated dephasing time $\tau_\phi(B)$, *saturates* when E_Z becomes comparable to E_{SOI}. Moreover, we show that the spin-induced TRS breaking mechanism is a *universal function* of the ratio E_Z/E_{SOI}, within the experimental accuracy.

8.1 Introduction

The spin dynamics in solid state systems is commonly determined by the competition between two energy scales; the Zeeman energy and spin-orbit interaction (SOI) energy. If the Zeeman energy (E_Z) is dominant, the spin is always aligned with the applied magnetic field. In contrast, if the spin-orbit interaction is dominant, the spin and orbital dynamics are coupled, and elastic scattering therefore randomizes the spin precession axis. This results in a finite spin relaxation time $\tau_s(0)$ [1]. Hence, the "control parameter" for the spin dynamics in diffusive systems is the ratio E_Z/E_{SOI}, where $E_{SOI} \equiv \hbar/\tau_s(0)$. Consequently, many proposals and physical phenomena in the field of spintronics depend on the ratio of these two energy scales [2, 3, 4].

An example where the spin dynamics, and therefore the ratio E_Z/E_{SOI}, plays an important role is in phase-coherent transport: quantum interference is qualitatively different for $E_Z/E_{SOI} \ll 1$ and $E_Z/E_{SOI} \gg 1$. For $E_Z/E_{SOI} \to \infty$ the spin dynamics does not depend on the orbital motion of the electrons (Fig. 8.1a). The spin is a good quantum number and the interference takes place within each spin-subband separately. For $E_Z/E_{SOI} \ll 1$, the spin is not a conserved quantity, and the spin randomly precesses during the orbital motion (Fig. 8.1b). This leads to mixing of the spin subbands in the interference process (resulting in weak-anti localization [5, 6]). Increasing the ratio E_Z/E_{SOI} leads therefore to a crossover between two conceptually different physical conditions.

In the limit that $E_Z/E_{SOI} \ll 1$, it was recently shown theoretically [7] and experimentally [8, 9] that increasing the ratio E_Z/E_{SOI} from 0 to a finite value ($\ll 1$), results in dephasing of time-reversed paths, i.e. it induces Time Reversal Symmetry (TRS) breaking (see Chapter 7). The effect of the interplay between Zeeman and Rashba SOI on quantum interference is therefore quite similar to a small perpendicular magnetic field (i.e. a magnetic flux); they both introduce an upper time-scale for interference, which is shorter than the inelastic scattering time [10]. We denote this upper time-scale due to the interplay between Zeeman and Rashba SOI by $\tau_\phi(B_\parallel)$.

In this Chapter we investigate experimentally the TRS breaking, due to the competition between Zeeman coupling and Rashba SOI [11], for the whole range of E_Z/E_{SOI}, i.e up to $E_Z/E_{SOI} \gg 1$. We demonstrate that the spin-induced TRS breaking, and hence the associated dephasing time $\tau_\phi(B_\parallel)$, *saturates* when $E_Z/E_{SOI} \approx 1$, i.e. when the spin becomes aligned with the external magnetic field. The saturation value of the dephasing time $\tau_\phi(B_\parallel)$ is found to depend exclusively on the spin relaxation time $\tau_s(0)$. Moreover, we show that the quantity $\tau_s(0)/\tau_\phi(B_\parallel)$ is a *universal function* of E_Z/E_{SOI}, i.e. it is independent of any
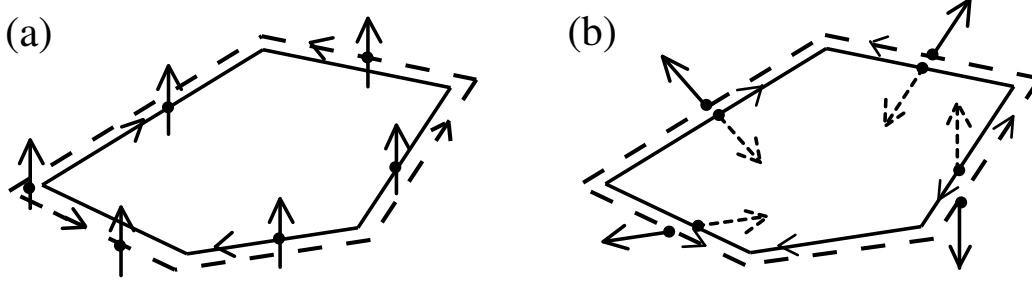
Figure 8.1: Schematic illustration of the relevant time-reversed trajectories contributing to weak-(anti)localization for the case of negligible Rashba SOI (a; $E_Z/E_{SOI} \rightarrow \infty$) and strong Rashba SOI (b; $E_Z/E_{SOI} \ll 1$). If Rashba SOI is negligible the spin remains parallel to itself and interference takes place for each spin-subband separately. If Rashba SOI is strong, the spin dynamics has to be taken into account. This changes the nature of time-reversed trajectories and makes them sensitive to the presence of a magnetic field applied parallel to the plane of the two-dimensional electron gas.

details of the quantum well, such as the electron density, elastic scattering time and Rashba spin-split energy Δ. All these conclusions are based on the detailed quantitative analysis of the magnetoconductance as a function of perpendicular and parallel magnetic field.

8.2 Samples and experimental procedure

In our investigation we have used the same samples as in Chapter 7, and we will refer to the three Hall bars with different Rashba SOI strength again as to samples 1, 2, and 3, respectively. These measurements have also been performed at T = 1.6 K.

Experimentally, the values of $\tau_\phi(B_\parallel)$, which quantify the TRS breaking at different values of E_Z/E_{SOI}, are obtained again from the magnetoconductance as a function of $B_\perp$, at different fixed values of $B_\parallel$ (i.e. E_Z). Specifically, from the quantitative analysis of the line-shape of the resulting magnetoconductance curves $\sigma(B_\perp)$, the values of $\tau_\phi(B_\parallel)$ can be extracted. For all details of extracting $\tau_\phi(B_\parallel)$ we refer the reader to Chapter 7. Here we recall that we use the theory of Iordanskii, Lyanda-Geller and Pikus (ILP) [6], in which $\tau_\phi(B_\parallel)$ and the spin relaxation time $\tau_s(B_\parallel)$ are the only free parameters [13].

8.3   Typical measurements

The upper graph in Figure 8.2 shows an example of the measured magnetocon-ductance curves $\sigma(B_\perp)$ at different values of $B_\parallel$ for sample 3. The bottom graph shows a zoom-in on the data (open circles), together with the best fit to the ILP theory (the continuous lines superimposed on the data). We find very good agreement between data and theory for all values of $B_\parallel$, or equivalently, for all values of the ratio E_Z/E_{SOI}. This kind of analysis has been performed for all samples, and for different values of the electron density, elastic scattering time and SOI strength [14].

Note that for $E_Z/E_{SOI} \geq 1$ the weak-antilocalization is fully suppressed (see Fig. 8.2). Therefore, in the limit that $E_Z/E_{SOI} \geq 1$, $\tau_\phi(B_\parallel)$ is the only free parameter in the ILP model to fit the data, and can be determined with great accuracy. Only in the narrow region where $E_Z \approx E_{SOI}$, the value of $\tau_\phi(B_\parallel)$ is possibly determined with somewhat less accuracy, due to potential $B_\parallel$-induced anisotropies in the spin relaxation time.

8.4   The phase-coherence time: $\tau_\phi(B_\parallel)$

In Fig. 8.3 we first plot the extracted values of $\tau_\phi(B_\parallel)$ as a function of $B_\parallel$ (or more precise, $B_\parallel^2$), since this is the experimentally applied parameter. For each value of E_{SOI}, we find the same qualitative behavior of the $\tau_\phi(B_\parallel)$-curve (results from all three samples are shown). For small values of $B_\parallel^2$, the slope $\partial(1/\tau_\phi(B_\parallel))/\partial B_\parallel^2$ (hereafter called "dephasing-slope") is large, and depends strongly on the value of E_{SOI}. For large values of $B_\parallel^2$ (or E_Z^2) the dephasing-slope is found to be much smaller. In both limits, we find that the dephasing-slope is constant, i.e. $1/\tau_\phi(B_\parallel) \propto B_\parallel^2$. The value of $B_\parallel^2$ (or E_Z^2) at which the crossover occurs is larger for larger values of E_{SOI}. Anticipating, the crossover occurs when $E_Z/E_{SOI} \approx 1$ (see Fig. 8.4).

The large dephasing-slope for $E_Z/E_{SOI} \ll 1$ is due to the competition be-tween Zeeman coupling and Rashba SOI (see Chapter 7). In contrast, the small dephasing-slope in the high field limit can be attributed to the coupling of $B_\parallel$ to the *orbital motion* of the electrons. Hence, Fig. 8.3 suggests that the spin-induced dephasing of time reversed waves - i.e. the spin-induced TRS breaking - *saturates*.
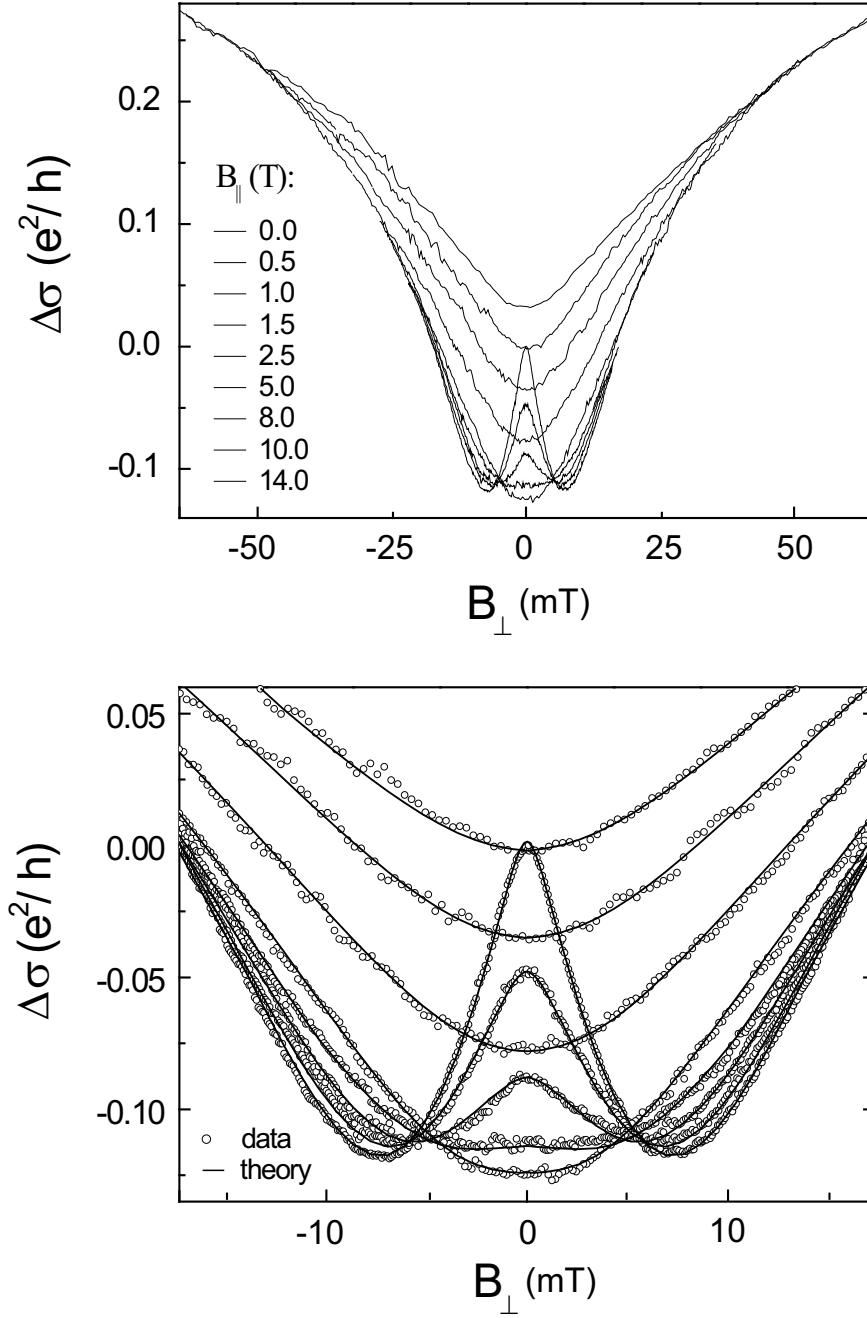
Figure 8.2: *Upper graph:* The magnetoconductance $\sigma(B_\perp)$ of sample 3, measured at different values of E_Z/E_{SOI}: 0, 0.23, 0.46, 0.70, 1.16, 2.33, 3.72, 4.66 and 6.53, corresponding to $B_\parallel = 0$, 0.5, 1, 1.5, 2.5, 5, 8, 10 and 14T. *Bottom graph:* A zoom-in on the data, together with the best fits to the ILP theory (solid lines). From these fits we obtain $\tau_\phi(B_\parallel)$ and $\tau_s(B_\parallel)$, and hence also $E_{SOI} \equiv \hbar/\tau_s(0)$.
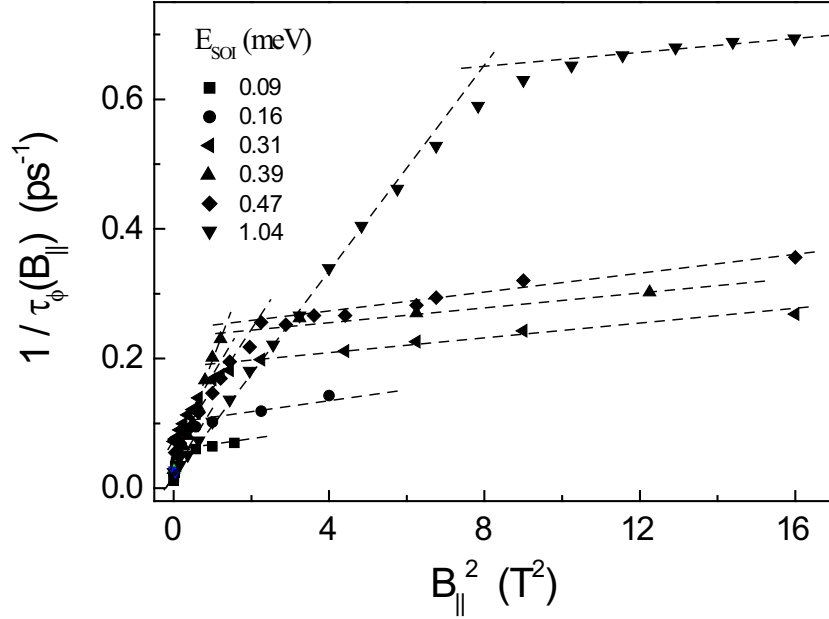
Figure 8.3: Extracted values of the dephasing rate $1/\tau_\phi(B_\parallel)$ as a function of $B_\parallel^2$. The different symbols correspond to different values of E_{SOI} [16] (results from all three samples are shown). The solid lines act as a guide to the eye.

8.5   Universality of spin-induced TRS breaking

To show the spin-induced part of the measured dephasing rate $1/\tau_\phi(B_\parallel)$, we subtract the contribution due to inelastic scattering ($\equiv 1/\tau_\phi(0)$), and denote the spin-induced dephasing rate by $\Gamma_\phi^s(B_\parallel)$, with $\Gamma_\phi^s(B_\parallel) = 1/\tau_\phi(B_\parallel) - 1/\tau_\phi(0)$. For $E_Z/E_{SOI} \ll 1$ the spin-induced dephasing rate of time-reversed waves $\Gamma_\phi^s(B_\parallel)$ is given by [7] $\tau_s(0)\,\Gamma_\phi^s(B_\parallel) = (E_Z/E_{SOI})^2$. In Fig. 8.4 we plot $\tau_s(0)\,\Gamma_\phi^s(B_\parallel)$ for the whole measured range of E_Z/E_{SOI} [17]. For all samples, and all different values of electron density, elastic scattering time, Rashba strength, and E_{SOI}, the quantity $\tau_s(0)\,\Gamma_\phi^s(B_\parallel)$ collapses to nearly the same curve (the combined error in the determination of $\tau_s(0)$ and $\Gamma_\phi^s(B_\parallel)$ is typically 10%). We therefore conclude that the spin-induced TRS breaking in quantum wells with Rashba SOI (or more precisely $\tau_s(0)\,\Gamma_\phi^s(B_\parallel)$) is a *universal function* of E_Z/E_{SOI}, within the experimental accuracy.

The spin-induced TRS breaking (or $\Gamma_\phi^s(B_\parallel)$) saturates when $E_Z/E_{SOI} \approx 1$. For this strength of the Zeeman coupling the spins start becoming parallel or anti- parallel with $B_\parallel$. This conclusion is consistent with the observation that for
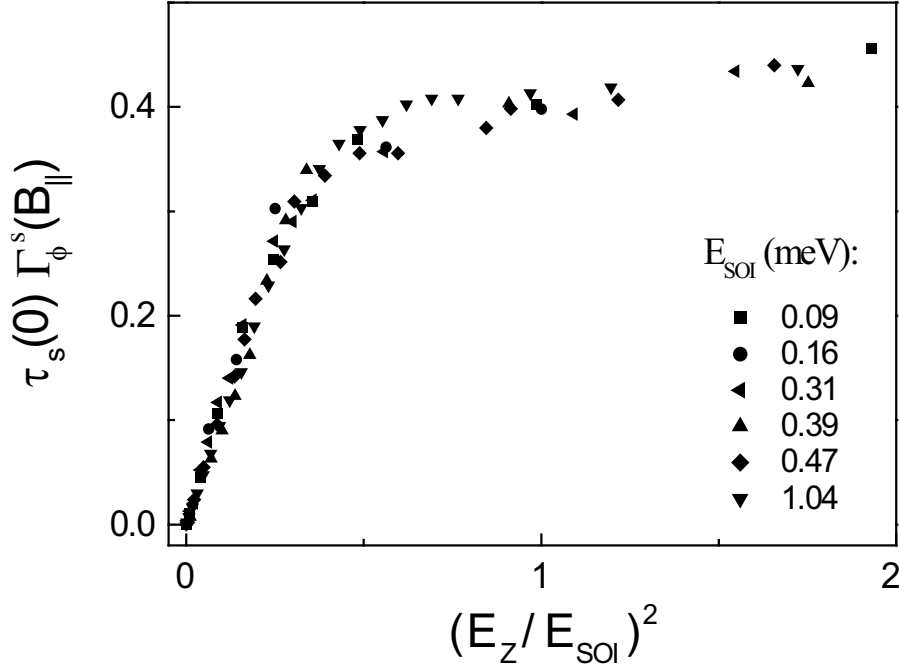
Figure 8.4: The spin-induced dephasing rate $\Gamma_\phi^s(B_\parallel)$ multiplied by $\tau_s(0)$, as a function of $(E_Z/E_{SOI})^2$, with $\Gamma_\phi^s(B_\parallel) = 1/\tau_\phi(B_\parallel) - 1/\tau_\phi(0)$, and $\tau_\phi(0)$ is the inelastic scattering time. Results from all three samples are shown, illustrating that irrespective of sample, electron density, SOI strength, etc., the data collapse on nearly a single curve.

$E_Z/E_{SOI} \approx 1$ the weak anti-localization is just fully suppressed (see Fig. 8.2): when the spins become aligned with $B_\parallel$, only weak-localization is expected, since conceptually this situation is identical to the case where only a small perpendicular field is present, and the spins are aligned with $B_\perp$.

Currently, there are no theoretical predictions for the behavior of $\tau_s(0)\,\Gamma_\phi^s(B_\parallel)$ when E_Z/E_{SOI} is not small, i.e. when the Zeeman coupling is not a small perturbation. It has only been predicted, for specific cases, that the magnetoconductance $\sigma(B_\parallel)$ saturates when $E_Z/E_{SOI} \gg 1$, indicating a saturation of $\tau_s(0)\,\Gamma_\phi^s(B_\parallel)$ [18]. However, the corresponding behavior of $\tau_s(0)\,\Gamma_\phi^s(B_\parallel)$ - in particular its universal character - had not been recognized so far.

We understand the saturation of $\Gamma_\phi^s(B_\parallel)$ for $E_Z/E_{SOI} \gg 1$, and the dependence of the saturation value of $\Gamma_\phi^s(B_\parallel)$ on spin relaxation time $\tau_s(0)$, in the following intuitive way. Imagine first that the Zeeman splitting is large and SOI is absent. At the Fermi energy, the spin-split subbands are then well separated in k-space, and are fully decoupled. In that case each subband contributes sepa-

rately to the interference, and the upper time-scale for interference is the inelastic scattering time, independent of the size of the Zeeman splitting. In the presence of SOI, the spin subbands become weakly coupled, i.e. a particle can be scattered from one spin subband to the other (flip its spin). Imagine there is a spin-flip center at a certain position along the path. Both time-reversed waves will then flip their spin at that position, and hence at different times in general. The waves spend therefore different amounts of time in each spin subband before they interfere, and obtain a large phase difference, since $k_{F,\uparrow} - k_{F,\downarrow}$ is large (large Zeeman splitting). This implies that waves do no longer contribute to the interference (on average) if a spin-flip event takes place along the path. The upper time-scale for quantum interference is therefore reduced to (roughly) the spin relaxation time $\tau_s(0)$, independent of the Zeeman splitting, as long as $k_{F,\uparrow} - k_{F,\downarrow}$ is large enough. This simple picture is in qualitative agreement with our experiments.

8.6   TRS breaking by orbital coupling

Finally, we focus in more detail on the remaining small, but finite, dephasing-slope for $E_Z/E_{SOI} \gg 1$ (see Figs. 8.3 and 8.4). To show the remaining dephasing rate for $E_Z/E_{SOI} \gg 1$ most clearly, we subtract the spin-induced dephasing rate in this limit - which equals the saturation value $1/\tau_\phi(E_Z/E_{SOI} = 1)$ - and denote the resulting dephasing rate by $\Gamma_\phi^{orb}(B_\parallel)$. Fig. 8.5 shows the extracted values of $\Gamma_\phi^{orb}(B_\parallel) = 1/\tau_\phi(B_\parallel) - 1/\tau_\phi(E_Z/E_{SOI} = 1)$ for sample 1 (weakest SOI), for different values of the electron density [19] (Note that the $B_\parallel^2$-field scale in this graph is much larger than in Figs. 8.3 and 8.4, i.e. $E_Z/E_{SOI} \gg 1$). We find that the dephasing slope is larger for larger values of the electron density. In particular, we find that the remaining dephasing slope scales about linearly with the Fermi velocity (see inset).

The finite thickness of the quantum well makes that $B_\parallel$ does not only couple to the electron spin (Zeeman coupling), but also to its *orbital motion*. It has been shown that this orbital coupling can also break TRS, via various mechanisms [21, 22]. These mechanisms depend on the specific (non-universal) details of the quantum well, such as surface roughness, z-dependence of the scattering potential in the 2DEG, and the asymmetry of the confining potential. The linear dependence of $\Gamma_\phi^{orb}(B_\parallel)$ (or $1/\tau_\phi(B_\parallel)$) on $B_\parallel^2$, together with the linear dependence of the dephasing-slope on v_F, indicates that the (small) remaining slope for $E_Z/E_{SOI} \gg 1$ is caused by surface roughness [21]. The resulting dephasing-slope is given by
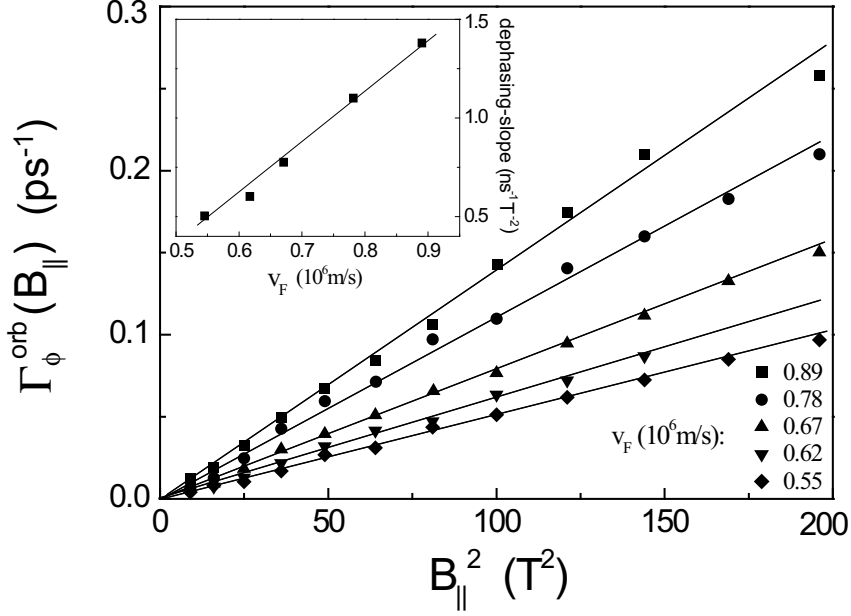
Figure 8.5: The measured values of $\Gamma_\phi^{orb}(B_\parallel) = 1/\tau_\phi(B_\parallel) - 1/\tau_\phi(E_Z/E_{SOI} = 1)$ in sample 1, for various values of the electron density (i.e. v_F). The dephasing-slope, $\partial(1/\tau_\phi(B_\parallel))/\partial B_\parallel^2 = \partial\Gamma_\phi^{orb}(B_\parallel)/\partial B_\parallel^2$, depends about linearly on v_F (see inset). This indicates that surface roughness is the main orbital TRS breaking mechanism. Note that the $B_\parallel^2$-scale is much larger than in Figs. 8.3 and 8.4.

$$\frac{\partial(1/\tau_\phi(B_\parallel))}{\partial B_\parallel^2} \approx \sqrt{\pi}\, e^2\, d^2\, L\, v_F\, /\, \hbar^2 \tag{8.1}$$

where d is the mean roughness height and L is the correlation length of the roughness. For our quantum well we find $d^2 L \approx 0.4 \; nm^3$, which is a small value in comparison to other reports [9].

In general, the orbital mechanism will break the universality of the experimentally measured TRS breaking in systems with SOI, since it adds to the (universal) spin-induced TRS breaking mechanism. In our samples, the orbital TRS mechanism is very small an hence unimportant, so it affects the universality only minorly. This allows us to observe the universal behavior of the spin-induced TRS breaking for all values of the ratio E_Z/E_{SOI}.

8.7   Conclusions

In conclusion, we have demonstrated that the TRS breaking rate $\Gamma_\phi(B_\parallel)$, caused by the competition between Rashba and Zeeman, saturates when $E_Z \approx E_{SOI}$. This is because for $E_Z \geq E_{SOI}$, two Fermi surfaces start being formed with well-defined spin direction, pointing either parallel or anti-parallel to $B_\parallel$. Moreover, we have shown that the scaled dephasing rate, $\tau_s(0)\Gamma_\phi(B_\parallel)$, is a universal function of the ratio E_Z/E_{SOI}, within the experimental accuracy. Finally, we have shown that this universality is broken by the coupling of the magnetic field to the orbital motion of the electrons.

References

[1] M.I. Dyakonov and V.I. Perel, Sov. Phys. JETP **33**, 1053 (1971); Sov. Phys. Solid State **13**, 3023 (1972)

[2] I.L. Aleiner and V.I. Falko, Phys. Rev. Lett. **87**, 256801 (2001); M. Governale, Phys. Rev. Lett. **89**, 206802 (2002); D.M. Zumbuhl, J.B. Miller, C.M. Marcus, K. Campman, and A.C. Gossard, Phys. Rev. Lett. **89**, 276803 (2002); V. M. Apalkov and M.E. Raikh, Phys. Rev. Lett. **89**, 096805 (2002); I. Zutic, J. Fabian, and S. Das Sarma, Rev. Mod. Phys. **76**, 323-410 (2004).

[3] V.A. Froltsov, Phys. Rev. B **64**, 45311 (2001); R. Raimondi, M. Leadbeater, P. Schwab, E. Caroti, and C. Castellani, Phys. Rev. B, **64**, 235110 (2001); Y. Yu, Y. Wen, J. Li, Z. Su, and S.T. Chui, Phys. Rev. B **69**, 153307 (2004); S.Q. Shen, M. Ma, X.C. Xie, and F.C. Zhang, Phys. Rev. Lett. **92**, 256603 (2004); D. Frustaglia and K. Richter Phys. Rev. B **69**, 235310 (2004)

[4] J. Nitta, F.E. Meijer, and H. Takayanagi, Appl. Phys. Lett. **75**, 695 (1999); B.I. Halperin, A. Stern, Y. Oreg, J.N.H.J. Cremers, J.A. Folk, and C.M. Marcus, Phys. Rev. Lett., **86**, 2106 (2001); J.N.H.J Cremers, P.W. Brouwer, and V.I. Falko, Phys. Rev. B **68**, 125329 (2003); F.E. Meijer, A.F. Morpurgo, T.M. Klapwijk, T. Koga, and J. Nitta, Phys. Rev. B **69**, 35308 (2004)

[5] See, e.g., G. Bergmann, Solid State Comm. **42**, 815 (1982)

[6] S.V. Iordanskii, Y.B. Lyanda-Geller, and G.E. Pikus, JETP Lett. **60**, 206 (1994) (Pis'ma Zh. Eksp. Teor. Fiz. **60**, 199 (1994))

[7] A.G. Malshukov, K.A. Chao and M. Willander, Phys. Rev. B **56**, 6436 (1997)

[8] F.E. Meijer, A.F. Morpurgo, T.M. Klapwijk, T. Koga and J. Nitta, Phys. Rev. B **70**, 201307(R) (2004)

[9] G.M. Minkov, A.V. Germanenko, O.E. Rut, A.A. Sherstobitov, L.E. Golub, B.N. Zvonkov, and M. Willander, Phys. Rev. B **70**, 155323 (2004)

[10] For a perpendicular field this upper time-scale is often denoted τ_B, and is given by $\tau_B = h/2eBD$, with D is the diffusion constant.

[11] E.I. Rashba, Fiz. Tverd. Tela (Leningrad) **2**, 1224 (1960) [Sov. Phys. Solid State **2**, 1109 (1960)]; Yu.A. Bychkov and E.I. Rashba, J. Phys. C **17**, 6093 (1984)

[12] T. Koga, J. Nitta, T. Akazaki, and H. Takayanagi, Phys. Rev. Lett. **89**, 46801 (2002)

[13] In the ILP model, the magnetoconductance is assumed to be determined by 2D interference, i.e $\sqrt{D\tau_\phi(B_\parallel)/3}$ must be much larger than the sample thickness. This condition is satisfied for all values of $B_\parallel$ in our measurements.

[14] Notice that due to the relatively large electron density and small effective mass ($m^* \approx 0.041 m_0$) the electron gas is far from being spin-polarized, even at $B_\parallel = 14$T. Also, due to the large SOI strength in our samples, together with $r_s \ll 1$, the magnetoconductance is essentially only determined by interference corrections, and not by $B_\parallel$-induced electron-electron interaction effects[15]. We do find a small quadratic enhancement of the Drude resistivity with $B_\parallel$ ($< 4\%$ at $B_\parallel = 14$T), the discussion of which is beyond the scope of the present paper.

[15] For a recent review see I.V. Gornyi and A.D. Mirlin, Phys. Rev. B **69**, 45313 (2004)

[16] The Rashba SOI strength Δ (and $E_{SOI} \equiv \hbar/\tau_s(0) = \Delta^2\tau/2\hbar$) can be modified by a gate voltage. See e.g. J. Nitta, T. Akazaki, H. Takayanagi, and T. Enoki, Phys. Rev. Lett. **78**, 1335 (1997); G. Engels, J. Lange, T. Schäpers, and H. Lüth, Phys. Rev. B **55**, R1958 (1997); T. Schäpers, J. Appenzeller, H. Hardtdegen, and H. Lüth, J. Appl. Phys. **83**, 4324 (1998); D. Grundler, Phys. Rev. Lett. **84** 6074 (2000)

[17] The g-factor is obtained experimentally from the TRS breaking for $E_Z/E_{SOI} \ll 1$, as shown in [8].

[18] A.G. Malshukov, V.A. Froltsov, and K.A. Chao, Phys. Rev. B **59**, 5702 (1999)

[19] In order to obtain the highest possible accuracy in determining $\tau_\phi(B_\parallel)$, as it is needed to determine the weak $B_\parallel$-dependence for $E_Z/E_{SOI} \gg 1$, we have (also) used the theory of Kawabata and Dyakonov[20] to extract $\tau_\phi(B_\parallel)$. Note

that this theory can not be used for $E_Z/E_{SOI} \ll 1$, as weak-antilocalization due to Rashba SOI is neglected.

[20] A. Kawabata, J. Phys. Soc. Jpn. **53**, 3540 (1984); M.I. Dyakonov, Solid State Comm. **92**, 711 (1994)

[21] H. Mathur and H.U. Baranger, Phys. Rev. B **64**, 235325 (2001);

[22] J.S. Meyer, A. Altland, and B.L. Altshuler, Phys. Rev. Lett. **89**, 206601 (2002); V.I. Fal'ko and T. Jungwirth, Phys. Rev. B **65**, R81306 (2002)

Summary

In modern semiconductor devices, only the *charge* of electrons is being utilized for the manipulation and transport of information. The spin degree of freedom of the electrons has not been exploited in any commercial semiconductor application so far. People in the field of Spintronics are trying to find new or improved functionalities and applications that are based on the *spin* of electrons, instead of - or in addition to - its charge. Some of these new ideas are based on the binary nature of the electron spin, which makes that it could serve as an elementary digital bit. When the spin state can be transported and manipulated in space and time, the spin could be used for new calculation schemes, for example. In addition, it has been predicted that the motion of electrons through materials can be affected by acting on their spin state. Hence, the spin could potentially function as a "knob" for tuning the conductivity of electrons.

From the above it follows that it is important to understand mechanisms that allow to manipulate the spin dynamics (i.e. the spin state of electrons). The best-known mechanism to affect the spin dynamics is by an external magnetic field, i.e., via Zeeman coupling to the spin. Another potentially important mechanism is Rashba spin-orbit interaction (SOI). The interesting and distinguishing feature of Rashba SOI is, that it can be tuned by *electrostatic* means. This might make it easier to control the spin dynamics on very small length scales, in comparison to Zeeman coupling. Rashba SOI is also known, however, to be the main cause of spin relaxation in many 2D electron systems, thereby destroying any information that is encrypted on the spin. For the field of Spintronics it is therefore important to understand the effects of Rashba SOI, and the interplay between Rashba SOI and Zeeman coupling, on electron transport and on the spin dynamics.

In this Thesis we have studied partly theoretically and partly experimentally the influence of Rashba SOI on low temperature electron transport in mesoscopic (phase-coherent) systems, such as Hall bars and ring structures. In addition, we have experimentally investigated how the competition between Rashba SOI and Zeeman coupling affects the spin dynamics in 2D electron gases, and if/how information about the resulting spin dynamics, such as the spin-relaxation time,

can be obtained from "simple" transport measurements. Finally, we have studied the effect of the interplay between Rashba SOI and Zeeman coupling on the breaking of time reversal symmetry in 2D electron gases.

Specifically, in the first part of the Thesis we have described in detail the procedure to obtain the correct Hamiltonian of electrons moving on a one-dimensional ring, in the presence of Rashba SOI and Zeeman coupling. The subtlety of this seemingly trivial problem was not fully appreciated before, and has led to some ambiguities and errors in the literature. We have described the formally correct procedure to project the Hamiltonian defined on the Hilbert space in two dimensions (r, ϕ), on a restricted Hilbert subspace spanned by a complete set of spinors that are only a function of the ϕ-coordinate.

Using this Hamiltonian, we have subsequently calculated the phase-coherent transport properties (i.e. the conductance) of the 1-dimensional ring, as a function of the Rashba SOI strength α. We have shown that Rashba SOI induces a spin-dependent phase-shift in the wavefunction, which results in a modification of the interference pattern, and hence affects the conductance of the ring. In particular, we have demonstrated that the conductance of the ring shows quasi-periodic oscillations as a function of the Rashba strength α. Since the value of α can in practice be controlled by applying a gate voltage, we have proposed to utilize a ring structure that is uniformly covered by a gate electrode as a (spin-based) conductance modulator, or spin-interference device.

The above mentioned spin-induced phase shift is known as the geometrical Aharonov-Casher phase (it is called a *geometrical* phase, because it only depends on the angle that the spin makes while travelling around the ring, and not on the time the traverse takes). This Aharonov-Casher phase is also predicted to affect the Aharonov-Bohm (AB) magnetoconductance oscillations in the ring. Without taking the spin dynamics into account, the period of the AB oscillations corresponds to a flux of h/e through the ring. Including the spin dynamics - causing the Aharonov-Casher phase - results in a beating pattern in the AB oscillations, and hence in deviations from the h/e periodicity. The experimental detection of the effect of the Aharonov-Casher phase in the Fourier transform of the AB oscillations has been the aim of the second part of this Thesis.

We have fabricated a ring structure using an InAs-inserted two-dimensional electron gas with strong Rashba SOI. The Fourier transform of the experimentally measured AB oscillations is found to be dominated by sample-specific features, due to the finite width of the arms of the ring and the quasi-diffusive transport through the ring. This precludes the direct observation of spin-effects in the Fourier transform of a *single* measurement. We have demonstrated that averaging the modulus of the Fourier spectrum $|G(\nu)|$ over measurements taken at

slightly different gate voltage, allows to suppress the sample-specific features in a controllable way. We have found that the h/e peak in the *ensemble averaged* Fourier spectrum $\langle|G(\nu)|\rangle$ shows a clear splitting. By performing a statistical analysis of the ensemble of Fourier spectra, we have demonstrated that the observed splitting in the ensemble averaged Fourier spectrum $\langle|G(\nu)|\rangle$ is statistically significant. Therefore, the observed splitting is *not* a remnant sample-specific feature, but is likely to be a Rashba-induced spin-effect.

In the remaining experimental part of the Thesis we have systematically investigated the influence of the interplay between Rashba SOI and Zeeman coupling on the spin-dynamics and phase-coherent transport in 2D electron gases. For these experiments Hall-bar structures were fabricated out of different InGaAs-based wafers. Each of these wafers was designed to have a different Rashba SOI strength. A gate electrode allowed to control the relevant parameters in the Hall bar, such as the electron mean free path, the Rashba SOI strength, and hence the spin relaxation time τ_s. Zeeman coupling to the spin was achieved by applying a magnetic field in the plane of the 2DEG, thereby causing minimal coupling to the orbital motion of the electrons.

We have used the quantitative analysis of the weak (anti-)localization signal, as a function of perpendicular and in-plane magnetic field, as a new tool to extract the phase-coherence time and the spin relaxation time as a function of both Rashba SOI and Zeeman coupling. From this detailed analysis we have demonstrated that the spin relaxation time increases with increasing Zeeman coupling strength, due to a partial alignment of the electron spin along the applied magnetic field. Hence, the magnetic field is shown to have a stabilizing effect on the spin precession axis. In particular, we have shown that the increase in the spin relaxation time is *only* a function of E_Z/E_{SOI}, with E_Z is the Zeeman energy and $E_{SOI} = \hbar/\tau_s$ is the Rashba SOI related energy scale.

In addition, from the phase-coherent transport measurements, we have also shown that the competition between Rashba SOI and Zeeman coupling results in a dephasing of time-reversed electronic waves. The effect of the interplay between Rashba and Zeeman on quantum interference is therefore found to be similar to a magnetic flux through the 2D electron gas: both cause a breaking of Time Reversal Symmetry (TRS). In contrast to a magnetic flux, however, we have demonstrated that the TRS breaking saturates when $E_Z/E_{SOI} \approx 1$, i.e., when the spins become aligned parallel or anti-parallel with the applied magnetic field. Finally, we have shown that this spin-induced TRS breaking mechanism is a *universal function* of the ratio E_Z/E_{SOI}, within the experimental accuracy.

Delft, April 2005

Samenvatting

In de huidige halfgeleider industrie wordt alléén gebruikt gemaakt van de *lading* van electronen om informatie te manipuleren en te transporteren. The *spin* van electronen wordt tot nu toe niet toegepast in commerciele applicaties die op halfgeleiders zijn gebaseerd. Onderzoekers op het gebied van de Spintronica proberen nieuwe en verbeterde functionalitieten en toepassingen te bedenken die wél zijn gebaseerd op de spin van electronen, in plaats van - of in combinatie met - hun lading. Sommige van deze ideeën zijn geinspireerd op het binaire character van de electron spin, waardoor een spin gebruikt zou kunnen worden als een elementaire digitale bit. Wanneer de spin-toestand kan worden getransporteerd en gecontroleerd in tijd en ruimte, zou de spin bijvoorbeeld toegepast kunnen worden in een nieuw soort informatie technologie. Bovendien is er voorspeld, dat de beweging van electronen door materie beïnvloedt kan worden door hun spin-toestand te beïnvloeden. Daarom zou de spin-toestand eventueel kunnen dienen als een "regelaar" van de geleiding van electronen door een bepaald materiaal.

Uit het bovenstaande volgt dat het belangrijk is om te begrijpen welke mechanismen de spin dynamica (spin-toestand) kunnen controleren/manipuleren. Het bekendste mechanisme is een extern magneetveld, oftewel Zeeman koppeling. Een ander potentieel belangrijk mechanisme is Rashba spin-baan wisselwerking (SBW). Rashba SBW heeft als interesante en onderscheidende eigenschap dat het getuned kan worden door middel van een aangelegde spanning. Dit vergemakkelijkt naar verwachting de controle over de spin-dynamica op nanometer schaal, in vergelijking tot Zeeman koppeling. Het is echter ook bekend dat Rashba SBW de hoofdoorzaak is van spin relaxatie in veel 2D electron systemen. Dit leidt ertoe dat de informatie die in de spin-toestand van electronen is opgeslagen, verloren gaat. Het is dus belangrijk voor de Spintronica om te begrijpen op hoe Rashba SBW, en de competitie tussen Rashba SBW en Zeeman koppeling, het electron transport en de spin dynamica in materialen beïnvloedt.

In dit proefschrift hebben we theoretisch en experimenteel onderzoek gedaan naar de invloed van Rashba SBW op electron transport in mesoscopische (fasecoherente) systemen, zoals Hall- en ring structuren, bij extreem lage tempera-

turen. Daarnaast hebben we onderzocht hoe de competitie tussen Rashba SBW en Zeeman koppeling de spin dynamica in 2D electron gassen beïnvloedt, en of/hoe informatie over bepaalde aspecten van de spin dynamica, zoals de spin-relaxatie tijd, kan worden verkregen uit "simpele" transport metingen. Tenslotte hebben we bestudeerd wat het effect is van de competitie tussen Rashba SBW en Zeeman koppeling op het breken van de tijd-omkeer symmetrie in 2D electron gassen.

Specifiek, in het eerste gedeelte van dit proefschrift hebben we een gedetailleerde beschrijving gegeven van de procedure voor het verkrijgen van de correcte Hamiltoniaan van electronen die bewegen in een 1D ring, onder invloed van Rashba SBW and Zeeman koppeling. The subtiliteit van dit ogenschijnlijk triviale probleem was tot nu niet onder ogen gezien, en heeft geleid tot vaagheden en fouten in de literatuur. Wij hebben de formeel correcte procedure beschreven voor het projecteren van de Hamiltoniaan die gedefinieerd is in de 2D Hilbert ruimte (met parameters r and ϕ), op een 1D Hilbert ruimte, welke slechts functie is van de ϕ-coordinaat.

Gebruik makende van deze Hamiltoniaan, hebben we vervolgens de fase-coherente transport eigenschappen (geleidbaarheid) van de 1D ring berekend, als functie van de Rashba SBW sterkte α. We hebben laten zien dat de Rashba SBW resulteert in een spin-afhankelijke fase verschuiving in de golffunctie, wat leidt tot een verandering in het interferentie patroon en dus in de geleiding van de ring. In het bijzonder hebben we aangetoond dat de geleidbaarheid van de ring quasi-periodieke oscillaties vertoont als functie van de Rashba SBW sterkte α. Aangezien de sterkte van de Rashba SBW getuned kan worden door middel van een gate-spanning, hebben we voorgesteld om een dergelijke ring te gebruiken als een schakelbare geleider, die gebaseerd is op de spin van electronen in plaats van op hun lading.

De bovengenoemde spin-geïnduceerde fase-verschuiving staat bekend als de geometrische Aharonov-Casher fase (het wordt een *geometrische* fase genoemd, omdat de fase alleen afhangt van de hoek die de spin maakt tijdens zijn beweging rond de ring, en niet van de tijd die het electron erover doet). Men heeft voorspeld dat deze Aharonov-Casher fase ook de Aharonov-Bohm magneto-weerstand oscillaties in de ring beïnvloedt. Als we de spin dynamica van de electronen buiten beschouwing laten, correspondeert de oscillatie periode van de weerstand met een flux van h/e door de ring. Er treedt echter een afwijking van de h/e periodiciteit op als we de spin dynamica (Aharonov-Casher phase) mee in beschouwing nemen. Dientengevolge zal de Aharonov-Casher fase naar verwachting zichtbare consequenties hebben in het Fourier spectrum van de Aharonov-Bohm oscillaties. De experimentele detectie van deze verschijnselen in het Fourier spectrum was

één van de doelen van het tweede gedeelte van dit proefschrift.

Wij hebben een ring structuur gefabriceerd uit een 2-dimensionaal electron gas met sterke Rashba SBW. We hebben laten zien dat het gemeten Fourier spectrum van de Aharonov-Bohm oscillaties wordt gedomineerd door sample specifieke eigenschappen, vanwege de eindige breedte van de armen van de ring en het diffunderend electron transport er doorheen. Dit belemmert de directe observatie van spin effecten in het Fourier spectrum. Wij hebben gedemonstreerd dat het middelen van de modulus van het Fourier spectrum $|G(\nu)|$, over metingen die genomen zijn bij verschillende waarden van de gate-spanning, het mogelijk maakt om de sample specifieke eigenschappen te onderdrukken op een gecontroleerde manier. Hierdoor hebben wij kunnen observeren dat de h/e piek in het ensemble-gemiddelde Fourier spectrum $\langle |G(\nu)| \rangle$ een duidelijke dubbele-piek structuur vertoont. Door middel van een statistische analyse hebben we aangetoond dat deze dubbele-piek structuur statistisch significant is. Deze observatie kan dus niet worden toegeschreven aan een resterend sample specifieke effect, maar duidt op een spin-geinduceerd verschijnsel.

In het resterende gedeelte van dit proefschrift hebben we systematisch onderzocht hoe de competitie tussen Rashba SBW en Zeeman koppeling de spin dynamica en fase-coherent electron transport beïnvloedt in 2D electron gassen. Voor deze experimenten hebben we Hall structuren gefabriceerd uit verschillende heterostructuren, welke zodanig ontworpen zijn, dat ze ieder een andere Rashba SBW sterkte hebben. Zeeman koppeling werd bewerkstelligd door een magneetveld aan te leggen parallel aan het 2D electronen gas (hierdoor werd de koppeling tussen het magneetveld en de beweging van de electronen geminimaliseerd). Een gate-electrode maakte het mogelijk om de relevante parameters te controleren, zoals de vrije weglengte van de electronen, de Rashba SBW sterkte, en daarmee ook de spin relaxatie tijd τ_s van de electronen in het electron gas.

Wij hebben een nieuwe methode ontwikkeld, gebruik makende van de kwantitatieve analyse van zwakke (anti-)lokalisatie metingen, die het mogelijk maakt de fase-coherentie tijd en de spin relaxatie tijd te bepalen, als functie van de sterkte van de Rashba SBW en de Zeeman koppeling. Door middel van deze analyse hebben we aangetoond dat de spin relaxatie tijd toeneemt naar mate de Zeeman interactie sterker wordt. Dit toont aan dat de electron spin zich (gedeeltelijk) oplijnt met het aangelegde magneetveld. Met andere woorden, we hebben gedemonstreerd dat een magneetveld een stabliserende werking heeft op de precessie-as van de spin. In het bijzonder hebben we aangetoond dat de spin relaxatie tijd alleen een functie is van E_Z/E_{SOI}, waar E_Z de Zeeman energie is en $E_{SOI} = \hbar/\tau_s$ correspondeert met de Rashba SBW energie.

Daarnaast hebben we aangetoond, door middel van fase-coherente transport

metingen, dat de competitie tussen Rashba SBW en Zeeman interactie resulteert in het breken van de tijd-omkeer symmetrie. Deze competitie is dus analoog aan een magnetische flux door het 2D electron gas; beiden resulteren in een fase verschuiving tussen electron golven die tegengesteld in de tijd bewegen. We hebben echter gedemonstreerd dat het breken van de tijd-omkeer symmetrie verzadigt wanneer $E_Z/E_{SOI} \approx 1$, oftewel wanneer de spins in de richting van het aangelegde magneetveld beginnen te wijzen. Tenslotte hebben we laten zien dat dit tijd-omkeer symmetrie brekend mechanisme een *universele functie* is van de ratio E_Z/E_{SOI}.

Delft, April 2005

List of publications

1. F.E. Meijer, A.F. Morpurgo, T.M. Klapwijk, and J. Nitta
   Universal spin-induced Time Reversal Symmetry breaking in two-dimensional electron gases with Rashba spin-orbit interaction
   Phys. Rev. Lett. **94**, 186805 (2005)

2. F.E. Meijer, A.F. Morpurgo, T.M. Klapwijk, T. Koga, and J. Nitta
   Competition between spin-orbit interaction and Zeeman coupling in Rashba two-dimensional electron gases
   Phys. Rev. B **70**, 201307(R) (2004)

3. F.E. Meijer, A.F. Morpurgo, T.M. Klapwijk, T. Koga, and J. Nitta
   Experiments on Aharonov-Bohm conductance oscillations: a statistical analysis of the ensemble-averaged Fourier spectrum
   Physica E **22**, 402 (2004)

4. F.E. Meijer, A.F. Morpurgo, T.M. Klapwijk, T. Koga, and J. Nitta
   Statistical significance of the fine structure in the frequency spectrum of Aharonov-Bohm conductance oscillations
   Phys. Rev. B **69**, 35308 (2004)

5. J. Nitta, T. Koga, and F.E. Meijer
   Effect of spin-orbit interaction in an InGaAs-based Aharonov-Bohm ring structure
   Physica E **18**, 143 (2003)

6. J. Nitta, T. Koga, and F.E. Meijer
   Spin-orbit interaction and its application for a spin interference device
   "Mesoscopic Superconductivity and Spintronics", Edited by H. Takayanagi and J. Nitta, World Scientific, 55 (2003) (ISBN 981-238-169-4)

7. F.E. Meijer, A.F. Morpurgo, and T.M. Klapwijk
   One-dimensional ring in the presence of Rashba spin-orbit interaction: Derivation of the correct Hamiltonian
   Phys. Rev. B **66**, 33107 (2002)

8. N.N. Iosad, A.B. Ermakov, F.E. Meijer, B.D. Jackson, and T.M. Klapwijk
   Characterization of the fabrication process of Nb/Al-AlNx/Nb tunnel junctions with low R_nA values up to 1 $\Omega\mu m^2$
   Superconductor Science & Technology **15**, 945 (2002)

9. J. Nitta, F.E. Meijer, Y. Narita, and H. Takayanagi
   Gate voltage-dependent Aharanov-Bohm experiment in the presence of Rashba spin-orbit interaction
   Physica E **6**, 318 (2000)

10. J. Nitta, F.E. Meijer, and H. Takayanagi
    Spin-interference device
    Appl. Phys. Lett. **75**, 695 (1999)

Curriculum Vitae

Frank Erik Meijer

02 - 03 - 1976   Born in Groningen, The Netherlands.

1988 - 1994   Grammar school
Dr. Aletta-Jacobscollege, Hoogezand-Sappemeer
(received "Eindexamen-prijs")

1994 - 2000   M.Sc. Applied Physics (*cum laude*),
University of Groningen.
Supervision: Prof. dr. ir. B.J. van Wees
Subject: Transport through superconducting quantum dots
(received "Propedeuse-prijs 1994/1995")

2000 - 2001   Management Trainee at the ABN-AMRO bank
Department of Credit Risk Modelling
Subject: developing model for Risk Adjusted Return on Capital

2001 - 2005   Ph.D. research at Delft University of Technology
and NTT Basic Research Laboratories, Atsugi, Japan
Supervision: Prof. dr. ir. T.M. Klapwijk
Co-supervision: Dr. A.F. Morpurgo
Co-supervision: Prof. dr. J. Nitta (NTT, Japan)
Subject: Rashba spin-orbit interaction in mesoscopic systems